SAND2019-3215R

ENVIRONMENTAL PERSISTANCE OF BIOLOGICAL AEROSOLS IN OUTDOOR AND SIMULATED ENVIRONMENTS

FINAL REPORT

Contract: IA: DOE10072A-10121, BASIC, Control No. 10121
IA: DTRA1002715543, Control No. 15543
IA: DTRA100271929, BASIC, Control No. HDTRA1619299

Prepared for
Department: Chemical/Biological Technologies Department (CB)/ Emerging Threats Division/ Threat Agent Sciences
Directorate: J9 (R&D or Research & Development Directorate)

Prepared by:
Sean Kinahan, Matthew Tezak, Don Collins, Danielle Rivera, Andres Sanchez, Cathryn Siegrist, Steven Storch, Gabriel Lucero, Yongle Pan, Josh Santarpia

Date: November 30, 2018
Revision: 1.0

TABLE OF CONTENTS

LIST OF FIGURES

LIST OF TABLES

NOMENCLATURE

AMS	Aerosol mass spectrometer
APS	Aerodynamic particle sizer
ARL	Army Research Laboratory
B.t.	*Bacillus thuringiensis* al hakam
CAGE	Captive Aerosol Growth and Evolution
CCN	Cloud condensation nuclei
CFU	Colony-forming unit
CSTR	Continuous stirred tank reactor
Da	Dalton
DI	Deionized
DMA	Differential mobility analyzer
DNA	Deoxyribonucleic acid
D_p	Particle diameter
DSTL	Defence Science and Technology Laboratory
E. coli	*Escherichia coli*
ePTFE	Expanded polytetrafluroethylene
FEP	Fluorinated ethylene propylene
FEVE	Fluoroethylene vinyl ether
GSD	Geometric standard deviation
IM	Injected modes
kHz	Kilohertz
HEPA	High-efficiency particulate arresting
Hg	Mercury
HR-TOF-AMS	High resolution time-of-flight aerosol mass spectrometer
JSF	Jones State Forest
LB	Luria Bertani
LIF	Light induced fluorescence
Lpm	Liters per minute
m^3/min	Cubic meters per minute
MFC	Mass flow controller
mL	Milliliter
MMAD	Mass median aerodynamic diameter
MΩ	Megaohm
µL	Microliter
µm	Micrometer OR micron
N	Number concentration
nm	Nanometer
NM	Nucleation modes
NPF	New particle formation
O_3	Ozone
PBS	Phosphate-buffered saline
PCR	Polymerase chain reaction
PFU	Plaque-forming unit
ppb	Parts per billion

ppm	Parts per million
PTFE	Polytetrafluoroethylene OR Teflon™
ROS	Reactive oxygen species
RNS	Reactive nitrogen species
RH	Relative humidity
RNA	Ribonucleic acid
RT-PCR	Reverse transcription polymerase chain reaction
S	Surface area concentration
SAM	Surface area mode
SMPS	Scanning Mobility Particle Sizer
SOA	Secondary-organic aerosol
SPFS	Single Particle Fluorescent Spectrometer
UH	University of Houston
UV	Ultraviolet
UV-APS	Ultraviolet Aerodynamic Particle Sizer
VOC(s)	Volatile organic compound(s)
WIBS	Wideband Integrated Bioaerosol Spectrometer

1. INTRODUCTION AND BACKGROUND

The fate of biological aerosols in the atmosphere depends on the unique and dynamic environmental conditions it is exposed to during transport. There exist many processes that can impact the effectiveness of an aerosol release, and its fate in the environment. Aerosol properties may be modified if biological particles that are released into the atmosphere interact with free radicals, volatile organic compounds (VOC), semi-volatile organic compounds, and inorganic gas-phase compounds, such as NOx and SOx. Meteorological conditions such as ultraviolet (UV)-light, relative humidity (RH), and temperature have also been shown to affect biological aerosols, with interactions dependent on both the organism and aerosol's chemical make-up. Oxidation or secondary-organic aerosol (SOA) formations on the particle can also lead to changes in surface proteins and extra-cellular nucleic acids that may agent detection technologies, at a different rate than the infectivity of the agents. Once modified, agents may then be transported via many atmospheric processes (depicted in Figure 1) such as deposition or incorporation into cloud condensation nuclei (CCN). Although these processes are known, it is unclear what the resulting form and potency of the bioaerosol may be after alteration by these processes.

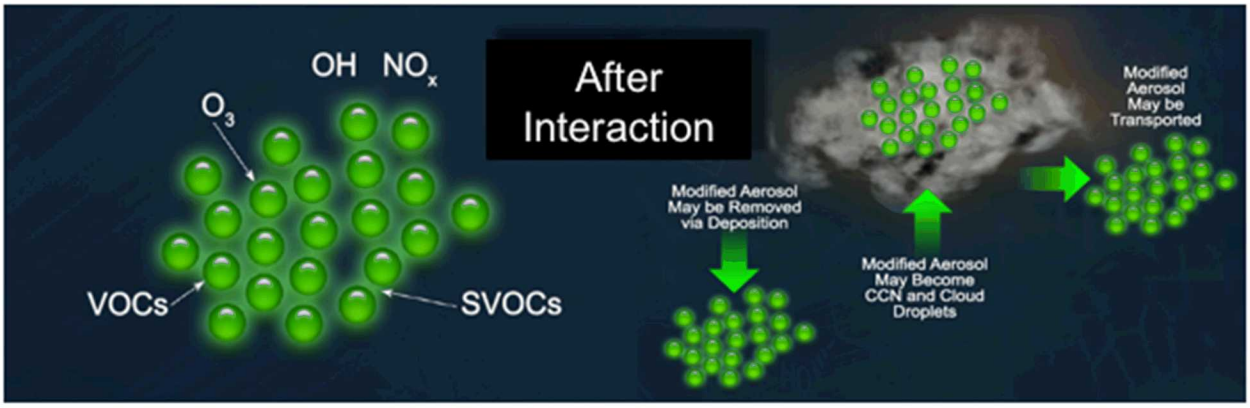

Figure 1: Demonstration of Various Agent Fate Pathways

2. OBJECTIVES

The objective of this research effort was to develop laboratory techniques for understanding the chemistry that affects viruses, bacteria, and protein aerosols in the outdoor environment. This effort combines laboratory and field measurements to measure both the detailed chemistry that affects these bioaerosols and frame it with ambient measurements. Ultimately, the data sets from this type of research can be incorporated into a model to more accurately depict the fate of biological aerosols.

3. AGING METHODOLOGY

3.1 Laboratory Aging Methods

The team utilized large rotating drums, to examine the effect of natural environmental and controlled laboratory aging on biological aerosols. The laboratory drum is an upgraded version of an existing SNL drum, capable of controlling and simulating, Ozone, RH, UV-light, and a volatile organic individually or together, to examine combinations of variables (Figure 2). Past

attempts at fabricating the entire drum from inert material (Santarpia et al., 2012) have been problematic due to the inadvertent generation of static charge during the rotation of the drum. Pan et al. (2013) used a Teflon (PTFE)-coated stainless-steel drum in order to mitigate this affect, which is the approach that was taken in this study. This process is relatively common in chemical pipes. Further, other drum materials that are involved in rotation were selected to ensure that no plastic on plastic contact is made during rotation, in order to limit the generation of charge. The Teflon coating will ensure that the reaction vessel is truly inert to both ozone and the volatile organic compounds. A chamber volume of 400 L, corresponding to a radius of 15 inches and a length of 36 inches, was used to ensure that there is ample volume for intermittent sampling throughout the aging experiments, which in these experiments lasted several hours.

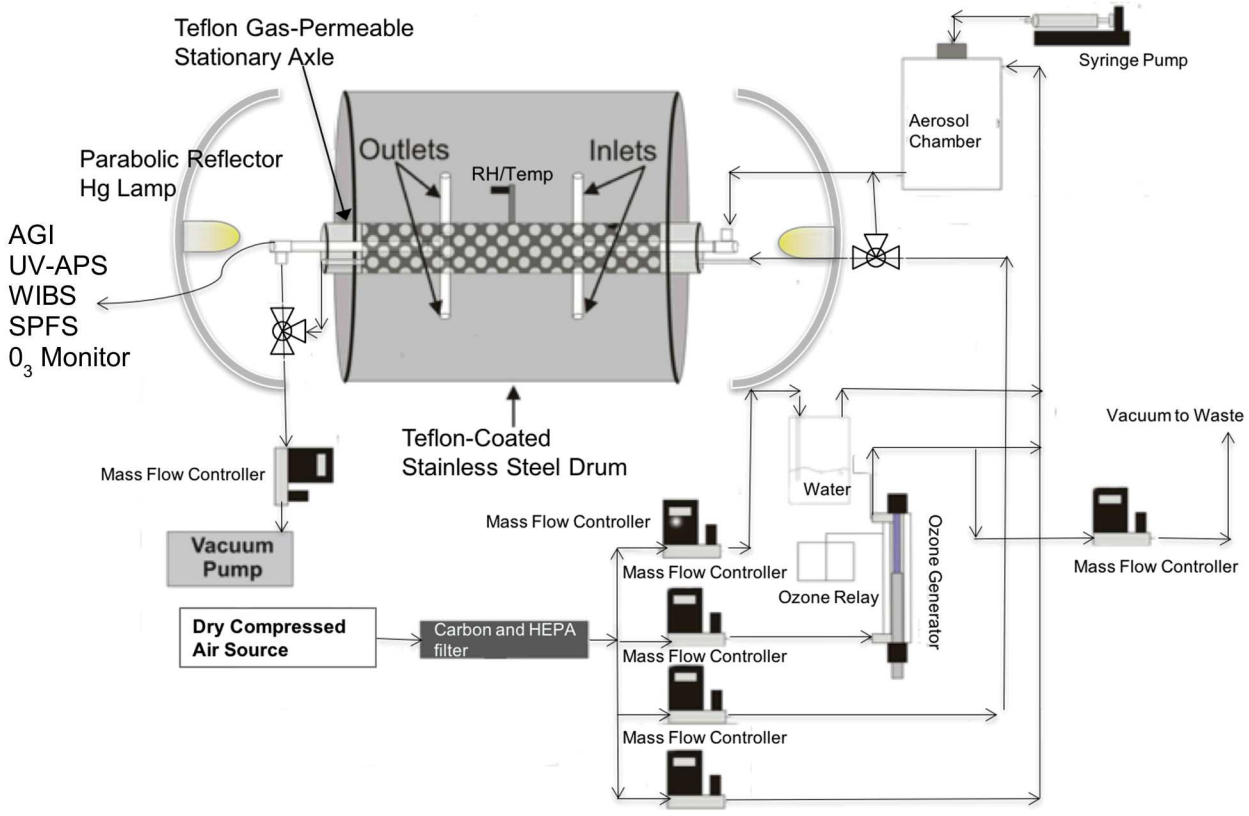

Figure 2. Laboratory Rotating Drum Diagram

Briefly, the rotating drum is supplied with a dry laboratory compressed air source, shown in the bottom left of figure 2. That air is carbon and high-efficiency particulate arresting (HEPA) filtered to remove residual volatile compounds and particulates. The air is then split to supply humid air (through a deionized (DI) water bubbler), ozone-laden air, dry air, and air for particulate generation. Each is metered at a target flow rate via Alicat Scientific mass flow controllers (MFC), controlled through a custom LabVIEW interface.

3.1.1 Relative Humidity

Humid air is generated by bubbling clean air through 18 MΩ DI water, and combining the resulting air stream with dry air, to achieve a particular RH. RH feedback is achieved utilizing a HOBO Inc. wireless temperature and humidity transmitter (Model: ZW-003). Utilizing a

sampling rate of once per minute. Due to the low sampling frequency, RH is mass flow controller balanced to maintain a target of either 80% or <30%. An access panel is present on the drum exterior, to allow for cleaning, replacement of batteries, and adjustments of tubing (Figure 4)

3.1.2 Ozone

When necessary to achieve target test conditions, ozone (O_3) is generated using a software-operated, relay-controlled, UV penlight (Pen Ray, 97-0067-01), enclosed within a custom polytetrafluoroethylene (PTFE) housing. As throughout the system, The mercury lamp produces UV light with energy sufficient to photolyze oxygen (wavelengths less than 220 nm). The singlet oxygen formed recombines with molecular oxygen (O_2) to form ozone. Since the concentration of ozone is dependent on the flow rate and contact time of the air stream over the UV-light, an additional MFC, on the vacuum waste line, is utilized to vary the amount of ozone entering the drum, so the generation line can remain constant. Generated at 4.8 ppm, into 5 lpm of carrier air, the ozone is mixed in 1-2 lpm quantities to achieve a target concentration of 100 ppb in the drum, based on periodic sampling feedback, with the rest of the carrier air diverted to waste. Ozone concentration was determined using an Eco Sensors UV-100 Ozone Analyzer, with a range of 0-1000 ppb in 10 ppb increments, sampling at 1 lpm. A selection of samples chosen randomly from all three years of testing demonstrates the variability inherent in sampling at 30-minute periods (Figure 3).

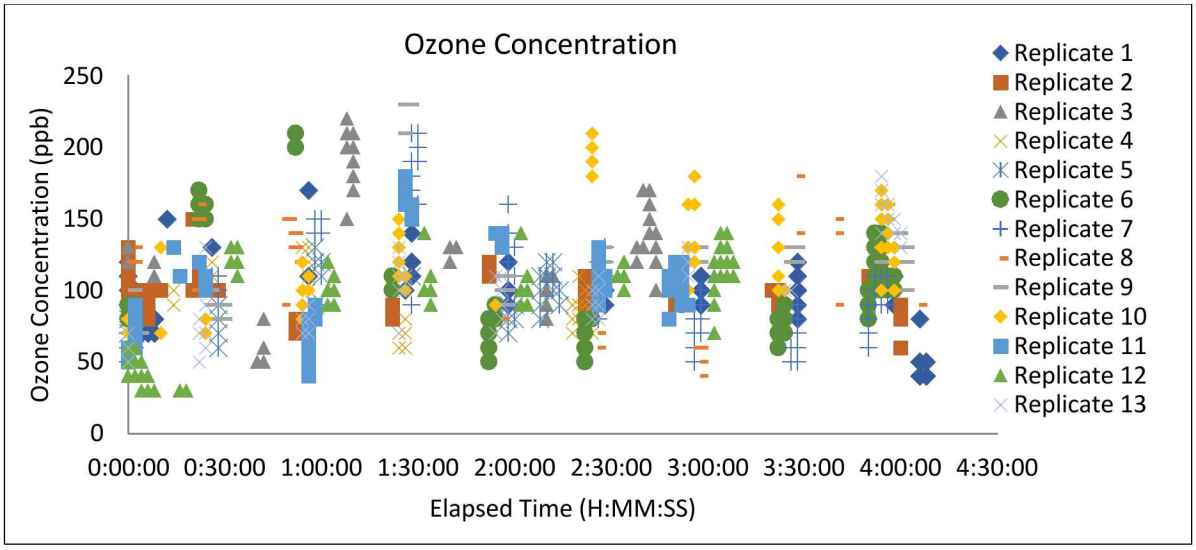

Figure 3. Ozone Concentration vs Time. At least four ten second samples are taken at each 30-minute time period.

3.1.3 Gas-Phase Compound Introduction to Drum

Ozone and RH conditioned air can be introduced into the chamber in either of two methods. First, by introducing through the direct injection ports, which allows for better mixing and directly replaces air in the drum with conditioned air. This method is used to precondition the drum to target concentrations and humidities quickly. Second, the conditioned air can travel along a 2-inch diameter perforated tube in the center of the rotating drum (Figure 4). The

perforated tube is lined with an expanded PTFE-membrane (ePTFE), which acts as a gas permeable conditioning system. This membrane is further described in the outdoor methods section. This approach is utilized during testing, to allow mixing of gaseous species through diffusion, while keeping forces that may disrupt rotational flow to a minimum. Direct sampling lines utilize conical reducers, to limit the disrupting injecting or sampling air velocity by increasing the cross-sectional area (Figure 4).

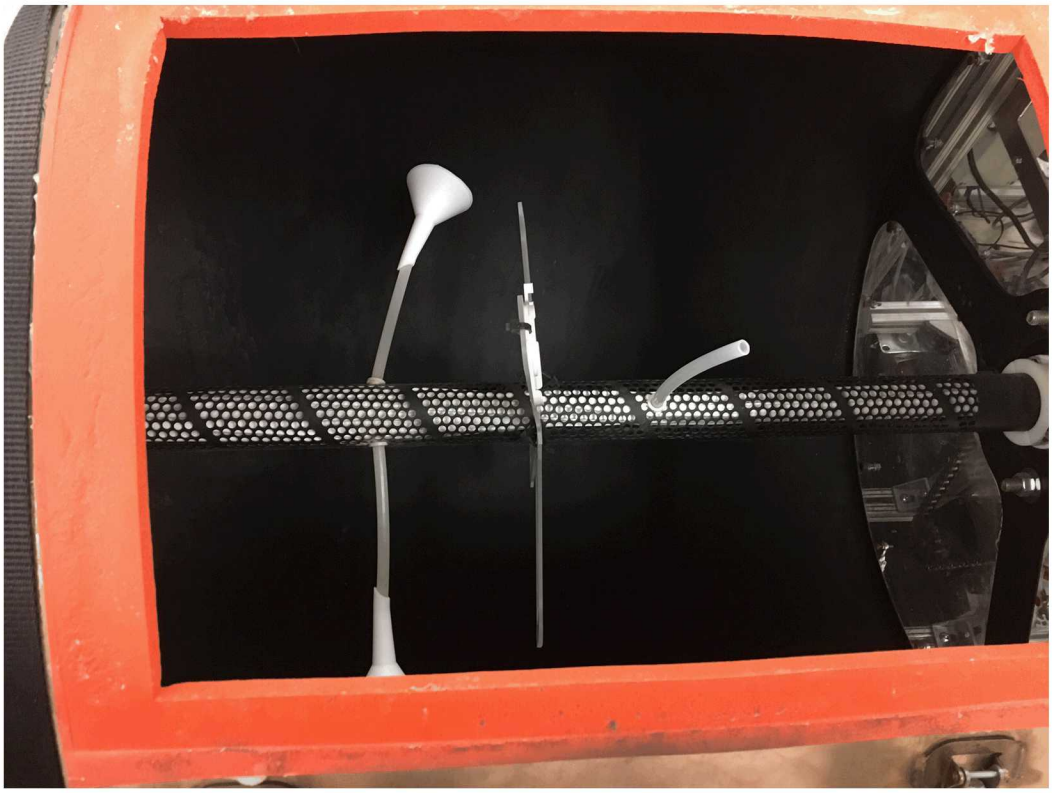

Figure 4. Inside View of Laboratory Rotating Drum. Drum contains a perforated ePTFE-lined center axle and conical reducers on sampling lines. Center of photo: mounting bracket for RH/Temperature probe.

3.1.4 Aerosol Generator

Aerosols are generated using a Sono-Tek Inc. 120 kHz ultrasonic nozzle, into the top of a stainless cylindrical aerosol chamber (Figure 2), with a 30-mL syringe and pump (Cole-palmer) to infuse the liquid aerosol suspension. A broadband ultrasonic generator (Sono-Tek Inc) generates the sine wave and controls the power level, set at 3 W. The tip of the Sono-Tek is placed at the top of an aerosol chamber, and sealed with custom fine-tapered, PTFE wrapped threads. Clean carrier air enters the aerosol chamber through a conical expansion near the top, at a flow rate of 10 lpm, to reduce the velocity and minimize the amount of shearing at the point of aerosol generation. The chamber is 24 inches in height, to allow the aerosols to begin to dry and enter the rotating drum, through a second conical reduction at the bottom of the aerosol chamber. The liquid medium and concentration used for aerosolization is organism dependent, and described below for each agent tested in the drum.

3.1.5 UV Light

UV light is produced using two Virtual Sun 1000 W mercury halide lamps with parabolic reflectors, to further direct light into the rotating drum. Each end of the drum utilizes 0.125 inch thick Acrylite OP-4 acrylic, which maintains above 70% transmission of UV light at 280 nm, and approximately 90% at 350 nm (Figure 5).

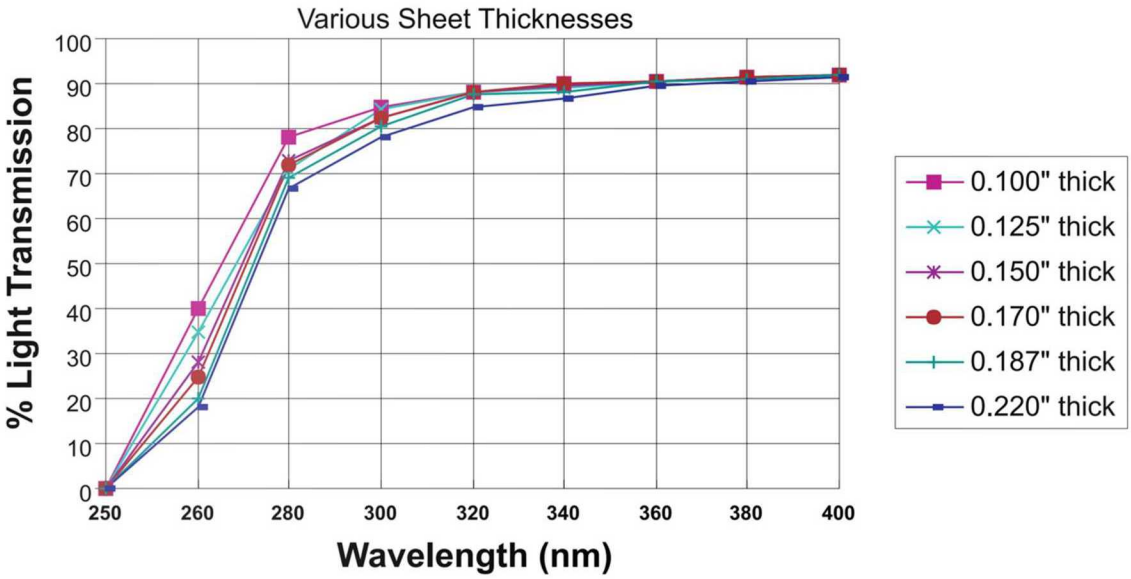

Figure 5. Transmissivity of OP-4 Acrylic – Vendor Supplied

If test conditions necessitate UV-light, portable evaporative coolers are used on the UV-light sources to limit the amount of temperature variation in the system. Temperatures varied from 23°C to 28°C, based primarily on the usage of UV-lights.

3.1.6 Interdependence of Variables

Higher temperatures, and variations between tests caused some variations in relative humidity. The usage of clean dry air for aerosolization, and the evaporation of nebulized droplets into dry particulate, caused initial test conditions to be more humid during dry tests, when injection air was lower in humidity than the 80% target; and less humid during wet tests, when injection air was higher in humidity than the target. These variations and average humidities can be seen across six dry and wet RH conditions in Figures 6 and 7.

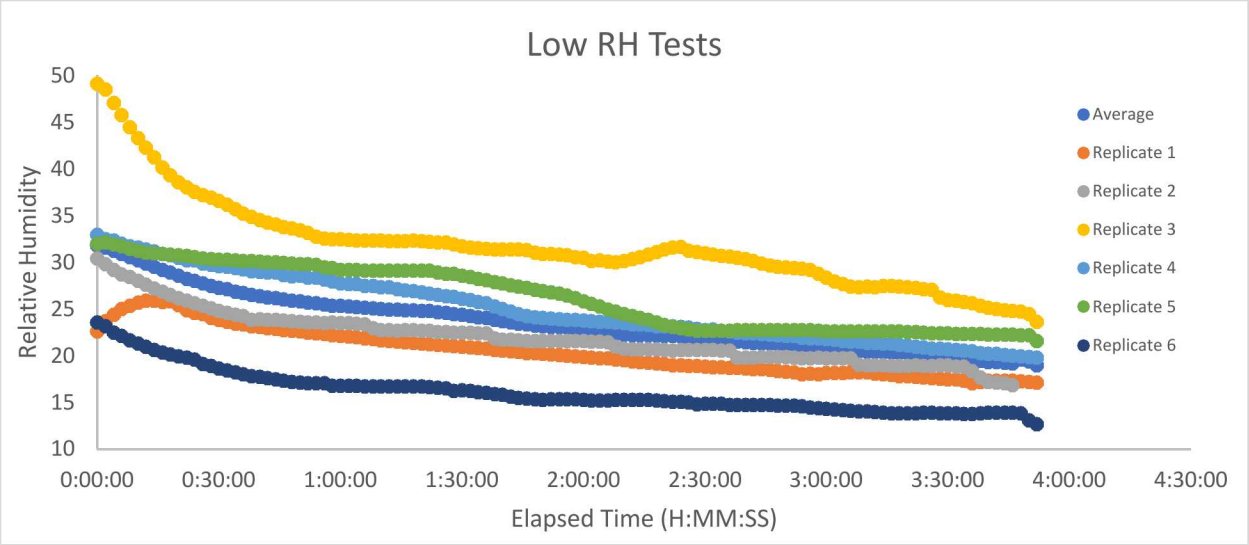

Figure 6. Low RH Test Conditions

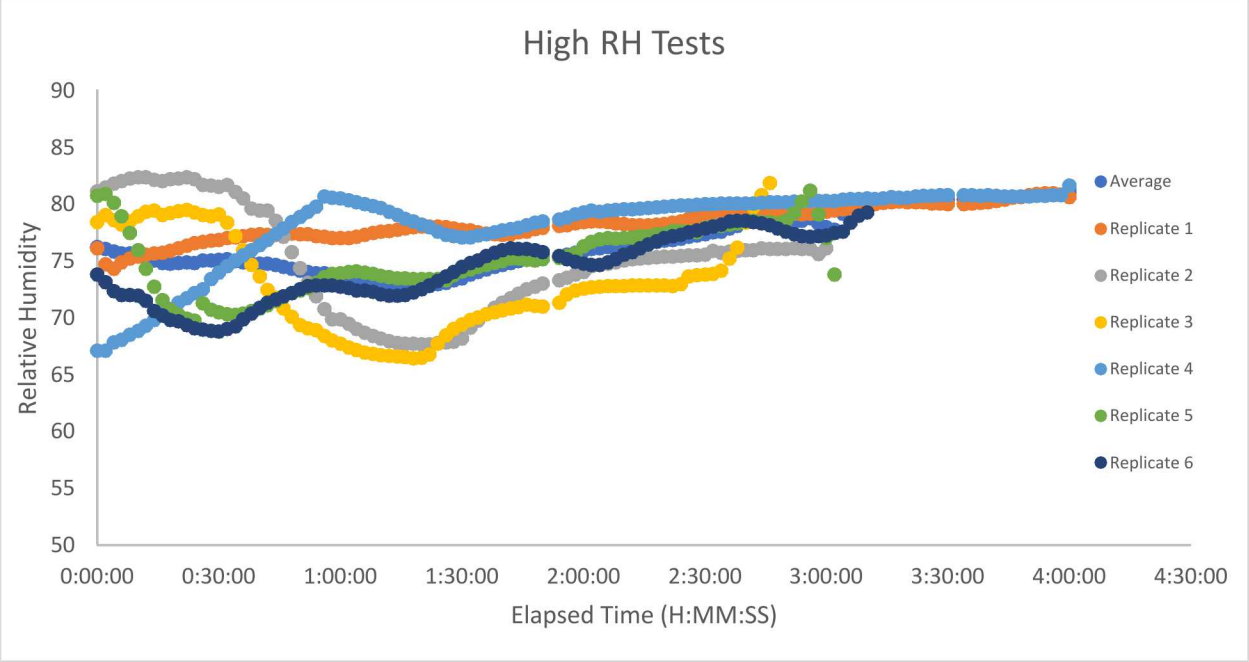

Figure 7. High RH Test Conditions

3.1.7 Addition of Volatile Organic Compounds

The addition of VOCs to the laboratory rotating drum was completed during the second year of the project, with a permeation tube and permeation tube holder used to vaporize target chemicals. Toluene and α-pinene were chosen as representative pollutant compounds generated from anthropogenic and naturally-occurring biogenic emissions processes.

A VICI Dynacal permeation tube holder, a U-shaped glass vial with Teflon-lined screw caps, and containing glass beads on one side, is used to hold the diffusion vials. Mass-flow controlled air is allowed to enter a ¼" fitting at 1 lpm, and equilibrate to the temperature of the glass holder, which is submerged in a 74ºC silicone oil bath. Silicone oil is used to prevent evaporation losses associated with water. The glass beads breakup the airflow, and contribute to the heat transfer of the air (Figure 8). The other half of the tube holder contains a VICI Dynacal diffusion vial, Vial C, which has a 2.0 mm, 2.0 inch long capillary tube at the end of a reservoir containing 2.5 mL of liquid to be vaporized.

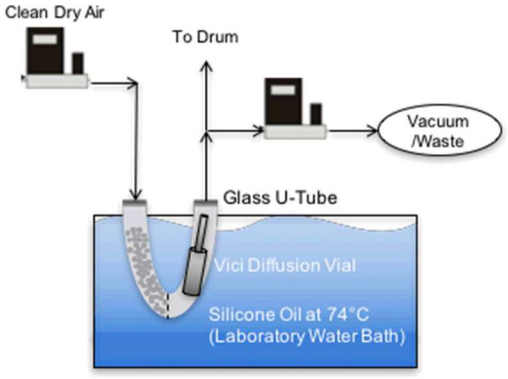

Figure 8. VOC Mass-Balanced Vaporization Setup. Diffusion vials produce linear vaporization at a given temperature.

Permeation of vaporized material will occur at a linear rate governed by the capillary diameter and length, as well as the temperature, molecular weight, pressure, and diffusion coefficient of the material:

Equation 1. Vaporization Rate

$$r = 1.90 * 10^4 T D_0 M \frac{A}{L} \log\left(\frac{P}{P-\rho}\right)$$

where:

r = rate of diffusion (ng/min)
T = temperature of vapor (ºK)
D_0 = Diffusion coefficient
M = molecular weight (g/mol)
A = cross-sectional area of capillary (cm^2)
L = length of diffusion path (cm)
P = atmospheric pressure (mm Hg)
ρ = vapor pressure of chemical at T (ºK)

For toluene, Equation 1 predicts a vaporization rate of 68132 ng/minute, or 4.08 mg/hour, using a temperature of 347.38K, vapor pressure of 236.9 mm Hg (Goodwin, 1989), D_0 of 0.0849 cm^2/sec (VICI), path length of 5.08 cm, cross-sectional area of 0.0314 cm^2, and atmospheric pressure of 610 mm Hg (approximate for 6000 feet of altitude).

Ultimately, the measured vaporization rate was followed up with a gravimetric measurement of the mass change over 48+ hours. The change in mass over time, which can be determined with the slope of a linear fit, is estimated while forcing an intercept of zero, corresponding to no mass vaporized at the beginning of vaporization (Figure 9).

Without a real-time gas-phase mass-spectrometry capability on-site, the concentration in the drum was determined by balance of mass with two mass flow controllers, and a known vaporization rate. The first flow controller provided a consistent carrier air flowrate, and the second was plumbed to waste, under vacuum. By adjusting this waste controller, it was possible to vary the fraction of VOC-containing air entering the drum. With the VOC concentration in the supply line constant, the LabVIEW control system was setup so that the waste line was varied depending on the amount of ozone, wet, and dry air currently being utilized. A temperature of 74ºC ensured that both compounds would vaporize at high rates, minimizing any dilution effect on the humid air or ozone concentrations, and lowering the velocity of air entering the drum, to prevent unnecessary particle losses.

The Toluene vaporization rate (Figure 9) averages out to 4.014 mg/hour, and can be converted to ppm or ppb through the ideal gas law (Equation 2), and a known mass flow rate of 1 lpm (0.06 m^3/hour):

Equation 2. Conversion to PPM

$$Concentration\ (ppm) = \frac{VR\ \left(\frac{mg}{hour}\right) * T * R}{0.06\ \left(\frac{m^3}{hour}\right) * MW\ \left(\frac{grams}{mole}\right) * P}$$

Where:

VR = Vaporization Rate (mg/hour)
T = Temperature (Kelvin)
R = Gas Constant (62.4 L torr/mol K)
MW = Molecular Weight (grams/mole)
P = Pressure (torr)

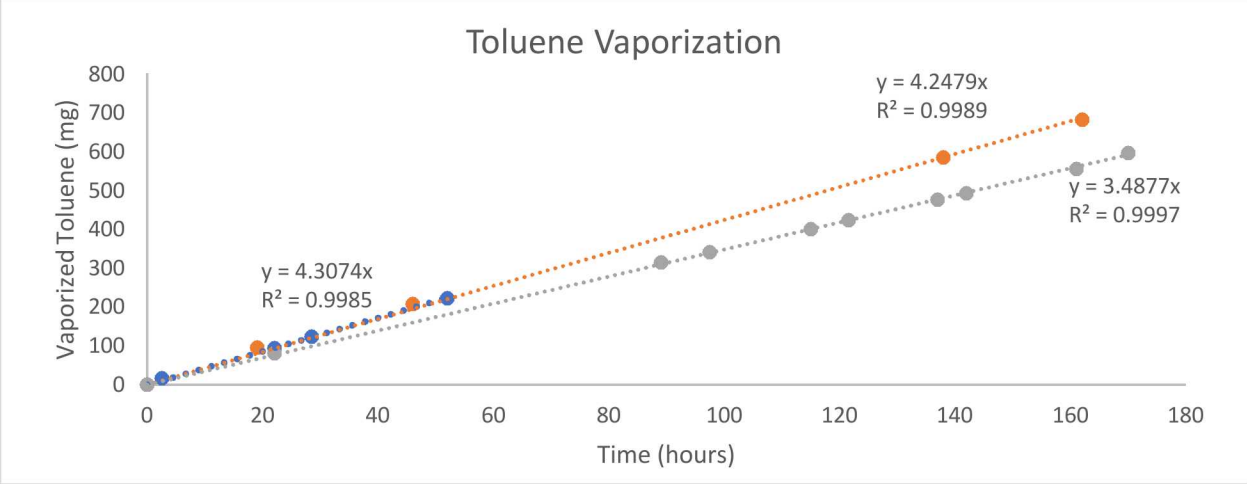

Figure 9. Toluene Vaporization Rate

The vaporization rate of 4.014 mg/hour leads to a concentration of 17.534 ppm, or 17,534 ppb. , of which only a fraction enters the drum to achieve the target concentration. Similarly, the alpha pinene vaporization rate of 0.375 mg/hour (Figure 10) corresponds to a concentration of 1.108 ppm or 1108 ppb. In both cases, the LabVIEW interface sends an appropriate fraction of the pollutant-laden air to waste to achieve the target concentration.

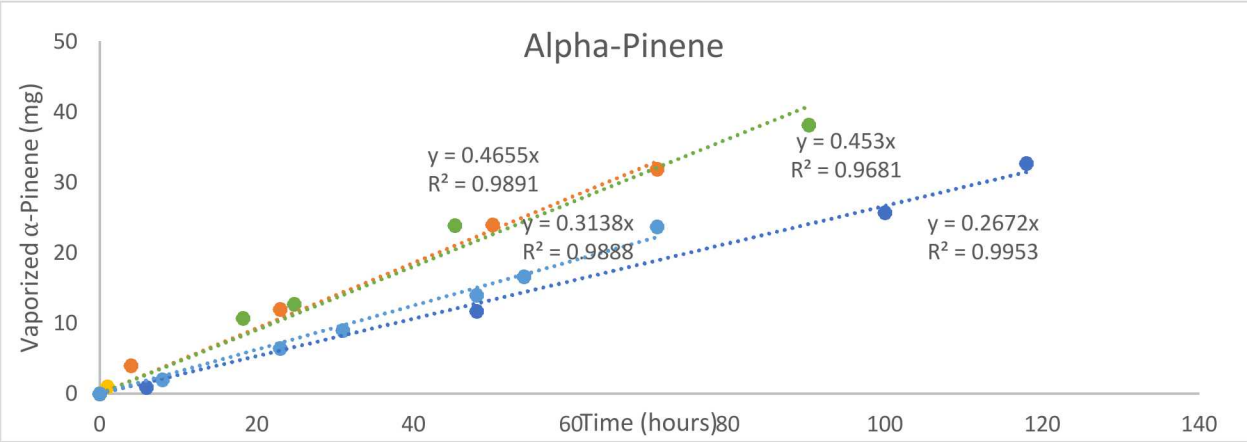

Figure 10. Alpha-Pinene Vaporization Rate

3.2 Field Aging Methods

3.2.1 Field site description

The site of both field studies supported through this project was the WG Jones State Forest (JSF), which is a roughly 2,000 acre, pine-dominated forest located between Conroe and The Woodlands in southeast Texas. The clearing in which the chambers were located, their location within the roughly rectangular state forest, and their proximity to the Houston metropolitan area are shown in the set of satellite images in Figure 11.

Figure 11. Satellite images of the WG Jones State Forest (JSF) site at which the two field studies were conducted. The location of JSF relative to Houston is shown on the left, the location of the field site within the roughly rectangular JSF in the middle, and the clearing at which the chambers and instrument trailers were located on the right.

As shown in Figure 12, the wind roses for the nearby Conroe, TX airport had prevailing winds in the summer months, during which both studies were conducted, from the south with somewhat more directional variability towards the end of the summer in August and September. Those prevailing southerlies bring the complex and concentrated mixture of pollutants from Houston into the test area. The Houston emissions are then mixed with high emissions rates of highly reactive biogenic hydrocarbons such as isoprene and the monoterpenes from the forest and local area.

For the field studies, the goal was to study how fast the viability, fluorescence and PCR signature of a set of bioaerosols were altered due to the chemistry involving those trace gases and due to exposure to solar radiation. The Captive Aerosol Growth and Evolution (CAGE) chambers used in this study, were completely redesigned and fabricated prior to outdoor testing in Houston. Though a description of a predecessor chamber with similar function has been published (Peng et al., 2016; Peng et al., 2017), the current CAGE chambers differ considerably from the earlier generations and are therefore described in detail in this report.

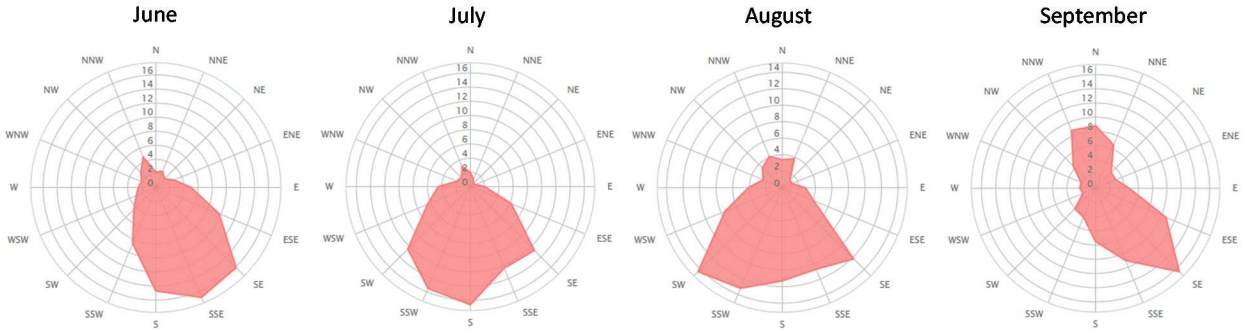

Figure 12. Wind roses for 2000 - 2017 at the nearby Conroe airport. For the four months spanning the periods of the 2015 and 2016 studies the prevailing wind direction is from the south.

3.2.2 CAGE Design and Function

A sketch and a photo of one of the two CAGE chambers used for this project are shown in Figure 12. Each chamber is a 1-m^3 all-Teflon cylindrical enclosure constructed primarily of UV-transmitting fluorinated ethylene propylene (FEP) film (a. in Figure 13). The only non-FEP section of the wall in each chamber is the gas-permeable ePTFE membrane sheet (b.) located at the back end of the cylinder as shown in both the sketch and photo. The stainless steel internal support structures of the chambers are fully wrapped with high density PTFE thread tape, which was first baked overnight at 150°C to vaporize and remove any volatiles left over from its manufacture. Each chamber is suspended in a stainless steel rectangular enclosure that was powder coated with a reflective fluoroethylene vinyl ether (FEVE) fluoropolymer paint. UV-transmitting Plexiglas G-UVT acrylic sides (c.) secured to the frames surround the chambers to block wind that would otherwise increase mixing and, consequently, particle loss rate. These acrylic sides are similar to, albeit a different brand, those used on the laboratory drum. FEP sheets, which has reduced reaction, vaporization, and absorption rates compared to acrylic, cover all interior surfaces of the enclosure within ~0.5 m of the far (right) end, where gas exchange is occurring.

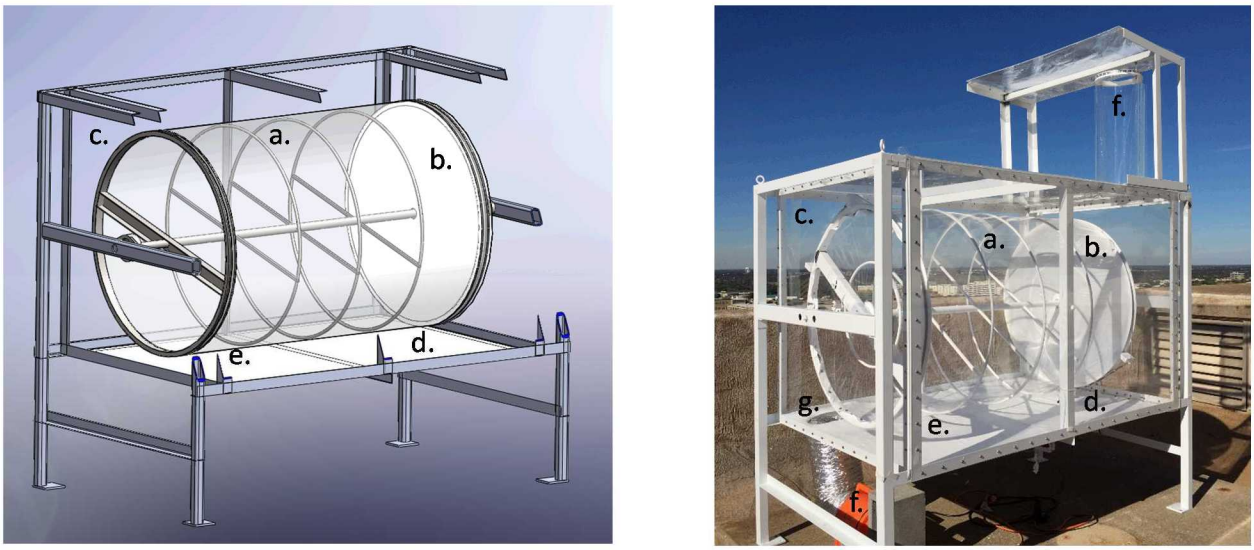

Figure 13. Sketch and photo of a CAGE chamber.

3.2.2.1 Light Transmittance Through CAGE

The overall light transmittance through the chamber and acrylic sheets is evident in the close-up photo in Figure 14. The small loss of UV (and visible) solar radiation through the acrylic and FEP is offset by reflection off a highly UV-reflective PTFE gasket sheet just below the chamber (Figure 13, d.). At the field study site, both chambers were oriented on the south side of the instrument trailer with their ePTFE membranes facing north, to minimize shading throughout the day. Their approximate placement and the valve and tubing configuration used to alternate between the two chambers (referred to simply as chambers A and B) for aerosol injection and sampling is depicted in Figure 14. For most daytime experiments Chamber B was used as a reference and was covered with a light shield that reduced UV intensity to below 1% of that in the unshielded chamber.

Figure 14. Close-up photo of a CAGE chamber highlighting the overall clarity.

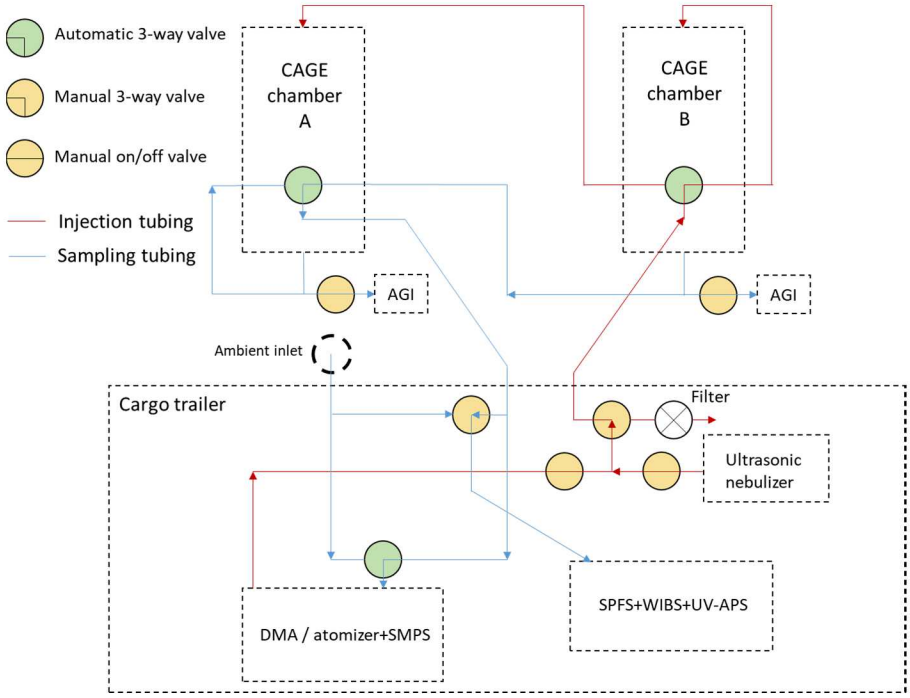

Figure 15. Placement and orientation of the CAGE chambers relative to the instrument trailer and tubing and valve configuration used to inject particles into and sample particles from both CAGE chambers.

Prior to the start of the 2016 field study cosine-weighted solar spectral intensity was measured outside and at a point between the bottom of the chamber and the reflective PTFE gasket (approximately point e. in Figure 13), using a spectroradiometer (StellerNet Inc BLUE-Wave). The results shown in Figure 16 represent the sum of the upwelling and downwelling measurements (spectroradiometer receptor pointing up and down, respectively). The broad spectral transmittance of the chamber and enclosure sides along with the broad spectral reflectance of the PTFE gasket resulted in a close chamber to outside match over the full UV range. Because the spectroradiometer receptor could not be positioned inside the FEP film of the drum, the offset between the two curves is only an approximate indicator of the absolute agreement between the intensities inside and outside of the chamber.

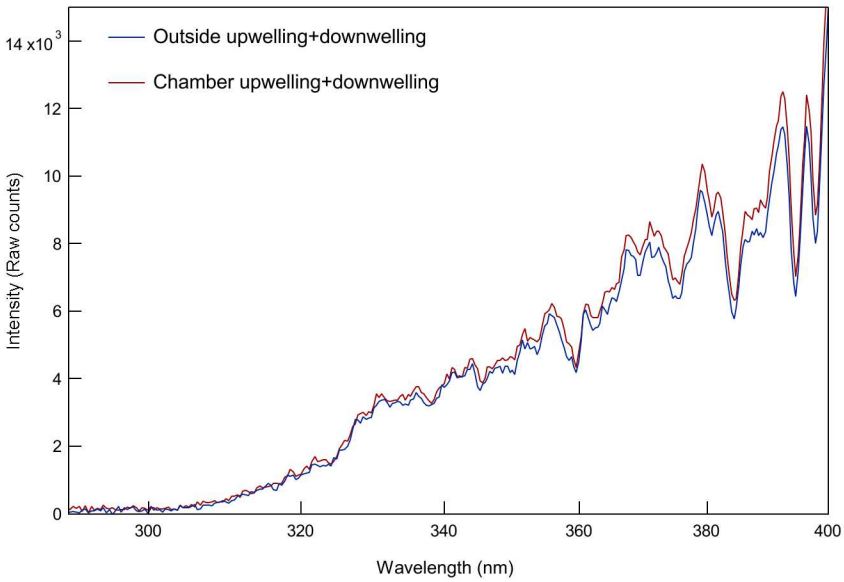

Figure 16. Comparison of spectral intensity measured just below the chamber (around point e. in Figure 12) and just outside of the chamber enclosure on a sunny day. The comparison is meant to highlight the similarity over a broad spectral range and not the absolute difference between the two.

Each FEP drum chamber rotates on a horizontal axis at about 1 rpm to minimize losses of large particles due to settling, and losses of particles of all sizes by dampening convective eddies.

3.2.3 Ambient Air Exchange Design

To encourage air exchange and equilibration, several m^3 min^{-1} of ambient air is drawn through an FEP-lined inlet on top of the chamber (f. in the photo in Figure 13) that is protected by an FEP-wrapped rain hat. The ambient air circulates around the gas-permeable ePTFE membrane and then around the chamber to the opposite end of the enclosure where it is exhausted through a port (g.) connected to a blower located below the acrylic frame. The FEP sheets covering the internal surfaces on the inlet end of the enclosure minimize contact of the air with any non-Teflon surface prior to reaching the ePTFE membrane. Efficient gas exchange across the ePTFE maintains near-ambient trace gas concentrations in the chamber without diluting the captive aerosol as would occur if ambient air were instead pumped into the chamber. Detailed results on gas exchange for various species are reported below.

3.2.4 Comparison to Ambient Sow Chamber

Ambient Sow chambers (so named for their appearance), Figure 16, were designed based on discussion with the Defence Science and Technology Laboratory (DSTL), to be comparable to the Sow chambers used to perform laboratory spider web-captured aerosol studies. This included side loaded web holders and a well-mixed aerosol across the face of the webs. For the outdoor study, several modifications were necessary to the existing laboratory DSTL Sow chambers, in order to have a comparable system to the CAGE chambers. Similar to the CAGE chambers, the interior and interior frame of the ambient Sow chambers were Teflon-coated in white to create an inert chamber that does not absorb additional heat or vapors from the environment. Additionally, UV

Transparent windows made of Acrylite OP4 were inserted to allow ambient solar radiation into the chamber. The UV-transparent FEP film was placed on the side facing the webs, to increase inertness when compared to the OP4 and to match the UV transmissivity of the CAGE chambers (Figure 17). A Teflon gasket sealed the frame of the chamber against the FEP film and window, with a thin piece of Kapton tape holding the folded-over FEP film in place on the outside, and taut against the inside of the window. As an end result, the same thickness and number of layers of FEP and acrylic were matched to the CAGE chambers, with reflective white underneath the chamber to reflect light back towards the spider webs. Both Sows could be externally covered in reflective-white to protect from UV light. For gas exchange, with ambient experiments, one chamber was run under a few inches of vacuum to slowly pass ambient Teflon-filtered, HEPA-rated air over the webs throughout aging. Compared to this ambient air, the other Sow was typically kept under positive pressure with carbon and HEPA filtered air supplied at a low flow rate to keep the webs exposed to fresh, laboratory-grade air. Both could be easily covered or reconfigured to match the testing conditions of the CAGE chambers on a typical day.

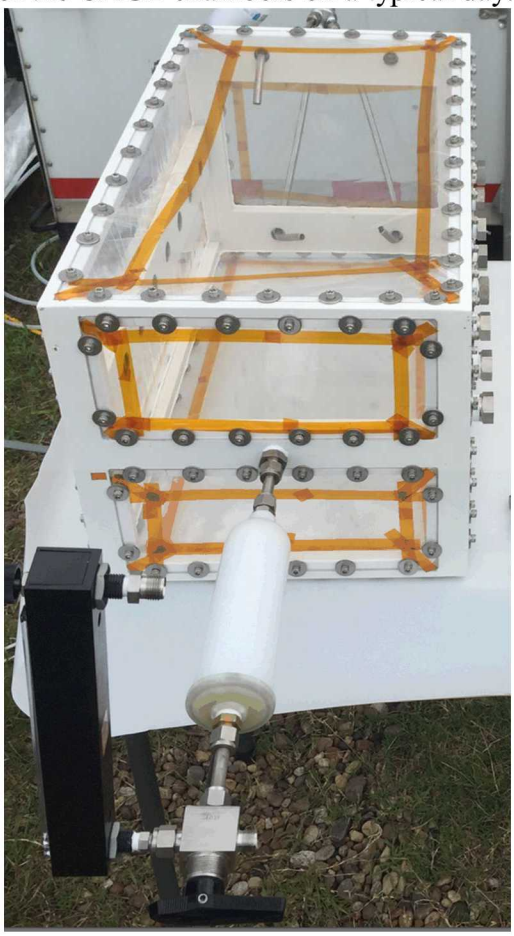

Figure 17. Ambient Sow for Synthetic Spider Web Aging

3.2.5 Relationship between ambient and chamber gas phase composition

The outdoor studies benefited from the fortuitous decision by researchers from University of Houston, Baylor University, and Rice University to deploy their mobile air quality lab to JSF during both the 2015 and 2016 studies. The measurements of gas and aerosol composition were

critically important for analysis and interpretation of the CAGE experiment results. They also provided an opportunity to thoroughly characterize the relationship between chamber and ambient air by temporarily reconfiguring the mobile lab inlet to alternate between sampling from the chambers and from outside. An ~2 hr comparison experiment was conducted at the end of the 2015 study. A much longer, and more revealing, experiment was then conducted over a 3-day break in bioaerosol experiments during the 2016 study. The characterization, results, and comparison informs the performance of the CAGE design and the interpretation of the bacterial aging experiments.

3.2.5.1 CSTR Model and Exchange Rate

During the comparison, automated valves were controlled to produce the repeated sampling pattern:

Ambient (15 min) → Chamber A (15 min) → Ambient (15 min) → Chamber B (15 min) →Repeat

Ozone (O_3), nitric oxide (NO), nitrogen dioxide (NO_2), and the sum of nitrogen oxides (NO_y) were measured with a Thermo Environmental 49C and a pair of Thermo Environmental 42C analyzers. The carbon monoxide (CO) and sulfur dioxide (SO_2) instruments used throughout the rest of the study were turned off to limit the total CAGE chamber extraction flow rate. An Ionicon Q300 quadrupole proton transfer reaction-mass spectrometer (PTR-MS) measured concentrations of a fixed set of VOCs. Of the 19 VOCs measured, analysis focused on the subset of species that were at least sometimes present at concentrations above their detection limit and were not significantly impacted by interference from other species detected at the same masses. The species analyzed were acetaldehyde (detected mass = 45 Da), acetone (59 Da), isoprene (69 Da), methyl vinyl ketone+methacrolein (MVK+MACR; 71 Da), methyl ethyl ketone (MEK; 73 Da), benzene (79 Da), toluene (93 Da), and the monoterpenes (137 Da). Based on regional emissions estimates with the Model of Emissions of Gases and Aerosols from Nature (MEGAN; Guenther et al., 2012) a 2:1 α-pinene:β-pinene split was assumed for the monoterpenes.

Consistent with results from prior chamber-ambient comparisons, trace gas concentrations in the chamber can be explained by treating the volume as a continuous stirred-tank reactor (CSTR). The resulting rate of change of the concentration of any of the trace gases can then be expressed as:

$$\frac{dC_{ch}}{dt} = P - L + \frac{Q_{ex}}{V_{ch}} C_{amb} - \frac{Q_{ex}}{V_{ch}} C_{ch}$$

Equation 3. Continuous Stirred-Tank Reactor Model

Where C_{ch} is the concentration in the chamber, C_{amb} is the ambient concentration, V_{ch} is the volume of the chamber (≈1000 L), P and L are the per unit volume rates of chemical production and loss in the chamber, respectively, and Q_{ex} is the effective exchange "flow rate" across the ePTFE membrane. The value of Q_{ex} is best determined for a gas that has negligible chemical production or loss (P = L = 0) and that is present at concentrations well above the instrument detection limit. NO_y best satisfied those requirements among the species measured during the comparison. The value of Q_{ex} was estimated as that for which the correlation (r^2) between the concentrations measured in the chambers and that based on the ambient concentration time series was greatest. As shown in Figure 18, a Q_{ex} of 33 L/min resulted in a peak r^2 of about 0.97 for both chambers.

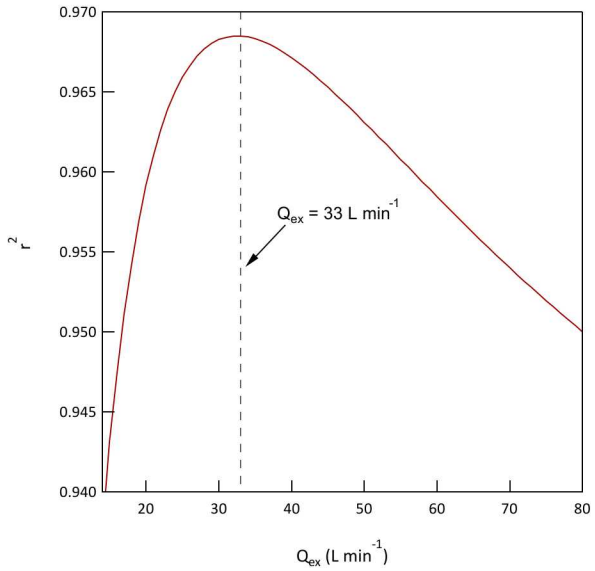

Figure 18. Relationship between the correlation between the time series of NO_y concentration i) measured in the chambers and ii) determined from the ambient measurements assuming the chambers can be modeled as CSTRs with exchange flow rate Q_{ex}. The Q_{ex} used for all subsequent calculations is that at which r^2 was highest. The average of the results for Chambers A and B is shown.

The resulting ~3 day time series for NO_y in Figure 19 shows that the time series of the mixing ratios (~concentration) in the chambers closely match that calculated from the ambient measurements. The most obvious impact of treating the chamber as a CSTR is the smoothing of the short duration peaks and troughs in the ambient data. Figure 20 presents the same data for NO_y (and other species as discussed below) as pairs of mixing ratios i) measured in the chambers (y-axis) and ii) calculated from the ambient measurements (x-axis). The best-fit lines through the NO_y pairs have slopes of 0.98 and 1.00 for Chambers A and B, respectively. A mixing ratio of 1.00 indicates the concentration inside and outside the drums are equal.

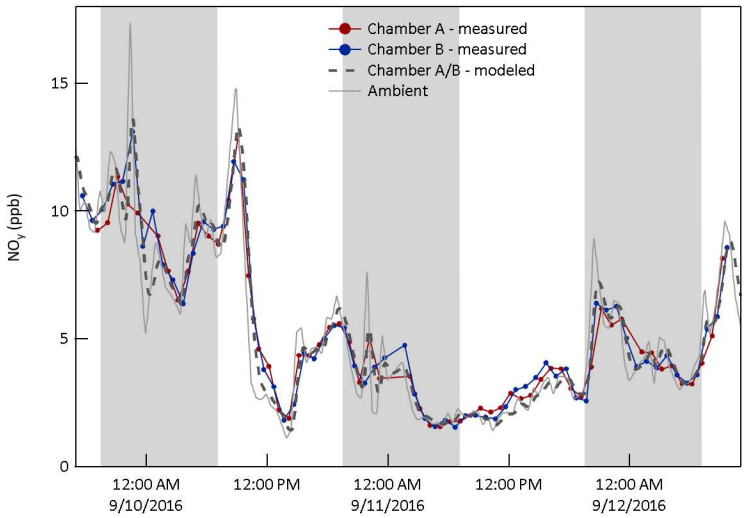

Figure 19. Time series of NO_y mixing ratio (ppb) measured in both chambers and just outside of them and calculated from the ambient time series assuming the chambers can be modeled as CSTRs with an exchange flow rate, Q_{ex}, of 33 L min^{-1}. The shaded bands represent nighttime.

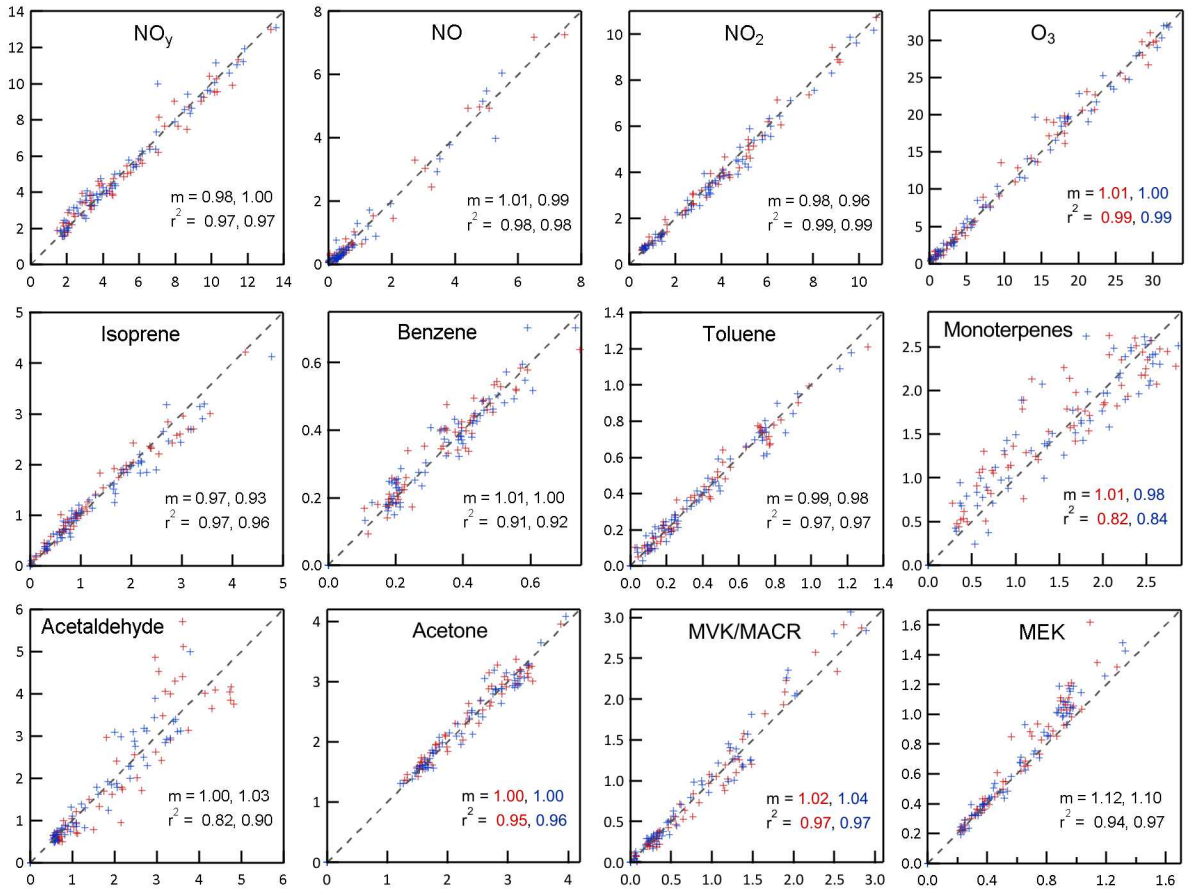

Figure 20. Relationships between mixing ratios (ppb) expected in the chambers calculated from the ambient time series using the CSTR-box model (x-axes) and measured in the chambers (y-axes). For all graphs the red markers and text are for Chamber A and the blue for Chamber B. The dashed lines shown in all graphs are 1:1 lines. The slopes, m, are for best-fit lines forced through the origin. MVK/MACR = methyl vinyl ketone/methacrolein, both of which are measured at the same mass by the PTR-MS. MEK = methyl ethyl ketone.

3.2.5.2 Compounds with production and loss terms

For all other measured species (or groups of species), chemical loss and production over the ~ 30 min residence in the chamber (based on volume divided by effective flowrate V_{ch}/Q_e) may be significant. For free radicals and other reactive or condensable species with typical atmospheric lifetimes much shorter than 30 min (e.g., hydroxyl radical, OH·, and nitrate radical, NO_3·), exchange across the ePTFE membrane is insignificant and P ≈ L in Equation 3.

A simple CSTR-box model was developed to interpret the results from the chamber-ambient comparison and to subsequently use ambient measurements made during the bioaerosol experiments to determine concentrations of measured and unmeasured species in the chambers. The model numerically integrates the time-dependent changes resulting from the 33 L/min gas

exchange and the reactions listed in Table 1. Only those reactions expected to have significant influence on the concentrations of measured or otherwise important species were included. Most photolysis rate constants were calculated from measured spectral intensity by researchers from University of Houston. The only exception is that for NO_2, which was instead calculated assuming ambient NO, NO_2, and O_3 concentrations satisfied the photostationary state relationship, $J_{NO_2} = k[O_3][NO]/[NO_2]$, where [ ] indicates concentration. Some reactions are intentionally not balanced when one or more of the products is not tracked in the model (e.g., $NO_3\cdot + RO_2\cdot \rightarrow NO_2$) and some reactions combine a series of steps with only that controlling the overall rate included (e.g., $NO_2 + h\nu \rightarrow NO + O_3$). The box model was used to calculate concentrations of measured (e.g., O_3, isoprene) and unmeasured (e.g., $OH\cdot$ and $NO_3\cdot$) gases and to estimate secondary aerosol production rates resulting from reactions of SO_2 with $OH\cdot$ and reactions of hydrocarbons with $OH\cdot$, $NO_3\cdot$, and O_3. Described below are measured and modeled concentrations for the $NO/NO_2/O_3$, isoprene/MVK+MACR, and O_3/acetaldehyde systems that, collectively, elucidate the relationship between conditions in the chamber and those outside.

Table 1. Reactions included in the CSTR-box model

Reaction	Rate coefficient ($cm^3\ s^{-1}$ unless stated otherwise)	Notes
$NO + O_3 \rightarrow NO_2 + O_2$	$1.40 \times 10^{-12} \exp(-1310/T)$	
$NO_2 + O_3 \rightarrow NO_3\cdot + O_2$	$1.40 \times 10^{-12} \exp(-2470/T)$	
$NO_2 + NO_3\cdot (+ M) \rightarrow N_2O_5$	$1.9 \times 10^{-12} (T/300)^{0.2}$	High pressure limit rate constant and expression
$N_2O_5 + M \rightarrow NO_2 + NO_3\cdot$	$1.30 \times 10^{-3} (T/300)^{-3.5} \exp(-11000/T)$	
$NO_3\cdot + NO \rightarrow 2NO_2$	$1.80 \times 10^{-11} \exp(110/T)$	
$OH\cdot + NO (+ M) \rightarrow HONO$	$1.50 \times 10^{-11} (T/300)^{-0.5}$	High pressure limit rate constant and expression
$OH\cdot + NO_2 (+ M) \rightarrow HNO_3$	$2.40 \times 10^{-11} (T/300)^{-1.3}$	High pressure limit rate constant and expression
$NO_3\cdot + RO_2\cdot \rightarrow NO_2$	2.00×10^{-12}	
$RO_2\cdot + RO_2\cdot \rightarrow$ products	2.00×10^{-12}	
$OH\cdot$ + acetaldehyde $\rightarrow RO_2\cdot$	$5.55 \times 10^{-12} \exp(287/T)$	
Photolysis reactions		
$NO_2 + h\nu \rightarrow NO + O_3$	J_{NO2}	Calculated assuming photostationary state for ambient NO, NO_2, and O_3 concentrations
$NO_3\cdot + h\nu \rightarrow 0.12NO + 0.88NO_2 + 0.88O_3$	J_{NO3}	Calculated from measured spectral intensity
$O_3 + h\nu \rightarrow 0.3OH\cdot + O_3$	J_{O1D}	Calculated from measured spectral intensity. Assumes 15% of $O(^1D)$ produced reacts with H_2O to form $OH\cdot$. O_3 is conserved because any shift this would cause would be captured in the estimated J_{NO2}.
$HONO + h\nu \rightarrow OH\cdot + NO$	J_{HONO}	Calculated from measured spectral intensity
Secondary aerosol forming reactions		
$OH\cdot + \alpha$-pinene $\rightarrow RO_2\cdot$	$2.54 \times 10^{-11} \exp(410/T)$	
$OH\cdot + \beta$-pinene $\rightarrow RO_2\cdot$	$1.21 \times 10^{-11} \exp(444/T)$	
$OH\cdot$ + isoprene $\rightarrow 0.6RO_2\cdot$ + 0.4MVK+MACR	$2.38 \times 10^{-1}1 \exp(357/T)$	
$OH\cdot$ + toluene $\rightarrow RO_2\cdot$	$1.81 \times 10^{-12} \exp(280/T)$	

$OH\cdot + SO_2 \rightarrow SO_4$	1.50×10^{-12}	
O_3 + α-pinene → $RO_2\cdot$	$6.30 \times 10^{-16} \exp(-580/T)$	
O_3 + β-pinene → $RO_2\cdot$	$1.20 \times 10^{-15} \exp(-1300/T)$	
O_3 + isoprene → $0.6RO_2\cdot$ + 0.4MVK+MACR	$1.03 \times 10^{-14} \exp(-1995/T)$	
$NO_3\cdot$ + α-pinene → $RO_2\cdot$ + $0.8NO_2$	$1.20 \times 10^{-12} \exp(490/T)$	
$NO_3\cdot$ + β-pinene → $RO_2\cdot$ + $0.3NO_2$	2.50×10^{-12}	
$NO_3\cdot$ + isoprene → $0.95RO_2\cdot$ + $0.3NO_2$ + 0.05MVK+MACR	$3.15 \times 10^{-12} \exp(-450/T)$	
Heterogeneous reactions		
$N_2O_5 + H_2O(\ell) \rightarrow 2HNO_3$	2.67×10^{-7} x S ($\mu m^2\ cm^{-3}$)	Aerosol surface area, S, assumed to be 100 $\mu m^2\ cm^{-3}$
Tuning reactions		
O_3 + wall → 0.65acetaldehyde + 0.12acetone	$1.00 \times 10^{-4}\ s^{-1}$ for A $0.70 \times 10^{-4}\ s^{-1}$ for B	Used to match observed O_3 loss and acetaldehyde and acetone production. Wall "concentration" dependent upon solar intensity to adjust for increase in contact frequency with increased convective mixing.
$OH\cdot + X \rightarrow$	$2\ s^{-1}$	Used to produce reasonable daily peak $OH\cdot$. Partially constrained by daytime difference between chamber and ambient isoprene resulting from reaction with $OH\cdot$.
(N_2+O_2) + wall → HONO	$1.0 \times 10^{7}\ s^{-1}$	Recognized radical source in Teflon chambers. Partially constrained by pattern of daytime difference between chamber and ambient isoprene resulting from reaction with $OH\cdot$.

- $OH\cdot$ is conserved for all "$OH\cdot$ + reactant →" reactions because an independent overall $OH\cdot$ reactivity is assumed.
- Species in parentheses involved in reaction but not needed for calculated rate.
- Chamber temperature assumed to be the same as ambient temperature

Whereas the concentration of the sum of all nitrogen oxides (= NO_y) is roughly conserved over the chamber-ambient mixing time, that of its more reactive components may not be. During the daytime, steady state cycling between NO, NO_2, and O_3 minimizes any differences between chamber and ambient concentrations. But at night, reaction of O_3 with both NO and NO_2 results in concentrations in the chamber that are, conceptually, what would be expected ~30 min (= V_{ch}/Q_{ex}) downwind. The model captures the influence of the reactions, resulting in close agreement between the expected and measured mixing ratios for both NO and NO_2, as is evident in the time series in Figure 21 and in the clustering of points around the 1:1 lines in Figure 18. For clarity, only the results for one of the two chambers (B) are shown in the time series, while the measurement/model pairs from both chambers are shown in Figure 20.

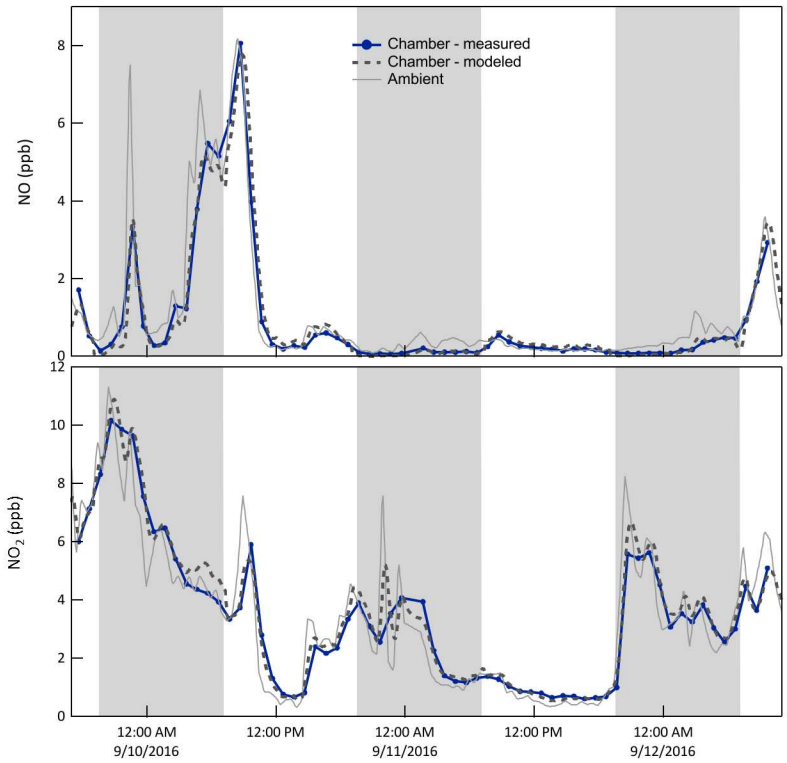

Figure 21. Time series of NO and NO_2 mixing ratios i) measured and ii) expected in the chamber (B), and iii) measured outside. Smoothing of the spikes in the ambient time series results from treatment of the chamber as a CSTR. The slightly lower NO and slightly higher NO_2 at night results from the reaction NO + O_3 → NO_2 + O_2. The combined effect is that the composition in the chamber is that expected about 30 min downwind of its physical location.

Oxidation of reactive hydrocarbons by OH·, O_3, and NO_3· creates a mixture of products that may subsequently react or may condense on the particles that were injected into or formed within the chamber. Biogenics, including isoprene and the monoterpenes, were typically the most concentrated hydrocarbons at the forested site. Isoprene chemistry was most important during the daytime as its emission rate is largely controlled by solar intensity, whereas the temperature-dependent emission of the monoterpenes varies comparatively little throughout the day/night. Figure 22 shows the influence of in-chamber chemistry on the mixing ratios of isoprene and its oxidation products MVK+MACR (only the sum of the two measured with PTR-MS). During the daytime and early evening when concentrations of OH· and O_3/NO_3·, respectively, are high both the expected and measured mixing ratios of isoprene are lower and those of MVK+MACR are higher than those measured outside. For both species the CSTR-box model captures the features in the time series quite well with resulting average best fit slopes and r^2 of 0.95 and 0.97 for isoprene and 1.03 and 0.97 for MVK+MACR.

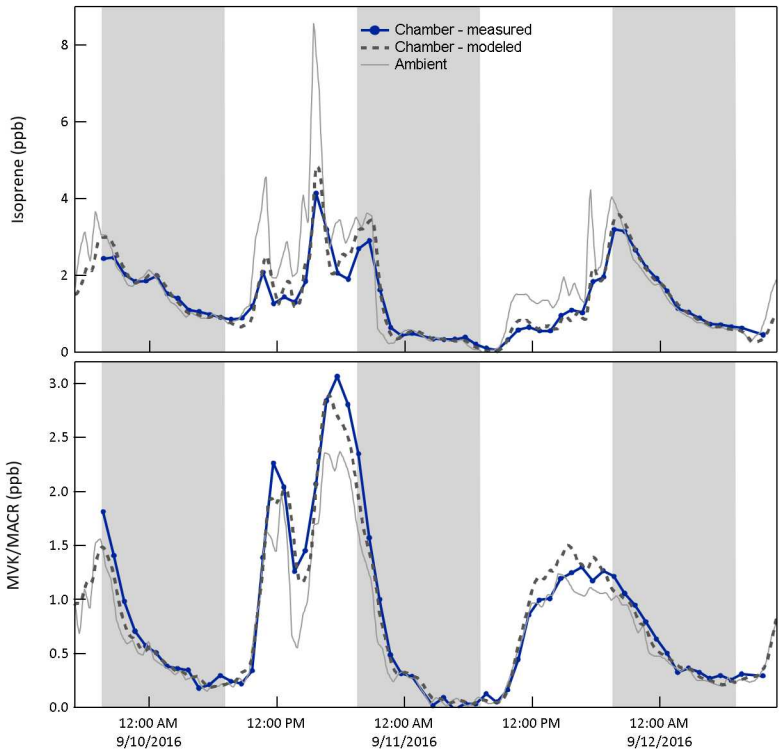

Figure 22. Mixing ratio time series of isoprene and its reaction products methyl vinyl ketone+methacrolein. Note the concentration expected in the chamber, measured in the chamber, and measured outside. Isoprene that enters through the ePTFE membrane reacts with OH·, O_3, and NO_3· in the chamber, resulting in a lower mixing ratio than outside. Products from those isoprene oxidation reactions include methyl vinyl ketone and methacrolein, which are consequently present at higher mixing ratio in the chamber than outside.

For almost all species, the concentrations measured in the chambers agree well with those calculated from the ambient measurements as is reflected in the near 1.0 best-fit slopes and high r^2 values shown in Figure 20. There is more scatter about the 1:1 line for the monoterpenes, which is largely the result of noise in the measurements as the mixing ratios were close to the detection limit for most of the comparison period. Because the PTR-MS cannot distinguish between monoterpenes with the same molecular weight, differences in the relative abundance of each monoterpene species may also contribute noise and uncertainty to this plot. Measured concentrations of MEK were generally higher than predicted simply because it is produced in the chamber from oxidation of species such as butane that were not measured, and therefore not included in the model.

Reaction of O_3 with the Teflon walls and/or impurities on those walls results in a slightly lower concentration in the chamber than outside, as shown in the top time series in Figure 23. To represent this in the model, an O_3 + Wall reaction was included and its rate constant adjusted to match the observations in each chamber. Additionally, as has been reported elsewhere (e.g., de Gouw and Warneke, 2007) surface reaction of O_3 produces acetaldehyde, which explains the high concentrations observed in the chamber shown in the bottom graph of Figure 23. Thus, an acetaldehyde yield from the O_3 + Wall reaction was used as an additional tuning parameter. With

the corrections, the modeled O_3 matches that observed very well, with average best-fit slope of 1.00 and r^2 of 0.99. The corresponding values for acetaldehyde are 1.02 and 0.86.

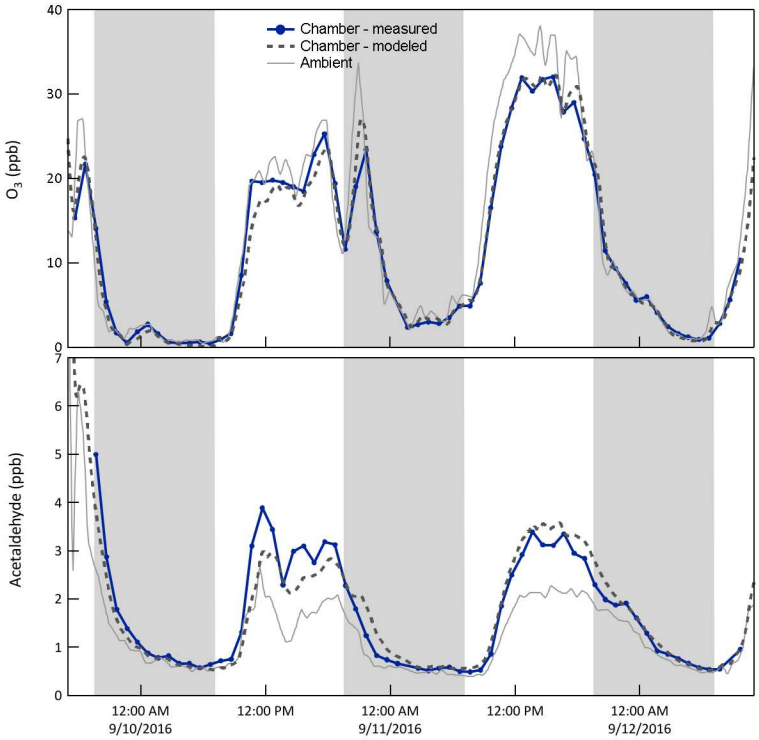

Figure 23. Time series of O_3 and acetaldehyde mixing ratios. Note the measured, expected concentration in the chamber, outside measurement. Ozone mixing ratios were slightly lower in the chamber than outside, which is believed to be the result of reactions with the Teflon surfaces or with impurities on those surfaces. The loss rate constant was adjusted to match the observations. A product of the O_3+wall and possible other reactions is acetaldehyde, resulting in higher than ambient concentrations in the chambers.

The only other tuning parameters in the model were used to estimate OH· concentration. Specifically, an overall OH· + X loss rate of 2 s^{-1} (or τ = 0.5 s) was assumed, as was a continuous source of nitrous acid, HONO. Photolysis of that HONO and of the modeled O_3 were assumed to be the only OH· sources. While the resulting OH· concentration is not well constrained, the daily profiles and maxima seem reasonable for the site location and the modeled influence of OH· on reactive species such as isoprene is consistent with that observed. Overall, the improved understanding of the CAGE chambers in general and the CSTR-box model in particular that came from the chamber-ambient comparison experiment increases the accuracy with which changes in bioaerosols could be connected with the responsible environmental conditions.

3.2.6 Particle Lifetime In Chambers

The CAGE chambers were designed to permit experiments on captive aerosols for periods ranging from hours to more than a day. The discussion above reveals why the use of a gas permeable membrane is necessary to do so. If the more traditional approach of continuously adding and extracting a flow were used the particle lifetime would be too short for flow rates comparable to Q_{ex} (τ ~ 30 min), while the gas phase composition would differ too much from that outside if a

much lower flow rate was used. Thus, diffusion-only exchanging of gases and not particles, makes it possible to conduct long-duration experiments under ambient conditions. Particle retention is further increased by rotating the chambers and by taking steps to minimize static charge on the Teflon surfaces.

Figure 24 summarizes the resulting distribution of lifetimes during the 2016 study for different particle size populations and identifies the techniques and instruments used to quantify them. The three histograms represent particle lifetime distributions for distinct particle populations that were simultaneously present in the chambers (their roles are described below). As expected, loss rates are lowest and lifetime highest for the ~0.3 μm diameter particles (D_p) that are in the size range at which the combined influence of diffusional and settling losses reaches a minimum. The average lifetime of the $(D_p)_{avg}$ = 2.4 μm bioparticles was 3.9 h. Even neglecting losses due to sample flow extraction and electrostatic attraction, a lifetime of less than 1 h would be expected for a non-rotating chamber with the same 0.53 m radius and the same 2.4 μm particles, which have a settling velocity of about 0.65 m h^{-1}. Loss rates were typically highest during the daytime as solar heating promoted convection in the chambers.

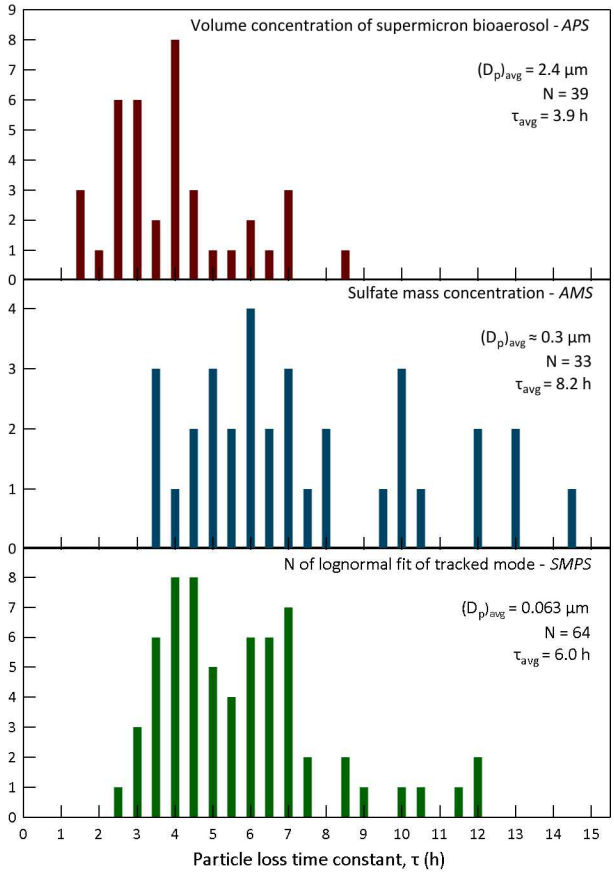

Figure 24. Exponential time constants for particle loss in the chambers during the 2016 study. The top graph presents the distribution of lifetimes of injected bioparticles with an average diameter of 2.4 μm. The loss rates were determined from exponential decay fits to the supermicron volume concentration calculated from measurements by an aerodynamic particle sizer (APS). The middle graph presents the distribution of lifetimes of ~0.3 μm diameter sulfate particles intermittently injected to maintain a stable surface area concentration in the chambers. The loss rates were determined from exponential decay fits to the sulfate mass concentration measured with an

aerosol mass spectrometer (AMS). The bottom graph presents the distribution of lifetimes of "tracked mode" particles having an average diameter of 0.063 μm. The loss rates were determined from exponential decay fits to the number concentration parameter of lognormal fits to the narrow mode distributions measured with a scanning mobility particle sizer (SMPS).

Simply taking the average of the lifetimes for the three particle populations and corresponding size ranges gives a particle lifetime of 6.0 h. This is quite high for such a small chamber with a correspondingly high surface area to volume ratio. In fact, it is higher than those reported for much larger chambers used to study secondary aerosol formation as summarized in Table 2, which was copied from Wang et al. (2014). A caveat of the simple comparison with other chambers is that for CAGE the lifetimes were averaged over daytime and nighttime conditions whereas for at least some of the other chambers the values were determined during daytime or when artificial lights were activated.

Table 2. Comparison of chamber particle loss rates. Copied from Wang et al. (2014) with CAGE data added.

Chamber	Volume (m^3)	Wall material	Wall loss rate (h^{-1})	Particle lifetime (h)
CAGE	1	FEP	0.17	6.0
GIG-CAC	30	FEP	0.17	5.9
PSI	27	FEP	0.21	4.8
Caltech	28	FEP	0.20	5.0
UCR	90	FEP	0.29	3.4
EUPHORE	200	FEP	0.18	5.6
SAPHIR	270	FEP	0.27	3.7
CMU	12	FEP	0.40	2.5

3.2.7 Particle Injection and Sampling Strategy

Among the processes that may impact the bioaerosol is production of secondary aerosol species that condense on, or dissolve in, the bioparticles. Though the process will result in growth, the typical rate of change in diameter of a few nm h^{-1} is undetectable for the ~2,000 nm bioparticles. Thus, a mode of smaller particles is co-injected and its measured growth rate ($GR = \frac{dDp}{dt}$)used as a proxy for the rate of addition to the bioparticles. Ammonium sulfate was selected because of its common use as a seed aerosol in chamber studies and because it often represents a significant component of atmospheric aerosols.

To accurately quantify changes that are typically between -1 and 10 nm h^{-1}, the atomized aerosol is first size-selected with a differential mobility analyzer (DMA) to generate a monodisperse population. Throughout the experiments a scanning mobility particle sizer (SMPS) is used to measure the particle size distribution in each chamber roughly twice per hour. The tracked mode size distribution is fitted using a lognormal function and the D_p and N parameters of the fits used to calculate particle growth rate and loss rate, respectively. During the 2015 study the co-injected mode was added to the chamber just prior to the bioaerosol and was tracked only during the ~4 h duration experiments. For the 2016 study, the generation and sampling systems were automated and a new monodisperse mode was added as soon as the previously injected mode became difficult to track. With this change in approach growth rate was determined nearly 24 hours per day, which

provided a better understanding of the controls of aerosol production at the site and provided context for the conditions during the bioaerosol experiments.

Condensable species that are produced are expected to be distributed among the particle population in the chamber. The division among those particles can depend on properties of the condensable species and of the particles, though these results suggest a simple particle surface area dependence. Because of competition for the condensable species among all particles in the chamber the growth rate of the tracked mode will be affected by the total surface area concentration. To minimize that influence an additional monodisperse mode centered at 0.3 μm was maintained with new injections triggered automatically each time the surface area concentration calculated from the SMPS-measured size distribution fell below 40 μm^2 cm^{-3}. The result is shown in the example 2-week time series of surface area concentration in Figure 25.

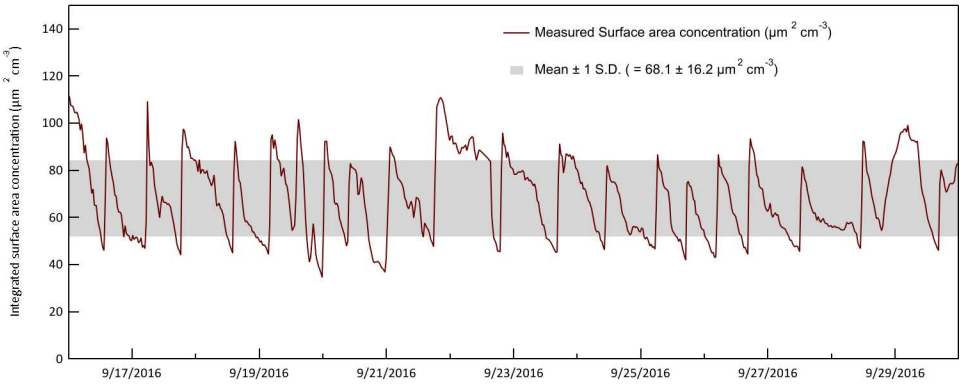

Figure 25. Two week time series of integrated surface area concentration in Chamber B calculated from size distributions measured by the SMPS. The periodic step change increases correspond to automated injections of ~0.3 μm ammonium sulfate particles intended to maintain a stable surface area concentration in the chamber.

In addition to the injected ammonium sulfate and bioaerosol particles, new particle formation (NPF) events would sometimes occur inside the chambers just as they do in the atmosphere. The nucleation or NPF modes are broad relative to those injected, but are still typically narrow enough to track. Figure 26 shows an example of the chamber size distributions measured by the SMPS over a 3.5 day period during the 2016 study. The modes labeled IM are the injected monodisperse ammonium sulfate modes and those labeled NM are nucleation modes consisting of particles that formed and grew within the chamber. The repeated injections into the surface area mode (SAM) results in the ~horizontal band centered at about 0.3 μm. To the right of the intensity graph is an x-y representation of the size distribution measured at the time indicated by the rectangular box. Also shown in the x-y graph is the particle surface area concentration size distribution, which highlights the extent to which the total concentration can be controlled by the SAM and is minimally impacted by the smaller particle tracked mode.

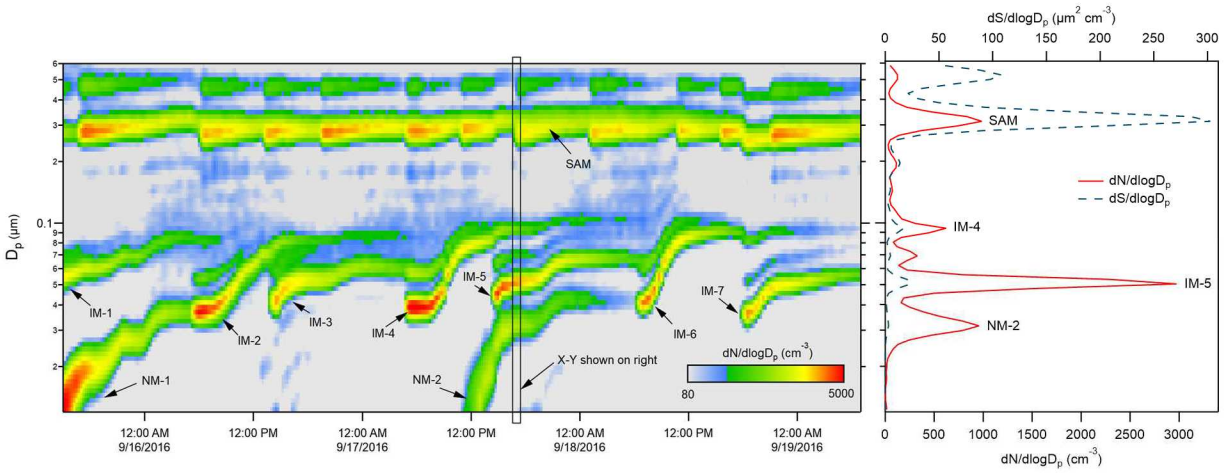

Figure 26. Left: Size distribution time series over 3.5 days during the 2016 study. IM = injected mode, NM = nucleation mode, SAM = surface area mode. Right: x-y presentation of the size distribution measured at the time indicated by the rectangle in the time series. N = number concentration and S = surface area concentration.

As noted above, the tracked modes are fitted with log-normal fits to extract the time-dependent mode diameters. The result for the same 3.5 day period is shown in Figure 27, where each of the curves represents one tracked mode. Different colors are used for different modes that overlapped in time and shaded bands are included to designate nighttime. The x-y representation to the right shows the lognormal fits to the same nucleation mode and two injected modes identified in Figure 26. The compilation of the growth curves of all of the modes tracked during the 2016 study is presented in Figure 28. The color bar towards the top of the graph indicates the periods during which at least one mode was tracked and growth rate could be determined.

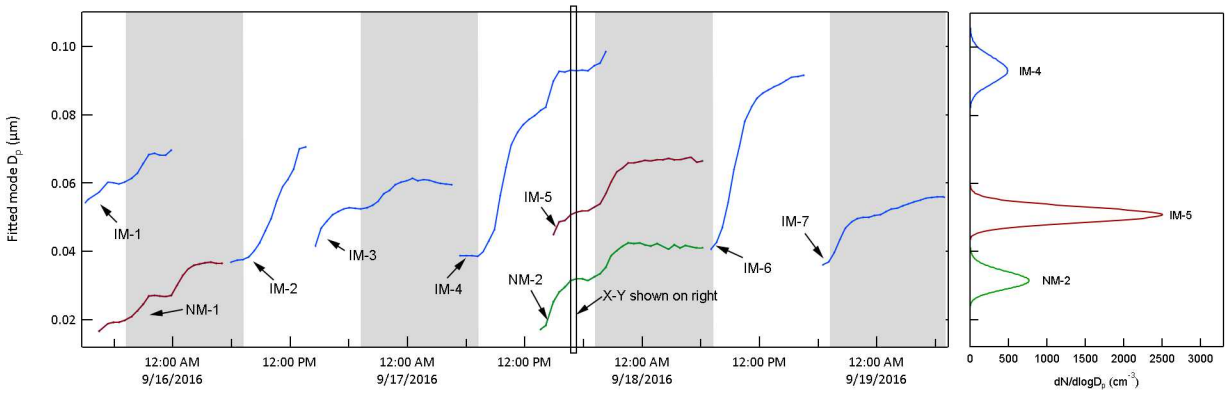

Figure 27. Left: Time series of the lognormal fit diameters of injected and nucleation modes identified in Figure 24. Different colors are used when two or modes overlap in time. Right: Lognormal fits to the three modes tracked at the time indicated by the rectangle in the time series.

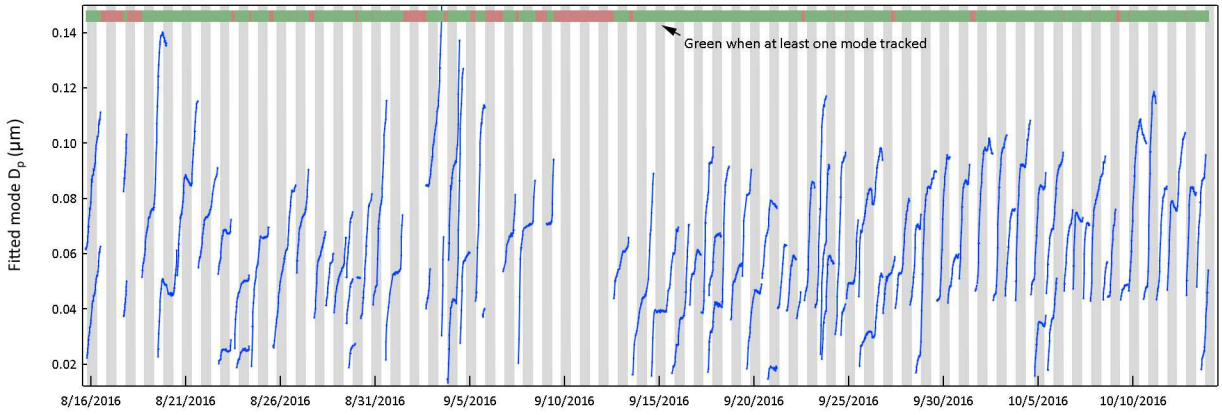

Figure 28. Time series of lognormal fit diameter to all modes tracked during the 2016 study.

Finally, for each tracked mode the growth rate is calculated as the change in lognormal fit D_p between two successive measurements divided by the time difference between them, as specified above, and presented in Figure 29 for the same 3.5 day example period. It is that GR as a function of time that reflects the rate at which bioparticles were coated by secondary aerosol and that may be correlated with observed changes in their viability or detection properties.

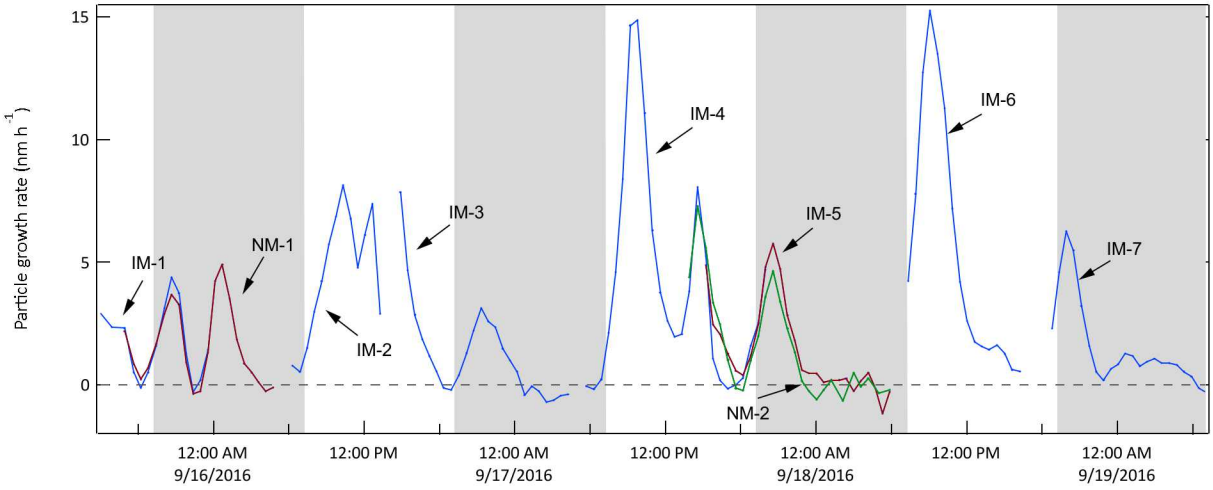

Figure 29. Particle growth rates calculated from the time series of lognormal fit diameters shown in Figure 25. The different colors correspond those used in Figure 25.

An important feature in Figure 29 is the similarity in GR among multiple modes that were tracked simultaneously. This lack of size dependence suggests condensation for these reactions is controlled by surface area. It simplifies use of this calculation, as a diameter-dependent correction would otherwise be required. Figure 30 shows the comparison of all growth rates calculated from simultaneously tracked modes. The general clustering around the 1:1 line further suggests the growth rate is independent of particle size and growth is dependent only on particle surface area.

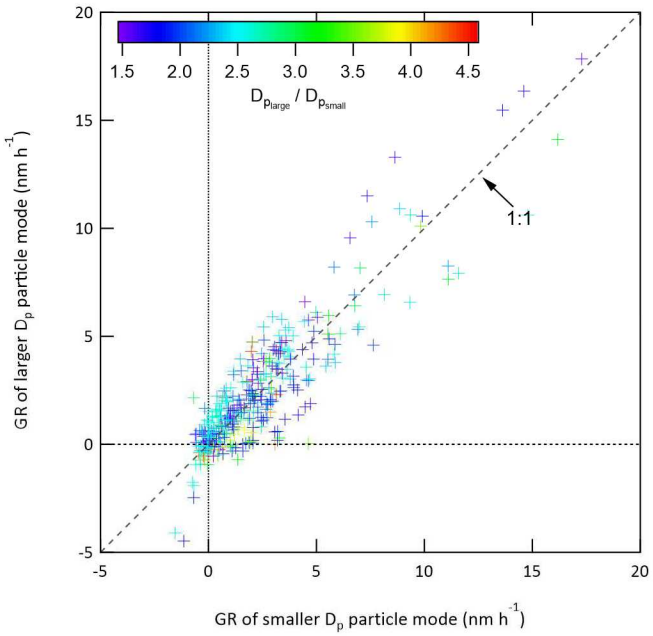

Figure 30. Comparison of all pairs of growth rates calculated for multiple modes tracked at the same time. The GR of the smaller diameter mode is plotted on the x-axis and that of the larger diameter mode on the y-axis. The ratio of the diameter of the lognormal fit to the larger particle mode to that of the smaller particle mode is indicated by marker color. The lack of a strong size dependence in the growth rates suggests addition of secondary aerosol mass varies with particle surface area.

3.2.8 Connecting Gas Phase and Aerosol Phase Measurements with Aerosol Production Estimates

Quantifying secondary aerosol formation in a chamber by diameter growth rate, as done here, is atypical. Almost all chamber studies instead measure and report the change in particle volume or mass concentration over time. The result can conveniently be related to secondary aerosol mass yields, which can then be used in atmospheric models that predict aerosol production following reaction of various precursors. However, those other chamber experiments can use precursor and oxidant concentrations much higher than observed at locations such as JSF, particularly at times corresponding to the growth rate minima commonly observed in the early morning and late afternoon. Evidence of the difficulty of tracking secondary aerosol mass production in ambient concentration chambers such as these is presented in Figure 31. That figure shows the GR time series from Figure 29, together with the organic aerosol production rate, dM_{org}/dt calculated from measurements made with an Aerodyne high resolution-time of flight-aerosol mass spectrometer (HR-TOF-AMS). Though production of inorganic sulfate and nitrate aerosol could also contribute to the total aerosol production rate, the organic component is expected to dominate at forested sites such as JSF. The rate of change of organic aerosol mass was corrected for losses due to flow extraction and wall deposition by normalizing with respect to the concurrently measured sulfate aerosol concentration,

$$\frac{dM_{org}}{dt} = \frac{\left(M_{org}\right)_{i+1} - \left(M_{org}\right)_i \frac{\left(M_{SO_4}\right)_{i+1}}{\left(M_{SO_4}\right)_i}}{t_{i+1} - t_i}$$

Equation 4. Correction via Organic Mass Flux (dM/dt)

Data was used only from those periods during which M_{SO_4} exhibited the characteristic exponential decay expected as the initially high concentration from an injection falls due to a constant loss rate. The top graph in Figure 31 shows those decay profiles and corresponding loss time constants. Though averaging the results over longer time periods would reduce the noise, it would also reduce the utility of the data as the time dependence would be obscured.

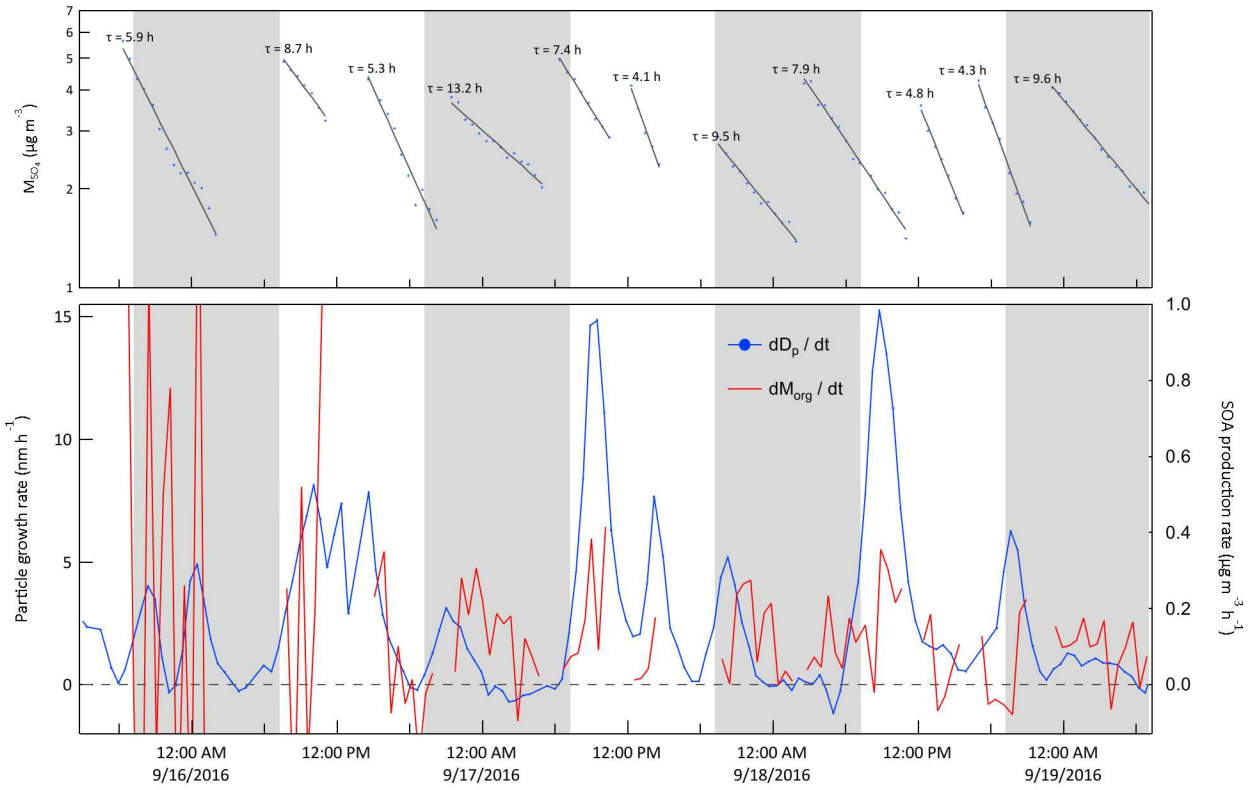

Figure 31. Top: Sulfate mass concentration in Chamber A measured with the AMS during the same 3.5-day example period as in Figures 26, 27, and 29. The lines and time constants are for the exponential decay fits to the concentrations. Bottom: Averaged diameter growth rate from Figure 29 (blue) and calculated rate of change of organic aerosol mass concentration (red). The rate of change of the organic mass concentration was corrected for loss using the sulfate mass as described in the text. The contrast between the two highlights the challenge in quantifying secondary aerosol production under ambient conditions using measurements of aerosol volume or mass concentration and motivates instead tracking narrow size distribution modes.

The diel profile of growth rate averaged over the full study period is shown in Figure 32. The two colored bands (yellow and blue) span the average start and stop times of the daytime and nighttime bioaerosol experiments. The nighttime experiment start times varied little during the study whereas there was more variability in those of the daytime experiments.

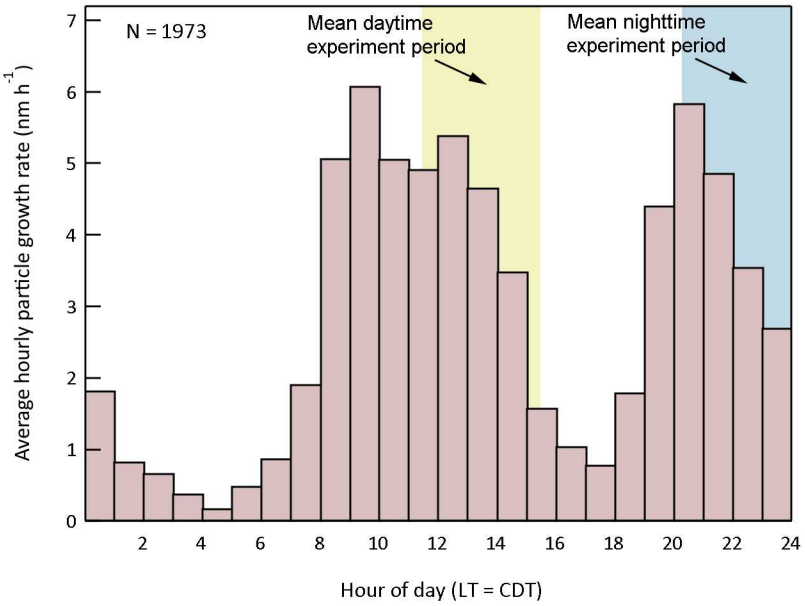

Figure 32. Distribution of particle growth rate during the 2016 study. A total of 1,973 values were used to construct the histogram. The shaded bands represent the average periods of the daytime and nighttime bioaerosol experiments.

The bimodality evident in Figure 31 results from active OH·-driven aerosol production during the day and NO_3·- and O_3-driven production at night. The decision to return to Jones State Forest in 2016 and to conduct daytime and nighttime experiments was motivated by this daily pattern and the potential to exploit it to disentangle the influence of chemistry from that of exposure to solar UV.

Figure 33 shows the daily profiles of the mean and 25th to 75th percentile interquartile range for the important oxidants (OH·, O_3, and NO_3·) as well as the most important anthropogenic (toluene) and biogenic (isoprene and the monoterpenes) secondary organic aerosol precursors. The average GR profile from Figure 32 is also included in each of the columns of graphs in Figure 33 to more clearly show the connection between the gas phase concentrations and the resulting aerosol production. The similarity between the OH· and daytime GR profiles and between the NO_3· and nighttime GR profiles is evident. The leftward shift in the daytime GR profile relative to that of OH· and the rightward shift in the nighttime GR profile relative to that of NO_3· largely reflects variation in the hydrocarbon precursor concentrations as the aerosol production rate is proportional to the product of the oxidant and precursor concentrations. Most importantly, the concentrations of both toluene and the monoterpenes decrease during the morning as the mixed layer deepens and then increase in the early evening as the pattern reverses and vertical mixing is limited.

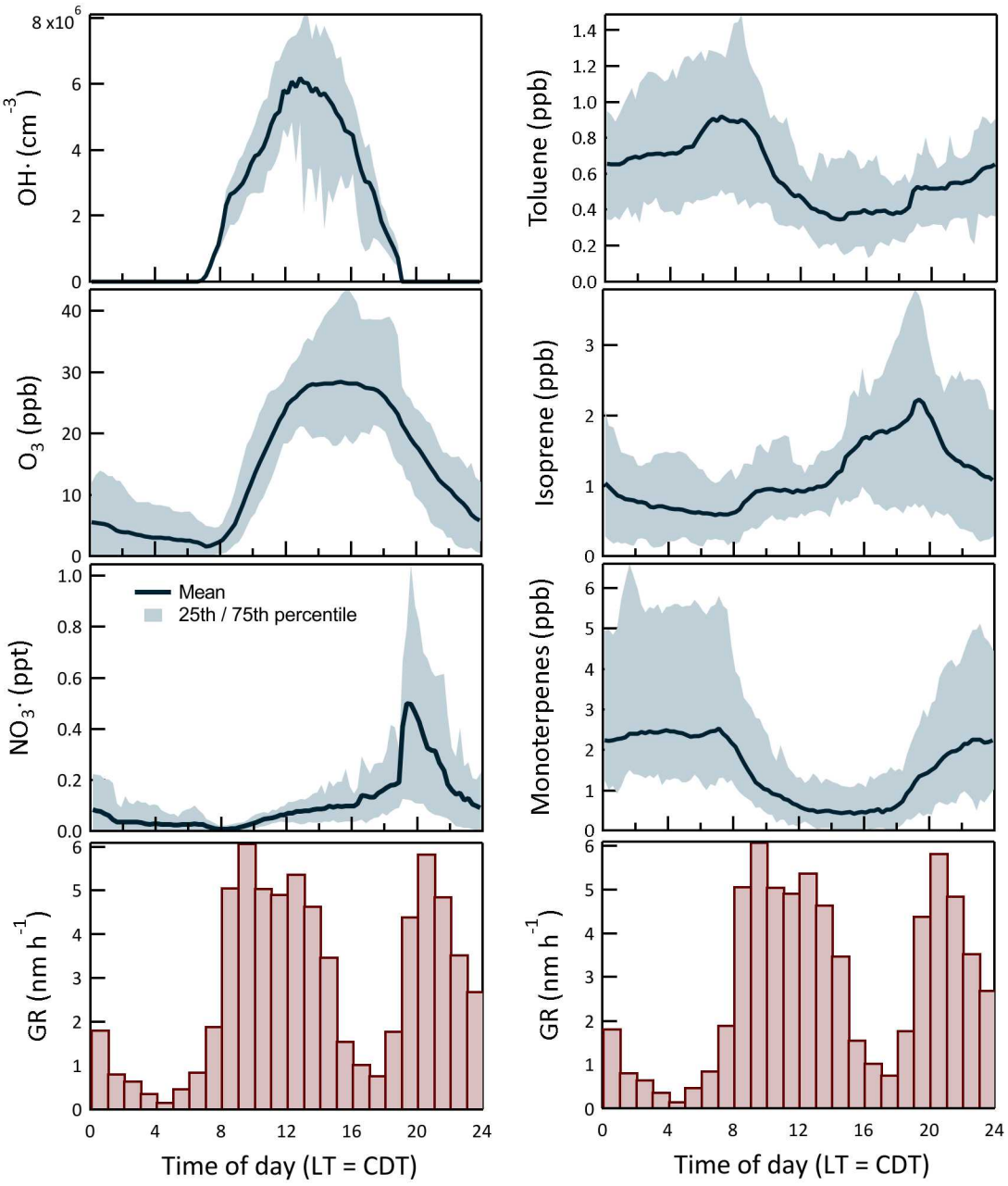

Figure 33. Time of day-dependent mean and 25th/75th percentile for the most important oxidants and secondary organic aerosol precursors. The averaged particle growth rates from Figure RRR are shown at the bottom to help visually compare the gas phase concentration and particle growth patterns.

Support for the broad interpretation of the relationship between the patterns in the GR and gas phase concentrations in Figure 33 comes from estimates of secondary aerosol production rate with the CSTR-box model. The results are used to further interpret temporal variability in GR during the day/night and between days and to assess correlations between changes in the bioaerosol and rates of aerosol production resulting from specific oxidant and/or precursor combinations. The estimated aerosol production at each time step is calculated as:

Equation 5. Production of Secondary Aerosol

$$P_{SA} = \frac{1}{N_A}\sum_i k_i[Precursor][Oxidant]MW_{precursor}Y_i'$$

, where P_{SA} is the secondary production rate, N_A is Avogadro's number, k_i[Oxidant][Precursor] is the reaction rate between an oxidant and precursor, MW is the molecular weight of the precursor, and Yi' is an effective aerosol production yield that was adjusted such that (arbitrarily) the value of P_{SA} (in μg m^{-3} h^{-1}) closely matched that of GR (in nm h^{-1}). The goal was to evaluate how well the model could explain the time dependence of the observed growth and not to retrieve mass-based aerosol yields.

As is shown in Figure 34 the calculated production rate captures the variation in GR over the same example 3.5 day period highlighted in Figures 26, 27, 29, and 31. During this period and for the remainder of the study the quality of the fit to the nighttime measurements of GR was generally significantly better than that for the daytime measurements. Among the contributors to uncertainty in the daytime estimates are the poor constraint on OH· concentration, and the exclusion of some precursors such as the xylenes that react efficiently only with OH· and for which measured concentrations were very noisy and rarely above the detection limit of the PTR-MS. The profile of the nighttime production rate was relatively insensitive to how it was partitioned between SOA production by O_3 and by NO_3·. Ongoing analysis of the aerosol mass spectrometer data by Rice University researchers should provide additional constraint on the relative importance of the two oxidants and the resulting distribution of aerosol phase products. Nevertheless, the general agreement between calculated secondary aerosol production rate and measured growth rate provides added confidence in the model output and in any attribution of the factors responsible for changes in the bioaerosol.

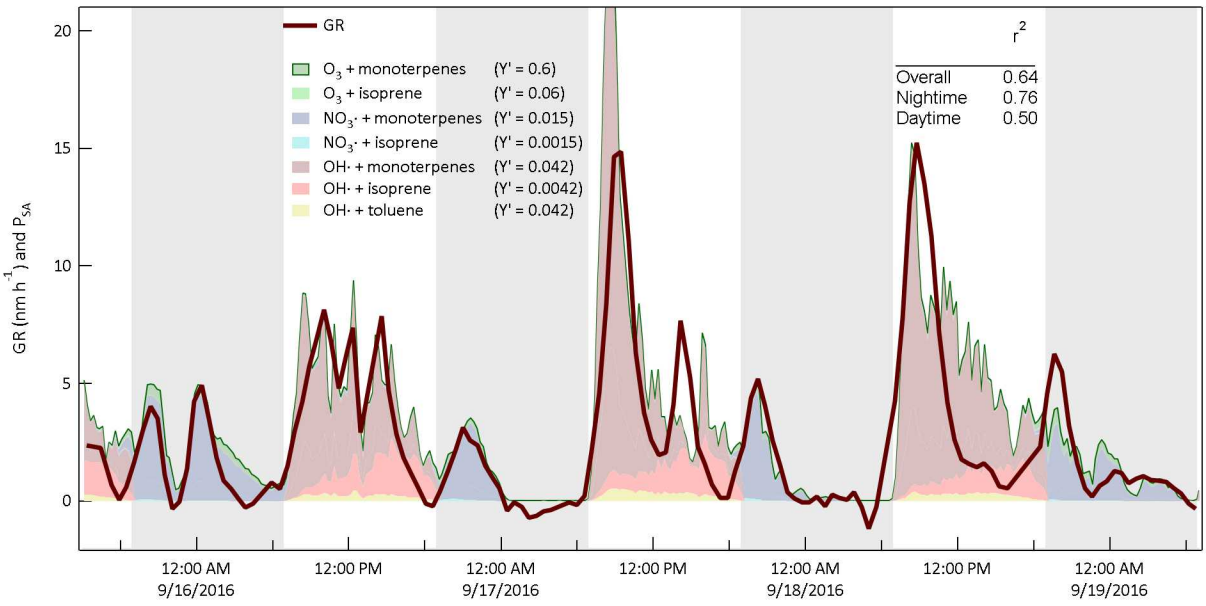

Figure 34. Measured diameter growth rate (GR) and calculated secondary aerosol production rate (P_{SA}) for the same 3.5 day example period. Effective aerosol yields for the reactions considered were adjusted to minimize differences between the values of GR (in nm h^{-1}) and PSA (in μg m^{-3} h^{-1}).

3.3 Surrogate Production

Bacillus thuringiensis al hakam (*B.t.)* was grown from a frozen master stock, by streaking on Luria Bertani (LB) agar plates for single colony isolates, and incubating at 37°C overnight. Individual colonies were used to inoculate 4-5 mL of LB broth, again incubated overnight at 37°C, 250 RPM. Overnight cultures were used as inoculum in larger scale flasks containing up to 500 mL of sporulation medium, modified from Nicholson & Setlow (1990). Each flask was incubated at 37°C and 250 rpm. Sporulation continued for a total of three days at 37°C, and monitored for the presence of spores using phase-contrast microscopy. Spores were washed one time in an equal volume of Phosphate-buffered saline (PBS) and resuspended in nanopure water. Resulting spore preparation titers were determined by serially diluting and plating 1 mL of suspension onto 3M Petrifilm, incubating at 37°C overnight, and counting resulting colonies.

MS-2 bacteriophage propagated in an *E. coli* A/λ strain host. Host *E .coli* cultures were streaked from glycerol stocks and incubated overnight on LB agar at 37°C for individual colonies. Colonies were placed into 10 mL LB broth, and incubated (37°C, 250 RPM) overnight for scale-up of production. A 500 µl aliquot of overnight culture was used to inoculate 50 mL of LB broth in a baffled flask, until log-phase culture was achieved, as monitored by spectrophotometer (Eppendorf Biophotometer), based on absorption at 600 nm. Refrigerated MS-2 stocks served as inoculum for the mid-log phase *E. coli*, with 500 µL used to inoculate the 50 mL mid-log host. Incubation of the suspension continued at 37°C, 250 RPM overnight. After filter-sterilization at 0.22 µm, to remove cell lysate and any residual bacteria, MS-2 stock was kept at 4°C for up to one month. Time zero aerosol samples were monitored for any decrease in concentration, to indicate that the stock had aged significantly (Figure 35).

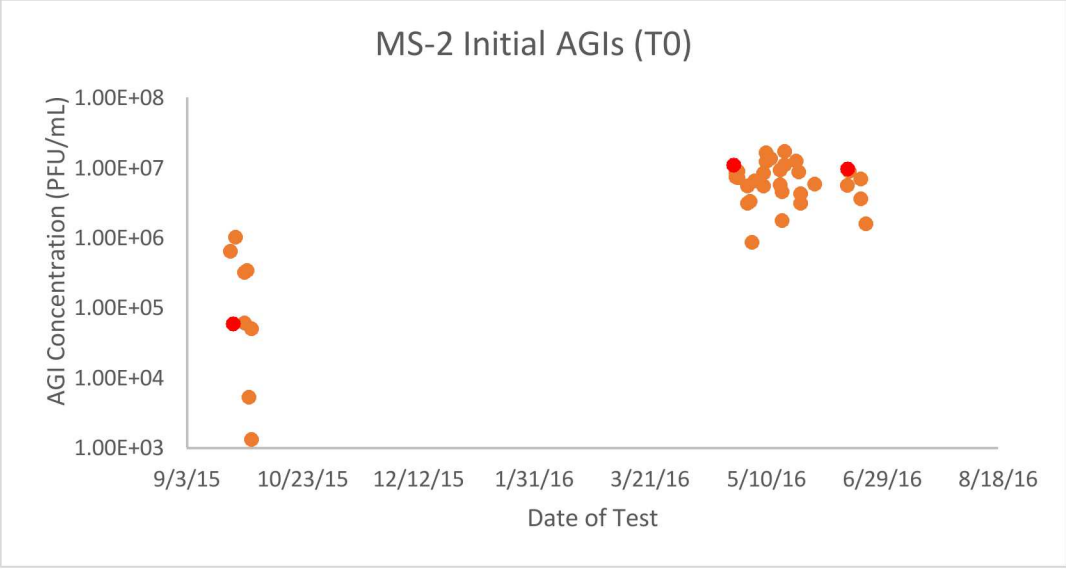

Figure 35. MS-2 change in initial AGI concentration over time. Samples with a red dot indicate a new stock.

Escherichia coli K-12 strain was also propagated from frozen stocks streaked for single colony isolates on LB agar, and incubated overnight at 37°C. Single colonies were scaled up to 10 mL overnight, then 500 ul of that overnight, scaled to 50 mL of LB and incubated overnight at 37°C, baffled flask and 250 RPM. Stock concentrations were determined by serially diluting and plating of 1 mL replicates on Petrifilm, enumerated after overnight incubation at 37°C. Final titers varied from 8.33E9 to 1.16E10 CFU/mL, and were kept in spent media for up to one month. Similar to MS-2, time zero aerosol samples were monitored for changes to indicate significant degradation (Figure 36). For all test conditions, the testing matrix was randomized, so that aging conditions were independent of the age of the bacterial stock.

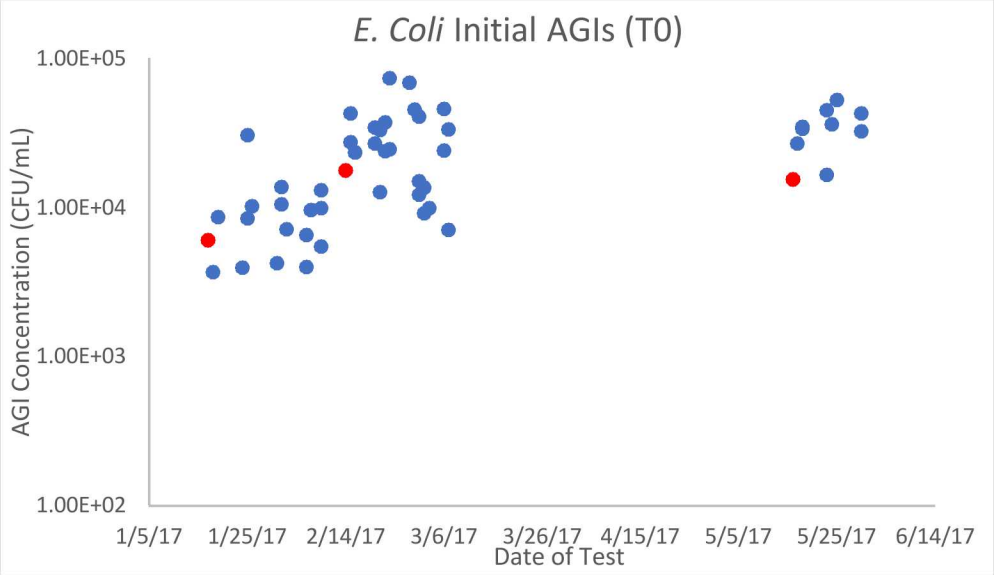

Figure 36. *E. coli* change in initial AGI concentration over time. Samples with a red dot indicate a new stock.

3.4 Aerosolization Methodology

Aerosolization suspensions were produced daily by diluting stock biological materials to achieve a mass median aerodynamic diameter (MMAD) of 2-3 µm. The target diameter was chosen for its likelihood to contain multiple organisms per particle, and to improve initial fluorescent particle signals, to better characterize the resultant changes due to aging, with a larger dynamic range in signal. *B.t.* al hakam was diluted with equal parts DI water, to a final concentration of 2.83E+09 CFU/mL. Resulting suspensions were injected at a rate of 100 µL/minute into the aforementioned 10 lpm aerosol carrier air stream. This aerosol was continuously generated until the number concentration in the drum was above 200 particles/cc, which equates to approximately 15 minutes. Initial mass distributions for *B.t.* al hakam can be seen in Figure 37.

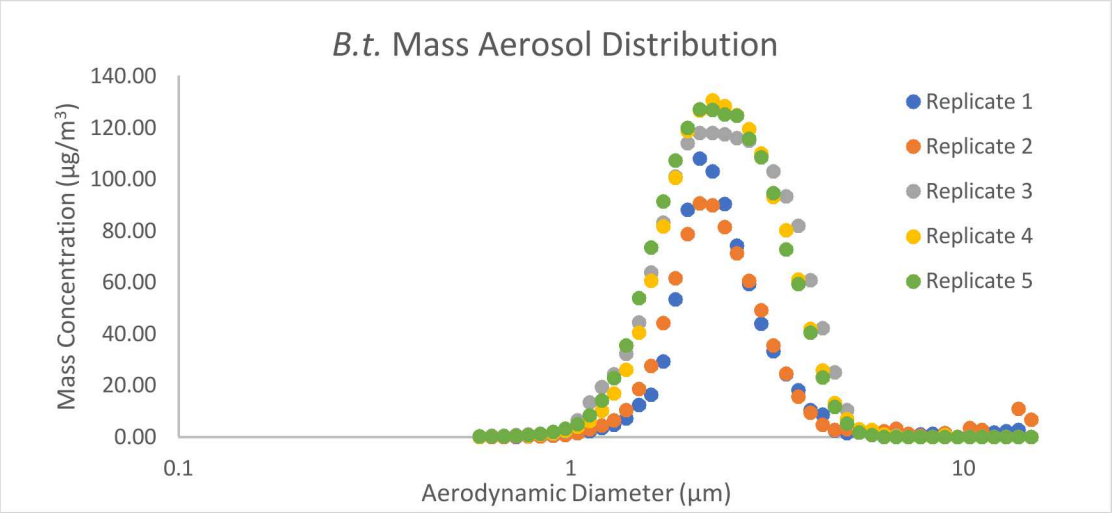

Figure 37. *B.t.* Mass aerosol distributions determined by an APS. Randomized selection of 5 trials as an example of aerosol distribution and variance.

Aerosol suspensions of *E.coli* K-12 were created daily by diluting refrigerated stocks in sterile-filtered DI water, to lower the contribution of dissolved solids from the spent media to the final dry particle size. A total of 95% water to 5% *E. coli* in spent medium was utilized, resulting in an aerosol suspension concentration of 4.98E+08 CFU/mL. Injection settings were consistent with *B.t.* at 100 µL/minute into 10 lpm of carrier air. Similarly targeting a dry particle size of 2-3 µm, initial MMAD distributions can be seen in Figure 38, which represents a random sample of *E. coli* dry aerosol distributions. Because *E. coli* in LB demonstrated some hygroscopic properties, size distributions at both the end of a test, and during initial aerosolization varied from the repeatable results that occurred in the presence of non-humidity variables (ozone, VOCs, and UV light).

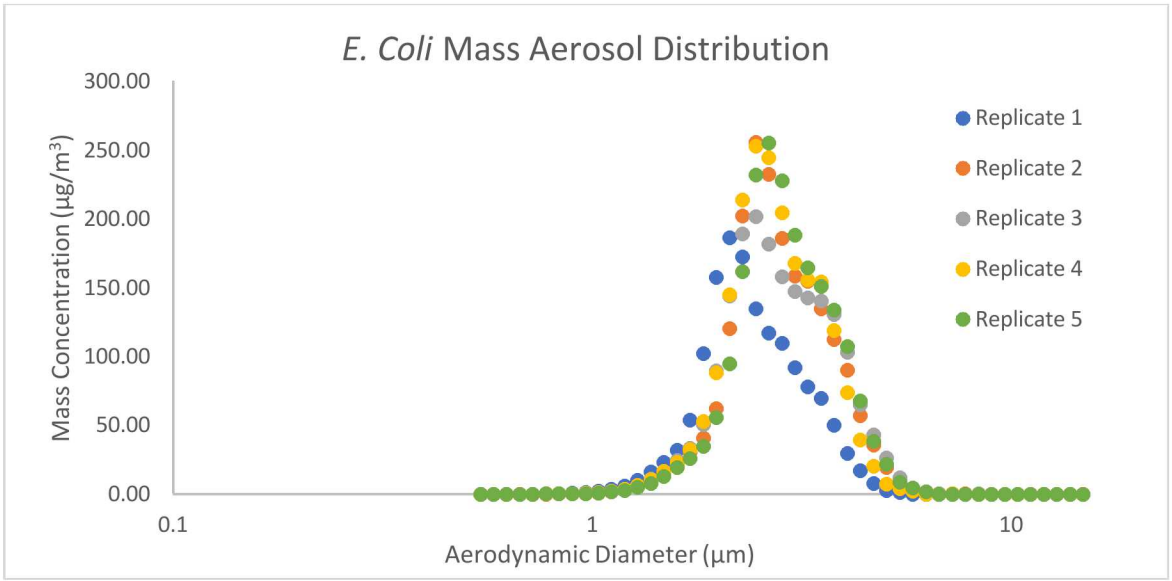

Figure 38. *E. Coli* Mass Aerosol Distribution determined by an APS. Randomized selection of 5 trials as an example of aerosol distribution and variance.

Aerosol stocks of MS-2, similarly stored in spent growth media, were also diluted at ratios of 95% sterile DI water to 5% MS-2. Final aerosol stocks varied from 1.09E+10 to 1.1E+12 PFU/mL. Aerosols were injected using the same injection settings as the *B.t.* and *E. coli*, namely 100 µL/minute into 10 lpm of air (Figure 39).

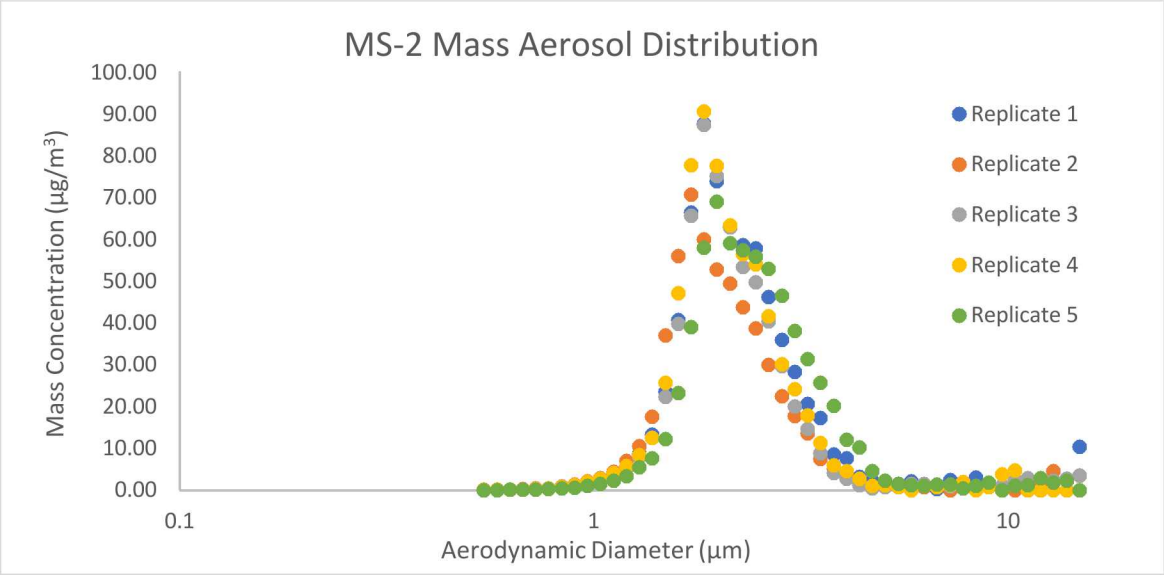

Figure 39. MS-2 Mass Aerosol Distribution determined by an APS. Randomized selection of 5 trials as an example of aerosol distribution and variance.

An overview of the aerosol statistics for all of the organisms is presented here. The 2-3 micron target size was achieved for all organisms, with relatively narrow distributions (Table 3).

Organism	MMAD	GSD
E. coli	2.51	1.314
B. thuringiensis	2.35	1.44
MS2	2.09	1.502

Table 3. Bioaerosol Statistics for each organism throughout testing.

4. SAMPLING METHODOLOGY

4.1 Laboratory Aerosol Collection

During laboratory testing, physical bioaerosol sampling was completed using All-Glass-Impingers (AGI)-30s, with 20 mL of PBS sampling at an airflow rate of 12.5 lpm for 5 minutes, for a total air volume of 60 liters. Time points included an initial sample, taken while aerosolization was on-going, and a final aged sample, between 1 and 4 hours later, depending on the test condition and organism. The sampling objective was two-fold, to age for an extended period of time, while maintaining a quantifiable sample at the end of testing. The initial timepoint was taken as the aerosol concentration reached a steady state, with aerosolization on-going, to collect as pristine of a sample as possible. Aerosol concentrations are calculated from the impingers assuming perfectly

efficient sampling, but always compared to a sample taken using the same methodology at the end of testing, so that the assumption has little practical implications or limitations.

4.2 Laboratory Aerosol Monitoring

4.2.1 Particle Size and Fluorescence

A TSI Inc 3321 Aerodynamic Particle Sizers (APS) and a 3314 Ultraviolet Aerodynamic Particle Sizer (UV-APS) determined the aerodynamic size and concentration of particles in the rotating drum. These time-of-flight sensors sampled at 1 lpm, for four 30 second samples, spaced out across 30-minute increments. The length time intervals were utilized to minimize the amount of disruption to rotational flow in the drum. These instruments operate essentially identically for sizing of particles, with the 3314 utilizing an added fluorescent signal integrated from a 355 nm UV excitation laser, triggered based on the particles time-of-flight. When possible, the 3314 was preferred, but degrading fluorescence signal required replacement, repairs, and recalibrations, and often a 3321 instrument was used instead.

A Single-Particle Fluorescence Spectrometer (SPFS) was developed by the Army Research Laboratory (ARL) for measurement of the changes in the spectral properties of biological aerosols when excited with wavelengths of 263 nm and 351 nm. The SPFS samples biological aerosols at 1 lpm, focusing particles through a jet with a sheath-flow nozzle. A red laser is used to size aerosols based on elastic scattering, and compared to a calibration curve using polystyrene latex (PSL) beads. Aerosol particles greater than approximately 2 μm are used to trigger one of two lasers at 263 nm or 351 nm, to excite naturally occurring fluorophores associated with the bioaerosol. In addition to the fluorescence, the sizing measurement is included in the SPFS for normalization of the fluorescence intensity. The SPFS is used to measure the spectral changes of the aerosols as a function of time, and sampled concurrently with the APS and WIBS (see below) at predominantly 30 minute increments. Unique amongst fluorescent particle detectors, the SPFS is capable of acquiring full emission spectra for individual particles, with a notch filter at the excitation and sizing wavelengths. For the purposes of much of the analysis presented, the SPFS data is binned into 3 key bands: UV263, which integrates UV emission wavelengths excited by the 263 nm laser; VIS263, which integrates the visible emission wavelengths excited by the 263 nm laser; and VIS351, which integrates the visible emission wavelengths excited by the 351 nm laser (ref).

A Droplet Measurement Technologies Inc. Wideband Integrated Bioaerosol Spectrometer (WIBS) 4A was acquired during the second year of testing, as an off-the-shelf fluorescent particle detector. The instrument draws a 0.3 lpm sample, and uses arc-xenon lamp and filter sets to excite particles at 280 and 370 nm, which aligns well with the 355 nm UV APS excitation, and the 263 and 351 nm SPFS excitation wavelengths. At the 280 nm excitation wavelength, the instrument integrates emissions into two bands, 310-400 nm (UV band) and 420-650 nm (visible band). Given the wavelength overlap at 370 nm excitation, fluorescence intensity is integrated into only the latter range for that excitation wavelength .

4.3 Field Sampling Methods

4.3.1 Aerosol Collection

In 2015, aerosol collection was performed using AGI-30s, with 20 mL of PBS sampling at an airflow rate of 12.5 lpm, similar to the laboratory methods and analysis for both viability and PCR was done in the same way. Samples were collected at the beginning and end of each experiment to limit the loss of aerosol due to sampling. In 2016, Midget Impingers, sampling at 1 lpm were used. The smaller flow rate allowed additional samples to be taken throughout each experiment (beginning and end and two midpoint samples), allowing for more points to be used in decay calculations.

4.3.2 Ambient Sow Chamber Methods

Figure 40 shows a 3-D turbulent air model of the ambient Sow chambers designed for this study. In these studies, artificial webs, manufactured from polymethyl methacrylate by Battelle, were spun onto small custom made forks (Figure 40) and placed into the chamber for each study. Aerosol was generated into the each of the two Sow chambers for 15 minutes to provide ample aerosol particles deposited onto the web of each fork, in a deliberately highly mixed turbulent air flow. Previous studies by DSTL indicated that aging on natural spiders webs were identical to aging on the artificial webs produced by Battelle. As mentioned above, the design and configuration allowed matching the two Sow chambers to the same condition as the two CAGE chambers (exposed to ambient conditions, shielded from sunlight, etc.) so that aerosol on the spiderwebs was exposed to exactly the same conditions as the free aerosol in the CAGE chambers, including the control.

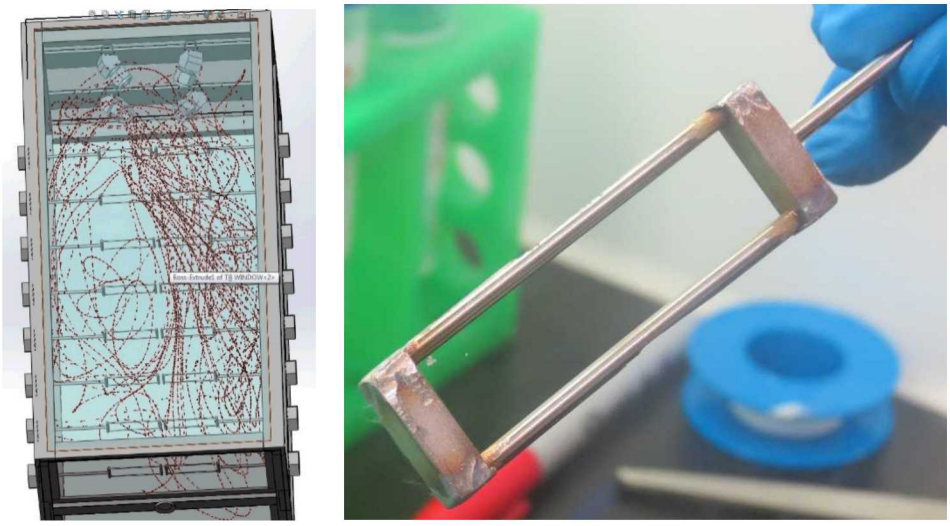

Figure 40. Ambient spiderweb samples from the SOW. (left) 3-D model of Ambient Sow chamber. (right) fork with artificial spiderweb.

5. MICRO AND MOLECULAR BIOLOGY METHODOLOGY

5.1 Culture and Plaque Assays for Laboratory Tests

E. coli and *B.t.* AGI-30 samples were serially diluted in PBS and plated in triplicate on 3M Petrifilm Aerobic Count Plates and LB agar. Since Petrifilm does not allow an observation of colony morphology, LB agar was used in parallel on only the first tests to ensure that aerosol samples contained only the organism of interest, and not previously tested or environmental aerosol contaminants. Petrifilm samples consisted of a 1 mL sample spread using a 3M Petrifilm spreader, whereas LB agar was plated using a Lazy-L spreader of a 100 µL sample. The benefits of Petrifilm are a lower limit of detection (larger sample size), an increased speed of plating, and a lower probability of overlapping colonies or overgrowth. The impinger or stock concentration is calculated from the average plate count, dilution, and the known sample volume.

To quantify MS-2, a plaque assay employing a mobility-reducing top agar is used, to allow counting of individual plaques in a lawn of host bacteria. LB agar plates, and LB agar top agar aliquots are prepared ahead of time. The top agar aliquots contain 7 g/L of agar, compared to the 15 g/L typically utilized in an LB plate, and are partitioned into sample tubes containing 4 mL agar each. Mid-log E. coli A/λ cultures were maintained as described in §4.3 for MS-2 propagation. Top agar is removed to a 50ºC dry bath to re-melt the media, and then combined with 300 µL of *E. coli* and 100 µL of sample, swirled, and decanted onto an LB plate. Plates are incubated overnight, and counted in the morning, with the count, dilution, and sample volume used to calculate the plaque concentration.

5.2 Polymerase Chain Reaction Assays

Bacillus thuringiensis al Hakam samples were quantified using a PCR assay previously described in Ratnesar-Shumate *et. al.* (2012). The probe was modified to use a more conventional FAM dye and TAMRA quencher, and both primer and probe sequences can be seen below (Table 4). DNA isolations were accomplished via a five-minute bead beat using 100 µm glass silica beads (MP Biomedicals 116911100), followed by a rapid gel cleanup using Zeba Microspin 7K MWCO columns, to remove large cellular debris. Thermo-Fischer Scientific Platinum Quantitative PCR Supermix-UDG was chosen to amplify bacterial DNA, with primers and probe added to the Master Mix at concentrations of 300 nM and 250 nM respectively. Of the 25 µL reaction volume, 5 µL was reserved for sample volume. A standard curve was prepared from serially diluted test stock and used to determine equivalent spore concentration. All samples were processed in triplicate on the Bio-Rad CFX Connect, with each plate also containing a sample from the standard curve and no-template controls for quality control.

Bacillus rpoB Target	Forward	5' to 3'	GAACATTAGTAGATCCAGAAAC
	Reverse	5' to 3'	CTTAATAGATTGCAGCTCAAC
	Probe	5' to 3'	**56-FAM**-TCACCTTCTACCACTCCACCAT-**36-TAMSp**

Table 4. Bacillus thuringiensis primers and probes

E. coli K-12 DNA isolations utilized a Qiagen Qiamp DNA Mini Kit from samples frozen immediately after plating to determine the viable concentration of bacteria. Primers and probes are based on an existing published K-12 specific assay (Lu, 2014), as shown in Table 5. Similar to the *B.t.* assay, amplification employed a Thermo-Fischer Scientific Platinum Quantitative PCR Supermix-UDG, with concentrations and reaction conditions taken from the Lu publication. Similar to *B.t.* and MS2, PCR assays were completed in triplicate and referenced to a standard curve developed from the *E. coli* stock. With each plate containing unknowns, representative positive controls from the standard curve, and no-template controls to ensure the assay functioned correctly.

E. coli K-12 Target	Forward	5' to 3'	TAAAGTAACCTTGATCGAAG
	Reverse	5' to 3'	ATTCCTAAAGAAAGTATCTATTC
	Probe	5' to 3'	**56-FAM**-AACGTACCAGCATAAATGATCCT-**36-TAMSp**

Table 5. *E. Coli* Primers and Probes

MS2 bacteriophage RNA concentrations were determined by quantitative reverse transcription polymerase chain reaction (RT-PCR). After completion of a plaque assay, to determine the concentration of effective plaque-forming units, samples were frozen at -20ºC until enough samples were present to begin an RNA extraction. RNA was isolated from MS-2 samples using a Zymo Viral RNA kit. Reverse transcriptase and PCR were accomplished in 25 µL reactions with TaqMan Fast Virus 1-step Master Mix. Detection targeted an assembly protein gene, with reaction conditions and concentrations described by O'Connell, et al. (2006), except that the reverse transcriptase step was completed at 50ºC for five minutes, per the master mix recommendations. Primers and probes also from O'connel et al., are shown in Table 6.

MS2 Assembly Target	Forward	5' to 3'	GTCGCGGTAATTGGCGC
	Reverse	5' to 3'	GGCCACGTGTTTTGATCGA
	Probe	5' to 3'	**56-FAM**-AGGCGCTCCGCTACCTTGCCCT-**36-TAMSp**

Table 6. MS2 Primers and Probe

All samples were processed in triplicate, using a Bio-Rad CFX Connect, with no template controls and representative samples from the MS-2 stock-based standard curve, to ensure consistency of reverse transcriptase and PCR activation. Samples are always compared to an earlier time-point taken on the same day, and processed at the same time, to minimize the effect of storage or PCR conditions on the results.

6. LABORATORY TEST CONDITIONS AND LEVELS

6.1 Overview of Test Levels

As discussed during the methods, two set levels of each variable were chosen to help reduce the scope of environmental conditions, and determine if individual or combinations of variables played a role in aging. Generally, a null or zero concentration, and a 'present', target concentration was chosen. While these levels are discussed in the methods section above, it can be broken into a single table of variable conditions (Table 7).

Condition	Ozone	RH	UV-light	Toluene	α-Pinene
Low (Absent)	0	<30%	Off	0 ppb	0 ppb
High (Present)	80-100 ppb	80%	On	42 ppb	5 ppb

Table 7. Laboratory Test Variable Levels

Laboratory test conditions, and the combinations of variables that were prioritized, were chosen to optimize available testing time and expected interactions of variables based on existing literature. Across two VOCs, UV light conditions, ozone, and two relative humidities, the combination of variables would have resulted in 32 potential test conditions, repeated in triplicate for each organism or simulant. Even with relatively short testing windows with rapid aging, to reach the test conditions, inject, sample, and then purge, only a few tests can be run during a typical day.

Most notably, the VOCs Toluene and α-Pinene were not tested in combination, but instead as individual compounds. Each was a representative compound, anthropogenic and biogenic, respectively, from a more complex real-world environment. Alpha-pinene concentrations are more atmospherically correct, whereas the toluene concentration of 42 ppb is similar to a total concentration of urban aromatics (~30 ppb), to better see the mechanism and significance for more complex environments (Qiu, 2012).

6.2 Testing Combinations

The team intended *E. coli* to have both the most combinations of variables and number of samples, as a test case for the impact of each variable, and combinatory effects only seen with multiple variables present concurrently. While *B.t.* is perhaps the best suited simulant, the relative heartiness of a spore may have made underlying mechanisms and combinatory aging effects more difficult to assess. In comparison, vegetative bacteria such as *E. coli* would be more likely to demonstrate aging effects, enhancing confidence in the results (Table 8). Replicates continued, and expanded into new combinations until the end of testing, ideally a minimum of 3 replicates is completed, but was not possible in all cases.

Table 8. *E. Coli* Variable Combinations

Combinations	UV	RH	Ozone	VOC	N sample size
Low RH (control)		Low			3
High RH		High			3
UV light (Low RH)	X	Low			3
UV light and High RH	X	High			2
Ozone (Low RH)		Low	X		4
Ozone and High RH		High	X		3
A-Pinene and High RH		High		α-Pinene	2
Toluene and High RH		High		Toluene	2
A-Pinene and Ozone		Low	X	α-Pinene	2
Toluene and Ozone		Low	X	Toluene	1
UV and Ozone	X	Low	X		3

UV and Toluene	X	Low		Toluene	3
UV and A-Pinene	X	Low		α-Pinene	4
UV, Ozone, High RH	X	High	X		2
UV, A-Pinene, High RH	X	High		α-Pinene	2
UV, Toluene, High RH	X	High		Toluene	2
A-Pinene, Ozone, High RH		High	X	α-Pinene	2
Toluene, Ozone, High RH		High	X	Toluene	2
Toluene		Low		Toluene	3
A-Pinene		Low		α-Pinene	3
Toluene, UV, low RH, and Ozone	X	Low	X	Toluene	3
A-pinene, UV, low RH, and Ozone	X	Low	X	α-Pinene	3
Toluene, UV, High RH, and Ozone	X	High	X	Toluene	3
A-pinene, UV, High RH and Ozone	X	High	X	α-Pinene	2

Combinations of testing variables for *B.t.* and MS-2 (Tables 9 and 10) were chosen to optimize resources, based on previous experience, and literature indicating that OH radical formation, typically via a combination of water vapor and UV light, is necessary to achieve VOC reactivity and SOA formation (Hurley, 2001).

Table 9. *B. thuringiensis* Testing Combinations

Combinations	UV	RH	Ozone	VOC	N sample size
Low RH (control)		Low			4
High RH		High			3
UV light (Low RH)	X	Low			4
Ozone (Low RH)		Low	X		4
Ozone and High RH		High	X		3
UV and Ozone	X	Low	X		3
UV and Toluene	X	Low		Toluene	3
UV and A-Pinene	X	Low		α-Pinene	3
Toluene		Low		Toluene	3
A-Pinene		Low		α-Pinene	3
Toluene, UV, low RH, and Ozone	X	Low	X	Toluene	3
A-pinene, UV, low RH, and Ozone	X	Low	X	α-Pinene	3
Toluene, UV, High RH, and Ozone	X	High	X	Toluene	3
A-pinene, UV, High RH and Ozone	X	High	X	α-Pinene	3

Table 10. MS-2 Testing Combinations

Combinations	UV	RH	Ozone	VOC	N sample size
Low RH (control)		Low			3
High RH		High			3
UV light (Low RH)	X	Low			4
Ozone (Low RH)		Low	X		3

Ozone and High RH		High	X		3
UV and Toluene	X	Low		Toluene	3
UV and A-Pinene	X	Low		α-Pinene	3
Toluene		Low		Toluene	3
A-Pinene		Low		α-Pinene	4
Toluene, UV, low RH, and Ozone	X	Low	X	Toluene	3
A-pinene, UV, low RH, and Ozone	X	Low	X	α-Pinene	3
Toluene, UV, High RH, and Ozone	X	High	X	Toluene	4
A-pinene, UV, High RH and Ozone	X	High	X	α-Pinene	3

7. RESULTS

7.1 Laboratory Results

Laboratory data was normalized to particle number concentrations in the drum, to account for varying levels of particle loss depending on the test condition, and the sample time. Additional techniques to account for varying amounts of particle loss were considered, including co-aerosolization of a fluorescent tracer, and the use of mass concentration of particles. Each of these techniques have shortfalls. For the fluorescent tracer, any fluorophore co-aerosolized would likely age in parallel with the bioaerosol, and at an unknown rate, dependent on aging conditions. Therefore, reported fluorophore concentrations would not track with the number of particles. Additionally, the absorbance and emissions bands would interfere with the study of fluorescent decay using the SPFS and WIBS.

Utilizing the mass concentration of aerosols yields similar results to the APS number aerosol concentration, but is less reliable because of changes in the relative humidity and increasing particle diameter during high relative humidity tests. The increasing particle diameter is indicative of water-uptake and increasing mass, and introduces additional noise into the normalization.

Therefore, to calculate log decay rates normalized to number concentration, the following equation is used:

Equation 6. Log Decay Calculation

$$\frac{\log_{10}\left(\frac{C_{0AGI}}{n_0}\right) - \log_{10}\left(\frac{C_{1AGI}}{n_1}\right)}{t_1} = \log \text{decay per hour}$$

, where:

C = Aerosol Concentration – Determined by PCR or Plating
n = Number Aerosol Concentration – Determined by APS or UVAPS
t = Time Point of Second Sample
0,1 = Initial and Second Aerosol Time Point

This equation can be adjusted to give an exponential decay constant, of the form:

Equation 7. Exponential Decay Calculation

$$C(t) = C_0 e^{-rt}$$

, where:

C = Aerosol Concentration as a Function of Any Time, t
C_0 = Initial Aerosol Concentration at Time 0
t = Time Aerosol Has Been Aging (Seconds, s)
r = Rate of Decay (s^{-1})

A few replicates were not viable, even at time points of less than 2 hours. In these cases, the minimum detectable aerosol concentration is assumed, but is very likely lower, and contributes to higher standard deviations between replicates. Future tests attempted to shorten the sampling time point to capture culturable material. For the *E. Coli* and *B.t.* that minimum detectable concentration corresponds to a concentration of 0.1056 CFU/L of air. This calculation derives from the concentration associated with counting a single colony from triplicate, one milliliter samples plated on Petrifilm (0.333 CFU/mL of collected sample). Back calculating further, an AGI sample volume at 19 mL after collection, and a total of 60 L of air sampled from the drum over a 5-minute sample, the lowest detectable limit is 0.1056 CFU/L of air.

A similar calculation for MS-2 leads to a higher limit of detection, since only 0.1 ml of a sample is assayed (albeit in triplicate). A single detectable plaque corresponds to 3.33 PFU/mL of collected sample, or 1.05 PFU/L of air for an AGI. All but one MS-2 sample had countable plaques, even after significant aging. The high initial titer of MS-2, compared to the bacterial samples, increases the dynamic range, even at a higher limit of detection. The number of replicates and experimental conditions requires pooling of samples to determine statistical significance. This is done for both scientific and statistical reasons. For instance, VOC reactions typically require radical formation, and are less likely to cause an effect by themselves, then in the presence of a OH or nitrate radical.

7.1.1 *E. coli*

E. coli best exhibits the difference between aging conditions, because of its susceptibility to aging compared to a spore-forming species, and was chosen for an expanded number of trials (Figure 41). Per the discussion on pooling variables above, one-sided T-tests were calculated assuming equal variance. While UV light aging is anecdotally occurring, when pooling all variables off (essentially the control condition) with the condition where only alpha-pinene is applied (to increase the sample size and statistical significance, since this variable did not significantly increase aging), there is not enough additional aging under UV lights to be significant above an 80% confidence interval, with a p-value of 0.172. This calculation includes pooling both UV light alone and UV light with alpha-pinene (see Appendix A for T-Tables). This may simply indicate that the UV aging occurring in here is less effective than other aging variables either as a result of the organism or the power of the UV lights. However, there is stronger confidence in the effects of aging in both RH and most ozone aging conditions, which agrees with previous studies (Santarpia, 2012). Specifically, the p-value for the same control conditions when compared to High

RH alone pooled with high RH and alpha-pinene is 0.055, significantly above 90% confidence. Nearly as significant, the pooled combination of ozone alone, with ozone and alpha-pinene leads to a p-value of 0.114, indicating significant ozone aging. Most uniquely to this study, the toluene alone yielded a P-value of 0.072 compared to the controls, likely because of the relatively high concentration, and therefore demonstrated additional aging compared to the no variable and alpha-pinene conditions.

Most importantly for this report, while toluene and alpha-pinene alone demonstrate relatively limited enhanced aging (although statistically significant for toluene), the presence of toluene with UV light demonstrates a significant amount of additional aging, even when pooling a significant number of variables that may underestimate other combinatory effects. First, for comparison, all samples with UV light without VOCs, including UV light with low humidity, UV light and high humidity, UV light and ozone, and UV light with ozone and high RH were pooled. These same conditions with toluene, specifically, UV light and toluene, UV light high RH and toluene, UV light toluene and ozone, and UV light high humidity ozone and toluene yielded a p-value of $\ll 0.01$ compared to the previous group. Although never studied on biological aerosols in such a manner before, the lifetime and fate of these VOCs as pollutants is well understood, and is dependent on OH radicals, likely provided in this case by UV activation of water vapor even in relatively low RH cases. This can be seen visually by looking at the combinations of UV light and toluene in Figure 41.

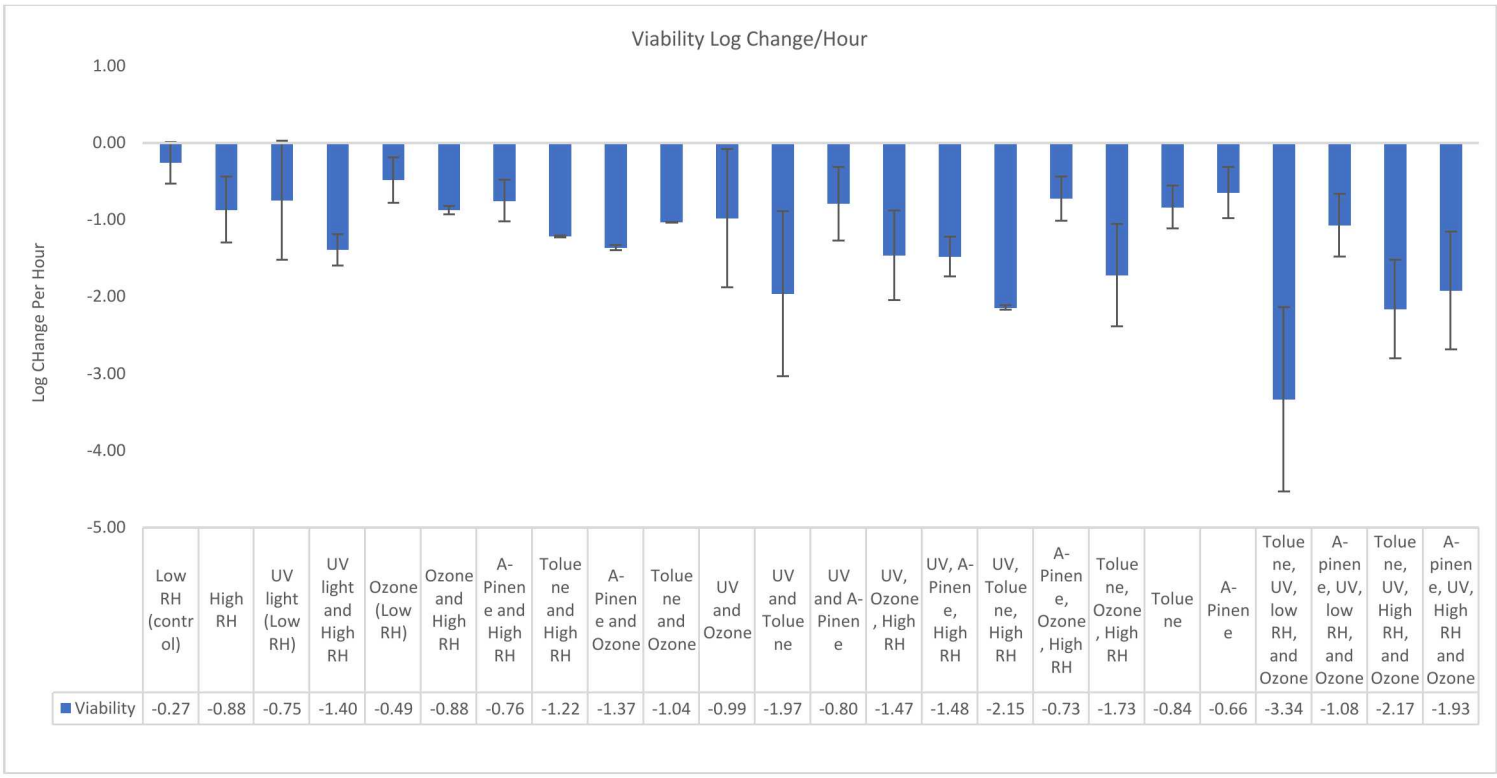

Figure 41. *E. coli* Laboratory Viability Decay Comparison

Changes in PCR detection for *E. coli* were more subtle, but mostly in line with changes in viability (Figure 42) except in a few cases. For instance, high humidity demonstrated no significantly

increased aging, alone or in combination with VOCs. However, UV light and ozone did cause relatively accelerated aging when compared to other conditions. The lack of change in PCR concentration as a function of humidity indicates that the changes in viability are likely occurring on the surface, or as a function of pH in the particle, instead of compromising the genomic DNA.

Throughout testing, the PCR results are relatively noisy compared to changes in viability. Since the DNA or RNA is relatively protected, it is changing slower than the viability, which relies on reactive surface proteins and cell membranes remaining intact and functional. These small changes become even noisier when normalized to particle concentrations to account for variations in physical losses, especially when compared to the relatively accelerated changes in viability.

Similar to the viability data, toluene only has an effect when combined with UV light, which is accelerated compared to UV light alone (P=0.075). This is based on a pooling of the same sample types as included above (with and without toluene), namely: UV light with low humidity, UV light and high humidity, UV light and ozone, and UV light with ozone and high RH. As with viability the effect of alpha-pinene alone and in combination with UV light is non-existent, yielding a p-value of 0.476.

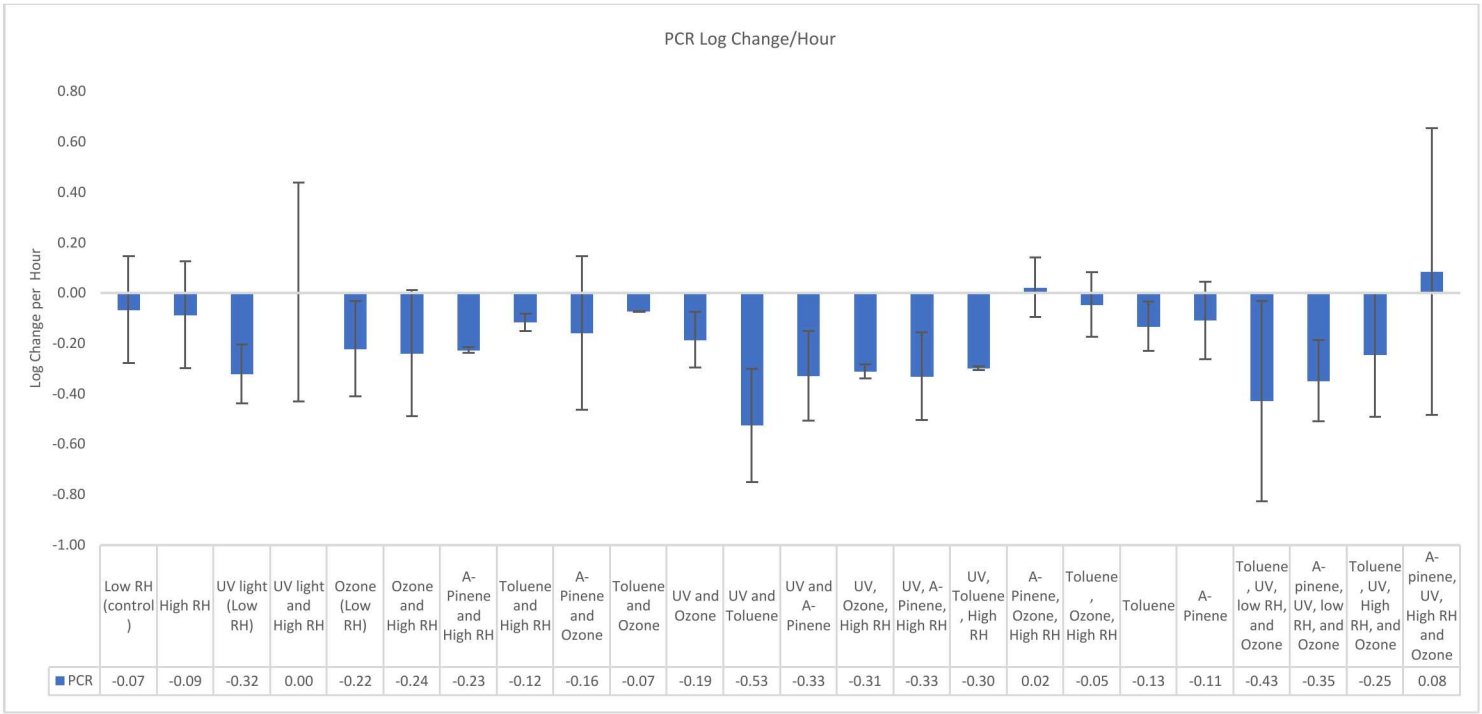

Figure 42. *E. coli* Laboratory PCR Decay Comparison

Conversion of log decay rates to exponential decay rates using Equation 6 (Table 11) demonstrates how varied aging conditions lead to order of magnitude differences in decay rate.

Table 11. *E. coli* Laboratory Exponential Decay Rates

Combinations	*E. coli* Viability Decay Rate

Low RH (control)	-1.71E-04
High RH	-5.60E-04
UV light (Low RH)	-4.81E-04
UV light and High RH	-8.95E-04
Ozone (Low RH)	-3.15E-04
Ozone and High RH	-5.64E-04
A-Pinene and High RH	-4.86E-04
Toluene and High RH	-7.82E-04
A-Pinene and Ozone	-8.76E-04
Toluene and Ozone	-6.64E-04
UV and Ozone	-6.32E-04
UV and Toluene	-1.26E-03
UV and A-Pinene	-5.11E-04
UV, Ozone, High RH	-9.39E-04
UV, A-Pinene, High RH	-9.49E-04
UV, Toluene, High RH	-1.37E-03
A-Pinene, Ozone, High RH	-4.69E-04
Toluene, Ozone, High RH	-1.11E-03
Toluene	-5.39E-04
A-Pinene	-4.20E-04
Toluene, UV, low RH, and Ozone	-2.14E-03
A-pinene, UV, low RH, and Ozone	-6.91E-04
Toluene, UV, High RH, and Ozone	-1.39E-03
A-pinene, UV, High RH and Ozone	-1.23E-03

7.1.2 *B. thuringiensis*

The most noticeable differences between *B. thuringiensis* spores and the vegetative *E. coli* is the change in y-axis, with aging occurring on much slower timelines and in smaller magnitude on average. High humidity, ozone, and the combination of high RH and ozone fail to see statistically significant amounts of additional aging. Instead UV light dominates aging, agreeing with previous data. In this case, the UV light conditions are all similar, regardless of other variables present, creating a strong statistical degree of aging ($P \ll .01$), when low and high RH samples (which showed no difference) are pooled against all UV light aged samples.

In a first study of its kind, the VOCs do present slightly higher degradation rates than the control conditions, and this case is strengthened by the low variance on the low and high RH alone conditions, and is also statistically measurable above the effects of UV light alone. In particular, the effects of alpha-pinene vs low RH conditions, alpha-pinene and UV light, vs UV light alone, and alpha-pinene UV light and ozone compared to just UV light and ozone have p-values of 0.144, 0.088, and 0.005, respectively. Visually, it is clear from the graph (Figure 43) that the effects of UV light dominate the aging in a laboratory setting, so that the combinatory or enhanced effect of

a VOC is limited, but still present. However that effect must be even more noticeable in complex real-world VOC conditions, compared to simplified laboratory settings. The strong p-values in the presence of UV light indicate that activation of the monoterpenes with OH radicals remains important to rapid aging.

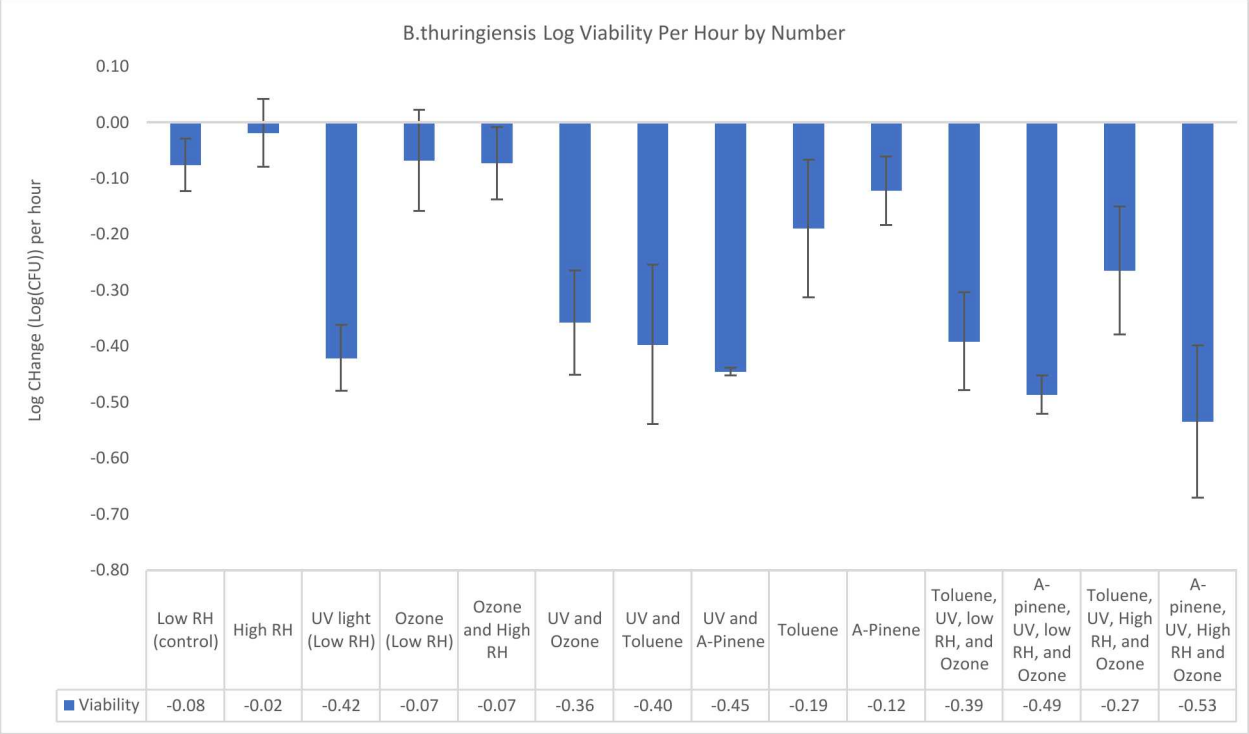

Figure 43. *B.t.* Laboratory Viability Decay Comparison

Similar to the PCR data for *E. coli,* PCR decay in *B. thuringiensis* occurs changes slowly, and at rates that are sometimes faster, and sometimes slower than changes in viability, depending on the aging condition (Figure 44) The biggest variation from the changes in viability is the combinatory effect of Ozone and RH, also known as RH-mediated ozonolysis. It is hypothesized that this decay, the strongest measured change in PCR signature over time, is a function of degradation of extra-spore DNA, which is present even despite pre-aerosolization washes, and more susceptible to aging (Almeida, 2008).

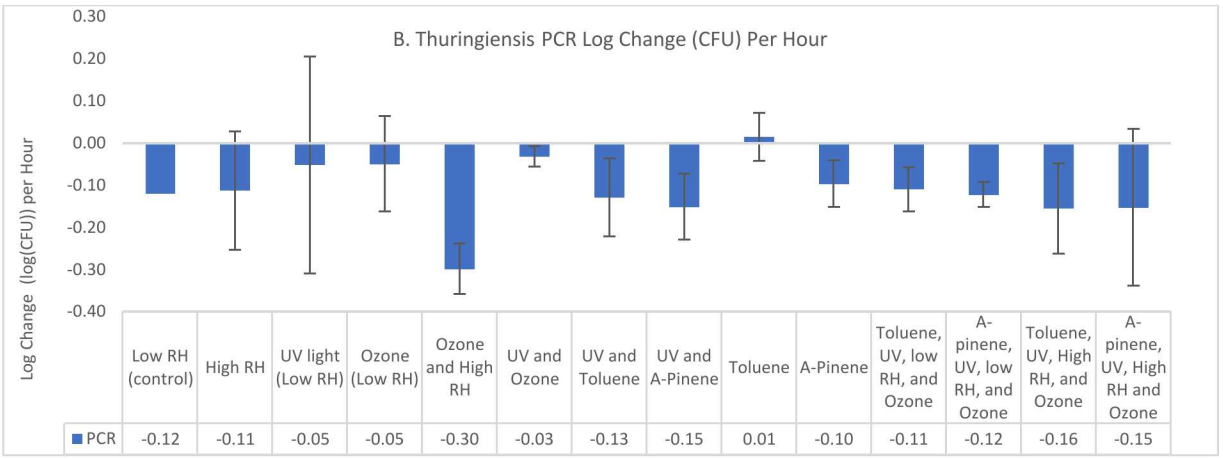

Figure 44. *B.t.* Laboratory PCR Decay Comparison

Converting log-loss rates to the exponential decay rates per equation 6 allows for use in atmospheric modeling and fate prediction (Table 12).

Table 12. *B.t.* Laboratory Exponential Decay Rates

Combinations	*B.t.* Viability Decay Rate
Low RH (control)	-4.90E-05
High RH	-1.24E-05
UV light (Low RH)	-2.70E-04
Ozone (Low RH)	-4.40E-05
Ozone and High RH	-4.72E-05
UV and Ozone	-2.29E-04
UV and Toluene	-2.54E-04
UV and A-Pinene	-2.85E-04
Toluene	-1.22E-04
A-Pinene	-7.87E-05
Toluene, UV, low RH, and Ozone	-2.51E-04
A-pinene, UV, low RH, and Ozone	-3.11E-04
Toluene, UV, High RH, and Ozone	-1.70E-04
A-pinene, UV, High RH and Ozone	-3.42E-04

7.1.3 MS2

In addition to dominance of UV light on MS-2 infectivity ($p \ll 0.001$), MS-2 demonstrates many classical examples of combinatory effects compared to the B.t., and is less noisy because of the higher dynamic range of starting with a concentrated stock (Figure 45). The next most noticeable effect is high humidity with a p value of 0.004. After that, there is a significant combinatory effect of ozone and humidity ($p=0.016$), with no effect of ozone alone ($p=.275$). There is no statistical effect of a VOC on these viral samples infectivity, although the additive effect of UV light with

the combinatory effect of RH and ozone is present in the High RH, UV light, and Ozone with VOC samples.

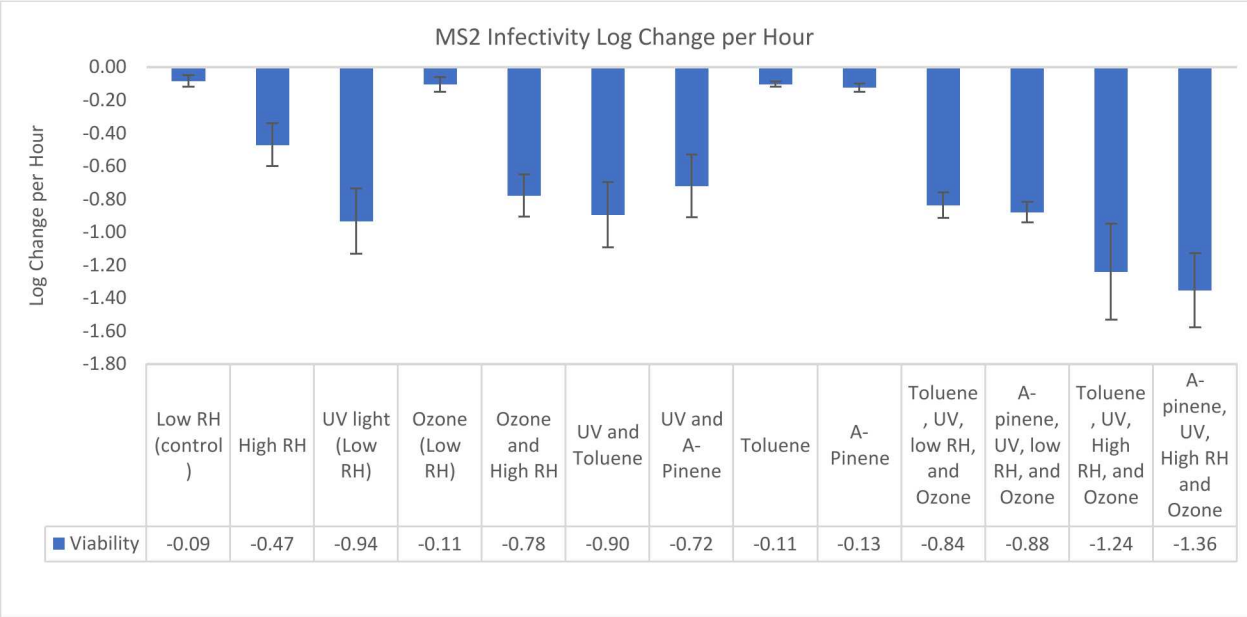

Figure 45. MS-2 Laboratory Viability Decay Comparison

The decay in PCR detection present in the RT-PCR assay for MS-2 shows much smaller amounts of degradation over time, indicating that the RNA is relatively protected from the atmospheric aging conditions (Figure 46). It is important to note that the protection of a agglomerate could be a function of residual media present and shielding, and may not be true for all particle sizes or levels of purity.

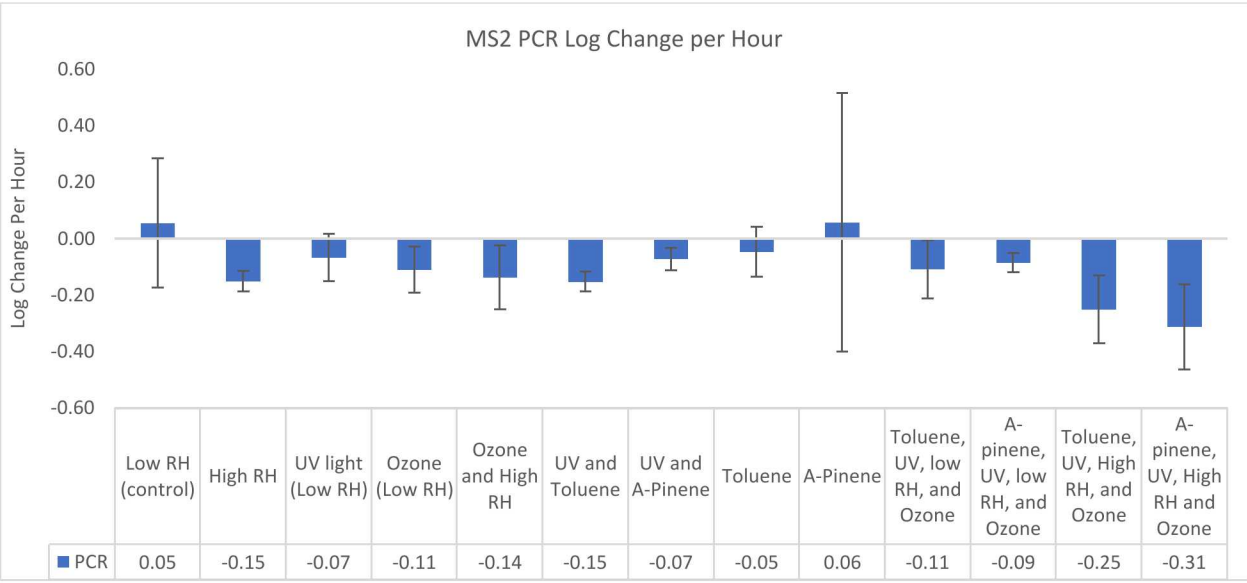

Figure 46. MS-2 Laboratory PCR Decay Comparison

Similar to the other agents, changes in MS-2 infectivity in exponential decay form show a log plus difference in decay depending on the variables present in the experiment (Table 13).

Table 13. MS-2 Laboratory Exponential Decay Rates

Combinations	MS-2 Infectivity Decay Rate
Low RH (control)	-5.46E-05
High RH	-3.03E-04
UV light (Low RH)	-6.00E-04
Ozone (Low RH)	-6.83E-05
Ozone and High RH	-5.40E-04
UV and Toluene	-5.75E-04
UV and A-Pinene	-4.63E-04
Toluene	-6.89E-05
A-Pinene	-8.15E-05
Toluene, UV, low RH, and Ozone	-5.37E-04
A-pinene, UV, low RH, and Ozone	-5.65E-04
Toluene, UV, High RH, and Ozone	-7.96E-04
A-pinene, UV, High RH and Ozone	-8.67E-04

7.2 Field Test Results

During the summer months of 2015 and 2016, several weeks of field experiments were performed at a site in the W.G. Jones State Forest near Conroe, Tx (described above). During 2015, these experiments utilized both the CAGE system and the Ambient Sow chambers to expose biological aerosol particles to ambient environmental conditions. In 2016, only the CAGE system was used. The 2015 experiments consisted exclusively of daytime experiments, while in 2016 a mix of daytime and nighttime experiments were performed, to further separate chemical aging from UV degradation. Each system consists of 2 chambers, so that the conditions in each chamber could be different during the experiments. For instance, in some cases, one chamber would be exposed to sunlight and all ambient gas-phase species, while another chamber could be kept isolated from solar radiation with its intake filtered to remove ambient species. This would potentially allow bioaerosols generated at the same time to be exposed to different conditions during the same time period to investigate the role of sunlight and chemical aging separately. In practice, this was only achievable for a limited number of cases.

The list of experiments performed in each year that was used in this analysis is described in Table 14. As indicated, experiments were performed over a period of several weeks in during the summer

and early fall in both years. During 2015, experiments focused exclusively on daytime aging, while in 2016, experiments were split between daytime and nighttime exposures.

Date	Agent	Drum A	Drum B	Start Time
7/8/2015	Bt	Ambient	Cover, Carbon	1009
7/9/2015	Bt	Ambient	Cover, Carbon	1015
7/13/2015	Bt	Ambient	Cover, Carbon	1001
7/14/2015	Bt	Ambient	Carbon only	1015
7/15/2015	Bt	Ambient	Carbon only	1017
7/16/2015	Bt	Ambient	Carbon only	1026
7/20/2015	Bt	Ambient	Ambient	1011
7/21/2015	Bt	Cover only	Cover, Carbon	1023
7/22/2015	Bt	Cover only	Cover, Carbon	1011
7/23/2015	Bt	Cover only	Cover, Carbon	1042
8/29/2016	Bt	Ambient	Cover	2036
8/30/2016	Bt	Ambient	Cover	2005
8/31/2016	Bt	Ambient	Cover	1459
8/31/2016	Bt	Ambient	Cover	2000
9/1/2016	Bt	Ambient	Cover	1106
9/12/2016	Bt	Ambient	Cover, Carbon	2048
9/13/2016	Bt	Ambient	Cover, Carbon	1218
9/13/2016	Bt	Ambient	Cover, Carbon	1955
9/14/2016	Bt	Carbon only	Ambient	1235
9/14/2016	Bt	Carbon only	Ambient	1235
9/15/2016	Bt	Carbon only	Partial Cover	1157
9/21/2016	Bt	Partial cover	Cover	1940
9/22/2016	Bt	Partial cover	Cover	750

Table 14. List of Field Experiments and Conditions 2015 and 2016, Conroe, TX.

During both years, a Proton-Transfer Reaction Mass Spectrometer (PTRMS) was used to measure the concentration of select gas phase organic species in the local atmosphere at the site. This system was owned and operated by the University of Houston (UH) and not directly a part of these experiments, but they have made the data available for these analysis. The University also measured a selection of inorganic species that was also shared for these analysis. As mentioned previously, the growth rate (GR) of a submicron (0.3 um) ammonium sulfate particle was tracked throughout each experiment. This particle mode served as a marker for secondary aerosol formation processes that would be occurring on all particles in the chamber, including the biological particles. Table 15 shows the average concentration of organic and inorganic species measured during each experiment in 2015, as well as total solar radiation and calculated aerosol growth rates, and Table 16 shows the average concentration of these species during 2016, additional environmental data and calculated aerosol growth rates. The availability of data from each year is somewhat different, due to upgrades in instrument operation and the needs of the project supporting UH.

	O3 ppbv	SO2 ppbv	Noy ppb	NO2 ppbv	NO ppbv	CO ppbv	methanol ppbv	acetaldehyde ppbv	acetone ppbv	isoprene ppbv	methyl vinyl ketone ppbv	methyl ethyl ketone ppbv	benzene ppbv	toluene ppbv	m-xylene ppbv	1,3,4-trimethylbenzene ppbv	camphene ppbv	solar avg W/m2	growth nm/hr
8-Jul	24.5791	2.12966	3.71784	2.2402	0.66653	100.47	7.95414	0.6256	1.55559	3.91019	1.19914	0.38609	-0.0716	0.00705	-0.0782	-0.0624	0.12082	701.204	8.10
9-Jul	18.8832	0.38874	3.47174	2.24548	0.79213	104.706	9.23065	1.37825	2.55318	3.87299	1.32943	0.61674	0.11129	0.14432	0.08275	0.06514	0.3	671.734	6.33333
13-Jul	32.2377	-0.3605	2.3261	1.35064	0.32595	89.3127	9.22924	0.6758	1.5069	2.69809	1.1864	0.32573	-0.1193	0.05416	-0.1212	-0.0484	0.06132	814.376	8.40
14-Jul	35.9353	-0.4007	2.38842	1.43676	0.28275	85.1521	9.33699	0.68434	1.58408	2.61162	1.17107	0.32616	-0.069	0.0434	-0.0826	-0.0121	0.12487	692.78	3.386
15-Jul	46.9835	-0.0044	2.68779	1.539	0.29027	102.13	8.3705	0.77838	1.93849	2.8354	1.09901	0.39932	-0.1035	0.07337	-0.0299	0.00166	0.08517	737.145	6.80565
16-Jul	48.209	0.52997	2.86597	1.75137	0.28104	105.769	8.45514	0.87611	2.15275	3.241	1.1413	0.4899	-0.0334	0.12251	-0.0627	0.02113	0.16073	736.224	3.78903
20-Jul	36.4681	-0.0584	2.62159	1.51821	0.32929	102.123	9.59319	0.84505	1.98938	2.96952	1.39686	0.51193	0.08246	0.21237	-0.005	0.09781	0.18077	687.46	5.41967
21-Jul	31.2511	-0.0811	2.79049	1.94137	0.41675	95.2395	9.3617	0.83137	1.84912	3.2608	1.26609	0.43523	0.00655	0.147	-0.0251	0.10213	0.29087	677.918	1.02953
22-Jul	33.1579	-0.0153	2.58699	1.58394	0.36248	99.0403	8.00311	0.82918	1.63218	3.58448	1.24604	0.50618	0.08551	0.22479	0.09979	0.21423	0.35323	672.292	N/C
23-Jul	36.8559	-0.0065	4.29675	2.80056	1.70563	110.826	11.5671	1.18633	2.37786	3.91984	1.53909	0.76057	0.15834	0.26222	0.12986	0.20416	0.39803	719.853	0.17694

Table 15. 2015 Field test list of monitored species, variables, and averages

Date	Start Time	O3 ppbv	CO ppbv	NO ppbv	NO2 ppbv	NOy ppbv	SO2 ppbv	Propyne ppbv	Acetonitrile ppbv	Propene ppbv	Acetaldehyde ppbv	formic acid ppbv	1-butene ppbv	Acetone ppbv	Dimethyl Sulfide ppbv	Isoprene ppbv	Methyl Vinyl Ketone ppbv	Methyl Ethyl Ketone ppbv	Hydroxyacetone ppbv	Benzene ppbv	3-Methylfuran ppbv	3-Pentanone ppbv	Toluene ppbv	3-Hexanone ppbv	M-Xylene ppbv	1, 3, 5-Trimethylbenzene ppbv	1, 2, 4, 5-Tetramethylbenzene ppbv	Camphene ppbv	Temperature F	Relative Humidity	Pressure mb	Wind Speed ms	Wind Direction deg	Growth Rate nm/hr
8/29/2016	2036	13.41045	126.0425	0.116958	0.116958	2.10362	0.145537	0.384374	0.16903	2.163535	1.389535	37.37561	1.132123	1.877335	0.024607	0.587521	0.12588	0.295827	0.437609	0.072199	-0.12891	0.086496	0	0	0	-0.1221	0	0.021479	76.0405	91.08635	1006.512	0.046711	114.2599	0.59
8/30/2016	2005	11.75574	231.8507	0.56298	7.477001	7.841241	0.177251	3.803343	0.344954	11.67759	5.487372	73.49102	2.272857	16.63076	0.306222	1.80345	0.479066	1.321511	0.670833	0.243343	-0.00173	0.400962	0.39558	0	0.28821	0	0	2.280233	81.47324	82.70222	1004.905	#DIV/0!	215.0609	1.79
8/31/2016	1459	N/A	N/A	N/A	N/A	N/A	N/A	1.293257	0.223614	6.630868	3.397226	62.49658	1.672873	5.114594	0.016074	3.383237	0.900535	1.23377	0.302332	0.011969	-0.07566	0.46331	0.132024	-0.12808	0.140001	-0.23389	-0.36029	-0.65178	89.7022	63.37668	1003.261	0.206637	127.5799	6.58
8/31/2016	2000	3.4895	244.944	0.355611	3.44262	N/A	N/A	0.938857	0.199695	5.023244	2.447884	59.42464	2.283135	4.325464	0.078035	1.752375	0.329174	0.826154	0.230603	0.282285	0.106811	0.305812	0.399557	0	0.273877	0	0	2.420562	79.12832	92.21407	1003.879	#DIV/0!	252.2852	0.03
9/1/2016	1106	43.45101	190.1348	0.176985	0.627044	1.567793	0.223736	0.893519	0.270294	6.832607	3.768715	66.95652	1.496659	5.796233	-0.02277	2.028836	0.690435	1.066541	0.415893	0.0263	0.018645	0.308906	0.061427	-0.08784	0.226344	-0.10228	-0.12629	-0.3258	90.77476	57.75204	1005.22	0.14394	171.9102	8.43
9/12/2016	1015	16.24373	185.1598	0.113185	5.910492	6.577099	N/A	N/A	N/A	N/A	N/A	N/A	N/A	N/A	N/A	N/A	N/A	N/A	N/A	N/A	N/A	N/A	N/A	N/A	N/A	N/A	N/A	N/A	79.57515	82.31755	1005.533	0.034957	114.252	1.62
9/13/2016	1218	37.90405	118.4158	0.285554	1.174133	2.720396	N/A	0.925376	0.237313	4.302096	2.172364	36.70176	1.436534	3.086767	0.200314	1.948841	1.089006	0.802865	0.583513	0.193932	0.125395	0.347371	0.274927	0.128485	0.273584	0.148527	0.010527	0.375737	88.89715	61.44411	1006.572	0.08177	158.5086	1.76
9/13 pm	1955	21.74396	164.0816	0.100418	4.328925	4.973766	N/A	0.594764	0.20409	2.971738	1.616189	25.3484	1.306081	2.647509	0.162755	0.721514	0.344981	0.514105	0.363721	0.231294	0.094267	0.181766	0.271839	0.053359	0.225744	0.099238	0	0.80012	79.44758	81.77008	1006.779	0.031422	118.6376	1.94
9/14/2016	1235	29.75613	91.13798	0.266576	0.678379	1.887444	N/A	1.006216	0.214874	4.695932	2.207439	41.94296	1.243687	3.135909	0.113432	2.426161	1.009289	0.814348	0.625405	0.050675	0.03174	0.324583	0.164723	0.029499	0.141451	0.007613	-0.13811	-0.09195	90.4012	53.05831	1008.369	0.126118	157.1037	7.18
9/15/2016	1157	35.17926	103.7434	0.308518	0.845704	1.681604	N/A	0.819326	0.211285	5.025085	2.264499	57.43514	1.529112	3.476212	0.101461	2.31301	1.033785	0.920222	0.670021	0.067837	0.04515	0.336824	0.119573	0.031746	0.067648	0.006546	-0.11222	-0.06852	90.73287	51.94845	1007.198	0.101555	158.4543	2.80
9/21/2016	1940	16.09629	272.42	0.717556	11.97272	14.50538	N/A	1.624957	0.301593	6.327524	2.649574	68.08649	3.074707	4.955657	0.350412	2.927236	1.448785	1.146566	0.987287	0.380484	0.299066	0.585595	0.740887	0.199058	0.390169	0.269573	0.309832	2.645567	79.16332	73.82921	1006.401	#DIV/0!	210.7826	3.07
9/22/2016	750	14.09068	241.6792	1.509888	7.661452	11.36168	N/A	1.253884	0.317408	3.541853	1.456128	40.91769	1.815131	2.981035	0.475822	1.935944	0.833907	0.76688	1.213647	0.699261	0.560347	0.538494	0.831004	0.448975	0.589566	0.671122	0.813126	2.674026	76.21132	88.73818	1007.171	0.069883	121.8427	0.47

Table 16. 2016 Field test list of monitored species, variables, and averages

7.2.1 Drum and Web Outdoor Comparison

In 2015, CAGE and Environmental Sow chambers were used side by side to compare the two methods of aging aerosol particles. The value of this comparison is significant, because it would provide a comparison point for many years of research that were done using Sow chambers at DSTL to both the rotating drum chambers used in this study and by other groups. In Sow chambers, spiderwebs (both natural and artificial) are used to capture aerosol particles and the spiderwebs are gently recovered by spinning a sterile loop inside the frame, and then cutting off tip of loop into 10 mL PBS (after exposure). This method ensures particles that may have entrained on the frame itself are not a significant contribution to aging results, and that only those particles suspended on the webs are assayed. Because the webs are so thin (~2 µm in diameter), it is hypothesized that the difference in exposure of the captured particles is negligible compared to that of "free" aerosol particles in the chamber, and that they act as virtual aerosols.

The results of experiments done in 2015 indicate that data taken from particles captured on spiderwebs can be treated essentially the same as data from experiments using chambers with free aerosol. Figure 47 shows the viability decay rates for the CAGES chambers and the Ambient Sow chambers over 3 days of experiments. In these experiments, one drum (ambient) was exposed to unfiltered environmental air and sunlight, while the second drum (control) was protected from sunlight and the air was carbon filtered to remove any ambient species. Figure 48 shows 3 days of experiments where the ambient drum was exposed to unfiltered environmental air and sunlight and the control drum was also exposed to sunlight, but air was carbon filtered. Comparison of figures 1 and 2 clearly indicate that exposure to sunlight is the dominant factor causing decay in the viability of B.t.in these experiments. It also clearly indicates that the viability decay measured through the 2 techniques is almost identical. The calculated difference in the viable decay rates measured between the two techniques was only 13.7% +/- 7.5%.

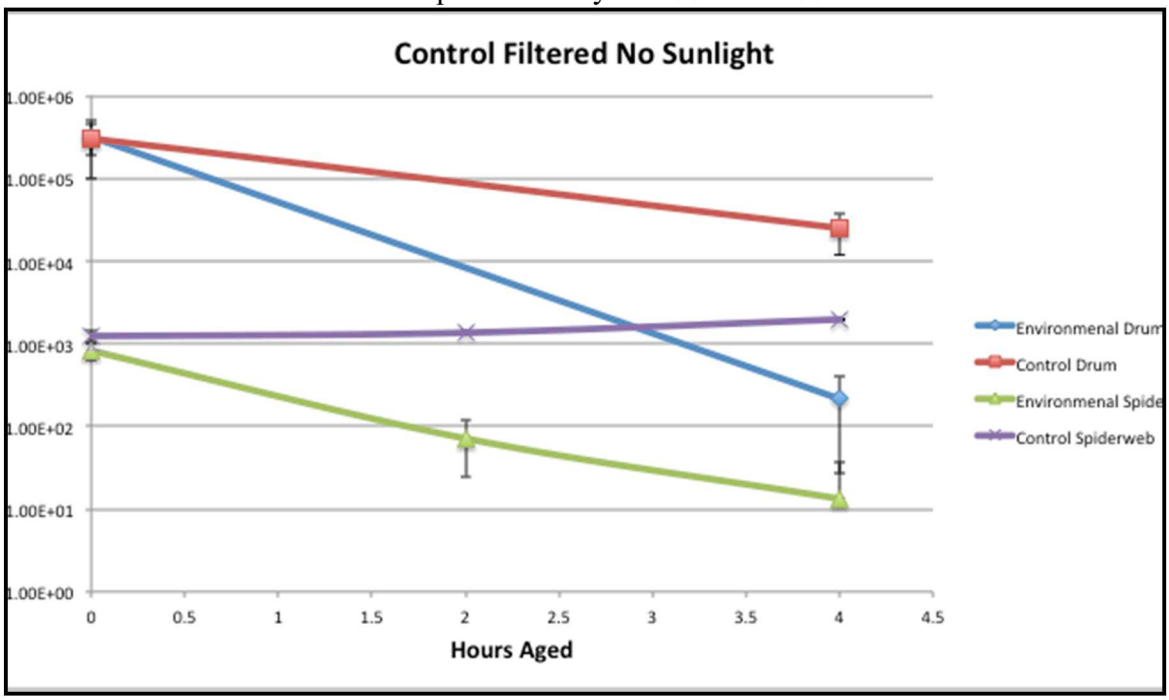

Figure 47. Three days, or replicates, of comparison between drums and webs, with no sunlight and carbon filtered air on the control chambers

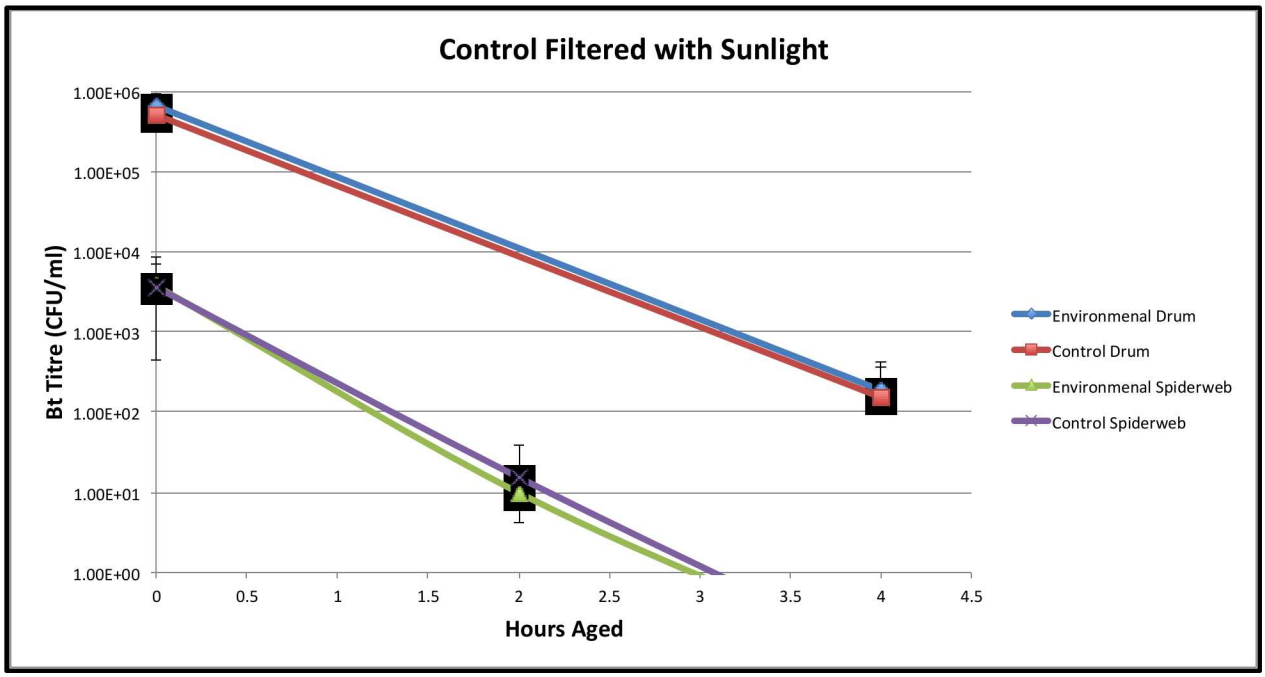

Figure 48. Three days, or replicates, of comparison between drums and webs, with sunlight in the control chambers, but utilizing carbon filtered air

7.2.2 Decay Rates for 2015

Despite attempts to use multiple simulants during both 2015 and 2016 studies, only Bacillus thuringiensis provided consistent data that could be used to compute decay rates. Several factors likely contributed to the failure of these simulants to provide good data, but key among them is fragility of both E. coli and MS2 bacteriophage as compared to *B.t.* spores. In many cases, for both E. coli and MS2, no surviving organisms were found in the samples taken immediately after dissemination, despite identical growth and aerosolization techniques with the laboratory tests. Discussion of possible process improvements that might recover additional viable organisms will be discussed in the final section, and for the remainder of the field results the data will focus on the decay of Bacillus thuringiensis.

In 2015, for the purposes of calculating decay rates, experiments were binned into two categories. The first was a full environmental exposure, of which there are seven experiments. The second is one where the environmental drum was protected from sunlight, but exposed to the ambient chemical species, of which there are three experiments. During six of these experiments, the control drum was protected from sunlight and the air was carbon filtered to remove ambient gas phase species. These control experiments should represent the average loss due solely to physical loss mechanisms and sampling, and exclude the aging mechanisms being studied, and was determined to be 0.22 logs per hour (logs/hr) for viability and 0.56 PCR threshold cycles per hour (cycles/hr) for PCR. The average decay rates for these control experiments (for all variables) was calculated and subtracted from the decay rates measured during all experiments. The decay data for experiments in 2015 are summarized in Table 17. Overall, the average decay in viability during experiments where *B.t.* particles were exposed to unmitigated ambient conditions was 0.72 +/-

0.23 log/hr, while when the chamber was protected from sunlight only, the loss was not detectable. The sensitivity of the *B.t.* PCR assay was also changed. On average, *B.t.* particles in the light required 2.95 +/- 2.23 more cycles of amplification per hour of aging for detection, while they only required 0.19 +/- 0.11 additional cycles per hour of aging when the chamber was protected from the sunlight. These data clearly indicate the importance of sunlight in the degradation of both viability and detection via PCR.

Date	Agent	Drum A	Drum B	Start Time	UV263	Vis263	Vis351	Viability Decay (Env) log/hr	Viability Decay (Con) log/hr	Viability Normalized log/hr	PCR Change (Env) cycles/hr	PCR Change (Con) cycles/hr	Normalized PCR Change cycles/hr
7/8/2015	Bt	Ambient	over, Carbo	1009	15.94	11.25	3.80	0.79	0.27	0.57	6.17	**	5.61
7/9/2015	Bt	Ambient	over, Carbo	1015	4.61	1.70	8.76	0.76	0.32	0.54	1.02	0.95	0.46
7/13/2015	Bt	Ambient	over, Carbo	1001	18.69	12.77	3.12	1.29	0.22	1.07	4.89	1.10	4.33
7/14/2015	Bt	Ambient	Carbon only	1015	14.20	1.93	4.44	1.11	1.08	0.89	4.91	1.40	4.36
7/15/2015	Bt	Ambient	Carbon only	1017	13.93	6.47	1.42	0.90	1.02	0.68	5.07	1.72	4.51
7/16/2015	Bt	Ambient	Carbon only	1026	13.43	8.77	-2.29	0.79	0.81	0.57	1.64	1.78	1.08
7/20/2015	Bt	Ambient	Ambient	1011	5.77	4.25	-3.37	1.28	1.28	1.06	0.89	0.62	0.34
7/21/2015	Bt	Cover only	over, Carbo	1023	11.84	13.85	-0.69	0.18	0.17	-0.04	0.83	0.17	0.27
7/22/2015	Bt	Cover only	over, Carbo	1011	12.70	12.04	-6.83	0.17	0.17	-0.05	0.62	0.38	0.07
7/23/2015	Bt	Cover only	over, Carbo	1042	10.45	5.34	-1.39	0.18	0.17	-0.04	0.79	0.20	0.23

Table 17. Decay rates and experimental conditions for 2015 field test

Fluorescence, measured by the SPFS, also shows decay as a function of exposure to the atmosphere around Houston. As previously described, the spectra obtained from SPFS data is binned into 3 bands over its two excitation wavelengths to allow for simpler description of the observed spectral changes: UV263, 263 nm excitation and emission integrated over UV wavelengths; VIS263, 263 nm excitation and emission integrated over visible wavelengths; and Vis351, 351 nm excitation and emission integrated over visible wavelengths. Because the fluorescence units are somewhat arbitrary and vary instrument to instrument, the decay rates are normalized by the peak fluorescence observed in each experiment. The rates themselves are calculated as the average of the decay between each subsequent measurement.

In the studies performed in 2015, the observed average decay rates for each band during experiments where the chamber was exposed to the ambient atmosphere and full sunlight were: UV263, 12.37 +/- 5.22 %/hr; Vis263, 6.73 +/- 4.39 %/hr; and Vis351 2.26 +/- 4.14 %/hr. In experiments where the drum was protected from sunlight, but still exposed to ambient gasses, the decay rates were: UV263, 11.66 +/- 1.14 %/hr; Vis263, 10.41 +/- 4.48 %/hr; with Vis351 showingan increase of fluorescence of 2.97 +/- 3.36 %/hr. These data clearly indicate that the presence of sunlight is important for the changes observed in some bands of fluorescence, but not all. For UV263, the decay is very similar whether the sunlight was blocked or not. Because the excitation wavelength to excite these molecules is lower, it is less likely to be photobleached by the solar radiation, indicating that other processes are likely responsible for the decay.

Processes such as ozonolysis-hydrolysis of tryptophan have been implicated by previous studies (ref). Decay in the Vis263 band appears stronger in the dark than in sunlight, but the variability in the measurements and the difference in number of experiments may explain that difference. Since the uncertainty clearly overlaps, it is likely that the decay is very similar in light and dark conditions and that other chemical processes are responsible for the observed decay. For Vis351, the change in fluorescence is extremely dependent on the presence of sunlight. Previous studies (ref) have shown that ozonlysis-hydrolysis of tryptophan can produce kynurenine, which is fluorescent in the Vis351 band. If this product is being produced in both light and dark conditions it might be photobleached in the light, causing the apparent decay, and not in the dark.

7.2.3 Decay Rates for 2016

In 2016, there were also two primary sets of experiments: daytime and nighttime. In 2015, the several experiments were performed during the day with covers blocking the solar radiation, but the atmospheric chemistry at night can be significantly different than in the daytime because the solar forcing is not driving photo-oxidation processes, and sources of both anthropogenic and biogenic compounds are different. In addition, bioaerosols were collected from the drums at more frequent intervals than in 2015. In 2015, beginning and endpoint sampler were collected for each 4 hour experiment with *B.t.*, so decay rates were calculated simply by the difference between the two.

In 2016, four samples were collected for each experiments at time 0, immediately after injection, and at 60, 120 and 240 minutes into the experiment. For these experiments, decay rates are calculated by taking the average of the decay calculated between each sample, similar to how decay rates were calculated for the fluorescence data in 2015. Similar to 2015, the data is normalized by the control drum data when the drum was isolated from the ambient gasses and sunlight. For these experiments, that occurred 3 times on the 12th and 13th of September for 2 daytime and 1 nighttime experiment. Decay rates for all experiments are shown in Table 18. For daytime experiments the average decay in viability was calculated to be 0.29 +/- 0.46 logCFU/hr, and the PCR sensitivity was found to decrease by 0.81 +/- 0.42 cycles per hour of exposure. During nighttime experiments, the average decay was not measurable above the decay measured in the completely isolated control experiments. In both the case of the viability and PCR, the average decay at night was less than the control.

Date	Agent	Drum A	Drum B	Start Time	UV263	Vis263	Vis351	Viability Decay (Env) log/hr	Viability Decay (Con) log/hr	Viability Normalized log/hr	PCR Change (Env) cycles/hr	PCR Change (Con) cycles/hr	Normalized PCR Change cycles/hr
8/29/2016	Bt	Ambient	Cover	2036	4.52	-4.02	-6.41	0.12	0.08	0.00	-0.48	-0.06	-0.10
8/30/2016	Bt	Ambient	Cover	2005	9.93	2.80	-8.05	0.06	0.06	-0.06	-0.29	-0.02	0.09
8/31/2016	Bt	Ambient	Cover	1459	18.59	3.41	-3.86	0.18	0.03	0.06	-1.03	-0.47	-0.65
8/31/2016	Bt	Ambient	Cover	2000	-4.16	-13.88	0.44	0.06	0.02	-0.06	-0.75	-0.19	-0.37
9/1/2016	Bt	Ambient	Cover	1106	10.33	2.01	-6.92	0.20	0.08	0.08	-1.20	-0.27	-0.83
9/12/2016	Bt	Ambient	Cover, Carbon	1048	NA	NA	NA	0.16	0.18	0.04	-0.75	-0.49	-0.38
9/13/2016	Bt	Ambient	Cover, Carbon	1218	NA	NA	NA	1.10	0.07	0.98	-1.76	-0.14	-1.38
9/13/2016	Bt	Ambient	Cover, Carbon	1955	NA	NA	NA	0.17	0.10	0.05	-0.60	-0.49	-0.22
9/14/2016	Bt	Carbon only	Ambient	1235	NA	NA	NA	1.25	1.31	1.14	-1.37	-1.78	-1.00
9/15/2016	Bt	Carbon only	Partial Cover	1157	NA	NA	NA	1.08	0.27	0.96	-1.92	0.88	-1.55
9/21/2016	Bt	Partial cove	Cover	1940	NA	NA	NA	0.08	0.11	-0.03	0.31	-0.63	0.68
9/22/2016	Bt	Partial cove	Cover	750	NA	NA	NA	0.14	0.06	0.02	-1.09	-0.25	-0.71

Table 18. Decay rates and experimental conditions for 2016 field test

The available, analyzed, SPFS fluorescence data from the 2016 field experiments was limited, and is summarized in Table 18. Decay rates and experimental conditions for 2016 field test. Given that data from only 2 daytime and 3 nighttime experiments were available, determining average decay rates for daytime experiments was of limited value, but calculations were made for the nighttime decay rates. During the three nighttime experiments, the UV263 decay was 3.43 +/- 7.10 %/hr, the VIS263 change was an increase of 5.03 +/- 8.38 %/hr and the VIS351 increased 4.67 +/- 4.50 %/hr. Overall, these are significantly less than the covered changes from 2015, indicating that the chemistry at night is different than the daytime chemistry, even when the influence of solar radiation is removed.

7.2.4 Correlation Analysis

In order to understand the factors that influence the observed decay, the decay rates for each variable were correlated to the available, measured environmental variables (inorganic and organic species, irradiation, etc.) described previously. The analysis was done separately for 2015 and 2016, since the available data was somewhat different between the two years. The strength of the relationship is between a calculated decay rate and an environmental variable, the square of the Pearson's R-value was calculated. Somewhat arbitrary categories of strength were used to compare the relationships between variables. R^2 values less than 0.10 are considered unrelated; R^2 values between 0.10 and 0.25 are considered very weak; R^2 values between 0.25 and 0.50 are considered weak; R^2 values between 0.50 and 0.75 are considered moderate; and R^2 values greater than 0.75 are considered strong.

Table 19 overviews the relationships using color to highlight different strengths of relationship. Viability in experiments where light was allowed into the chamber, and oxides of nitrogen and isoprene had the strongest relationships. Viability decay correlated with oxides of nitrogen has been associated with the same UV photooxidation processes that produce ozone, indicating that this decay is related to solar exposure, which was confirmed by comparing experiments with full solar to those where solar radiation was blocked.

The relationship to isoprene indicates that while the decay due to solar exposure dominates the decay, differences in the observed decay may be explained by secondary aerosol production processes due to the reaction of ozone with isoprene. Lack of observed relationship between either solar radiation or ozone may be explained by the consistency in the ozone concentration and solar radiation values during these experiments. Test locations with more varied ozone and solar radiation will offer additional insights into the correlation of decay.

PCR sensitivity has the strongest sensitivity to the higher mass organic species, especially toluene. The mild relationship to aerosol growth rates also indicates that secondary aerosol processes are likely responsible for observed decay in PCR sensitivity. As mentioned throughout this paper, the decay is likely occurring in DNA located in the spore coat and throughout the particle, rather than within the spore itself.

Decay in all bands of UV light induced fluorescence (LIF) show some relationship to solar radiation, and the VIS351 has a moderate relationship to ozone. Benzene appears to have a strong relationship to decay in UV263, which may indicate that secondary processes play a significant role in the decay of signal in this band, particularly given the relationship to measured secondary growth. Although the no particular organic compound stands out above the others, a similar situation exists for the VIS263 band. The VIS351 band appears most significantly related to ozone, oxides of nitrogen and solar exposure. This is consistent with the observation that photobleaching of the product causing an increase in the fluorescence of this band during aging due to ozonolysis-hydrolysis of tryptophan.

The relationships calculated in the absence of sunlight were significantly different. The concentration of methanol was the most significant relationship to the decay of viability, while the decay in PCR was most strongly related to high mass organics. It is important to note, however, that the actual decay was unobservable for viability and is essentially negligible for PCR sensitivity.

Table 19. Pearson's R^2 Correlation Table. X-Axis represents variables that were measured and varied over testing, Y-axis is a measured property of the bioaerosol.

Category	O3 ppbv	SO2 ppbv	Noy ppb	NO2 ppbv	NO ppbv	CO ppbv	methanol ppbv	acetaldehyde ppbv	acetone ppbv	isoprene ppbv	methyl vinyl ketone ppbv	methyl ethyl ketone ppbv	benzene ppbv	toluene ppbv	m-xylene ppbv	1,3,4-trimethylbenzene ppbv	camphene ppbv	solar avg W/m2	growth nm/hr
Light Viable	0.02	0.43	0.62	0.64	0.32	0.37	0.49	0.17	0.24	0.56	0.07	0.17	0.02	0.04	0.15	0.01	0.17	0.15	0.00
Light PCR	0.00	0.06	0.00	0.02	0.01	0.30	0.25	0.55	0.67	0.03	0.44	0.75	0.74	0.87	0.47	0.83	0.59	0.14	0.19
Light UV263	0.08	0.01	0.08	0.12	0.15	0.29	0.22	0.63	0.65	0.12	0.64	0.78	0.93	0.69	0.84	0.86	0.78	0.22	0.54
Light Vis263	0.01	0.14	0.00	0.00	0.02	0.00	0.28	0.33	0.29	0.00	0.18	0.22	0.40	0.22	0.48	0.47	0.42	0.37	0.58
Light Vis351	0.55	0.01	0.16	0.23	0.48	0.06	0.00	0.16	0.01	0.15	0.00	0.00	0.00	0.18	0.08	0.07	0.10	0.26	0.04
Dark Viable	0.13	0.05	0.53	0.70	0.45	0.20	0.79	0.42	0.70	0.04	0.48	0.22	0.02	0.00	0.03	0.17	0.01	N/A	N/C
Dark PCR	0.00	0.32	0.18	0.34	0.13	0.01	0.44	0.11	0.34	0.03	0.15	0.02	0.04	0.14	0.25	0.51	0.08	N/A	N/C
Dark UV263	0.55	0.06	0.92	0.99	0.88	0.66	1.00	0.86	0.99	0.38	0.90	0.68	0.35	0.20	0.10	0.00	0.29	N/A	N/C
Dark Vis263	0.98	0.55	0.91	0.78	0.94	1.00	0.69	0.96	0.78	0.91	0.93	1.00	0.89	0.75	0.62	0.36	0.84	N/A	N/C
Dark Vis351	0.01	0.25	0.25	0.42	0.19	0.03	0.52	0.17	0.42	0.01	0.21	0.04	0.02	0.09	0.18	0.42	0.04	N/A	N/C

Correlation analysis in 2016 was of limited value. Since no decay was observed above the control experiments for the nighttime experiments for either the PCR sensitivity or the viability, performing a correlation analysis has essentially no value. The daytime full exposure experiments only had 3 replicates and so correlation analysis indicated high degrees of relationship with many variables, due to the low number of data points. Since this does not improve our understanding of the chemistry, it is not presented here.

8. DISCUSSION AND CONCLUSION

The experiments overviewed represent an initial, but comprehensive examination of the primary types of environmental chemistry that might reasonably impact the viability of bioaerosols in the atmosphere, and our ability to detect them. The laboratory studies examined the impact of simulated solar radiation, relative humidity, ozone, alpha-pinene and toluene individually and in combination. *Bacillus thuringiensis, Escherichia coli* and MS2 phage were used to simulate the three common classes of biological aerosols of concern. The field studies examined the aging of *B.t.* under ambient environmental conditions, while measuring those inorganic and organic trace gasses, particle growth rates, solar radiation and environmental variables. It is understood that the specific decay rates measured in both the laboratory and field measurements are only directly relevant to the specific organism and assays being evaluated, the elucidation of key factors contributing to that decay when generalized across all simulants and compared between the field and laboratory studies can lead to an improvement in the understanding of key factors and the chemistry underlying the degradation of nucleic acid and proteins, leading to decays in assay sensitivity and ultimately to loss in viability.

In the laboratory experiments, a few broad generalizations can be made across the simulants. First, simulated solar radiation is a key factor in the degradation of viability and PCR sensitivity. Second, ozone, particularly at high relative humidity is also a major factor in the loss of viability and PCR sensitivity. Lastly, and the most striking result, is that ozone, simulated solar radiation and the presence of one or the other VOC creates the most significant decay in both viability and PCR sensitivity, in most cases. These aging scenarios still underestimate the more complex outdoor environment, and offer just a fraction of the total number of atmospheric chemistry reactions and condensing secondary organic byproducts.

In the field experiments, some very similar generalizations can be made based on the correlation analysis that was performed and comparison of the decay rates for different experiment types.

Similar to the laboratory experiments, sunlight played a major role in the observed decay. In 2015, it was virtually impossible to see any degradation in the viability that was not due to solar exposure. This goes beyond just degradation due to sunlight. Comparison of the results between daytime 2015 experiments when the chambers were shielded from the sun and 2016 nighttime experiments, shows different decay rates for the two conditions, suggesting that the photochemistry going on outside the chamber during the day is still influencing the bioaerosols inside the chamber, while the nighttime experiments experienced a different chemical environment and aging process. Second, secondary organic aerosol processes (photooxidation of VOCs to produce additional condensable aerosol mass) appear to be a major factor in the degradation of PCR sensitivity, UV LIF at various bands, and viability. This is a new result and adds complexity to previous attempts to understand the chemistry behind the degradation of tryptophan via ozonolysis-hydrolysis. Since we observe a relationship between some high mass organic species and degradation of UVLIF (particularly the UV263 band, which is most sensitive to tryptophan) it indicates that the ozonolysis-hydrolysis process for the degradation of tryptophan may be only one of several mechanisms operating. This may explain the lack of observation of an increase the VIS351 band that would be expected from the production of kynurenine (as described by Pan et al.), especially when combined with the photobleaching that is likely occurring due to solar exposure.

The production of reactive oxygen species (ROS) and reactive nitrogen species (RNS) by SOA from both biogenic (e.g. alpha-pinene) and anthropogenic (e.g. toluene) when exposed to biological systems (ref), has recently been implicated as a source of the increased health effects due to exposure to these aerosol (ref). It is reasonable to assume that the same ROS and RNS production responsible for human health effects may be directly impacting the proteins and nucleic acids of bioaerosol. Both the laboratory and field results indicate that bioaerosol decay (as measured in multiple modalities) is more rapid than when SOA production is more likely. Detailed study of these processes is warranted to better understand the potential impacts to our understanding of persistence of biological particles.

Several factors limited this study, particularly in the field. First, the study was heavily reliant on unpaid collaborators for environmental data. Although it was cost effective to team with other studies to obtain this data, it limited the field studies to the Jones State Forest in Texas and did not afford control over the data being collected. This severely impacted the analysis in some respects, but nevertheless, collaboration with these groups was invaluable for field tests. Going forward, Sandia has procured its own PTRMS system to allow a more flexibility over location and better control over data quality and focus.

Secondly, shipping samples from the field to the lab at Sandia for analysis likely created a limitation to our ability to study the more fragile organisms (E. coli and MS2) during the field study. Shipping, even overnight, a stressed and fragile organism likely resulted in significantly fewer observable viable organisms than could be observed if the assays had been done the day of collection. This was recognized and a fieldable biological laboratory capability is currently being finalized to support future efforts. Lastly, a complete understanding of what compounds are affecting the bioaerosol was not possible. Although the correlation analysis provided new clues to understanding the SOA chemistry impacting bioaerosols in this study, and the laboratory data supported the fact that both toluene and alpha-pinene could cause increased decay in photooxidative conditions, neither result clearly identifies which compounds are the most

prevalent under actual ambient conditions. Aerosol mass spectrometry is the only way to identify the SOA prevalent on the aerosols in near real-time. Sandia has procured a Livermore Instruments SPAMS 3.1 to help resolve these questions in future experiments. This system should be able to ablate the surface coating of a bioaerosol to understand which chemical species are present and likely contributing to the biological decay of these particles.

REFERENCES

1. Almeida JL, Harper B, Cole KD. Bacillus anthracis spore suspensions : determination of stability and comparison of enumeration techniques. 2008;104:1442-1448. doi:10.1111/j.1365-2672.2007.03684.x.

2. Goodwin RD. Toluene Thermophysical Properties from 178 to 800 K at Pressures to 1000 Bar. *J Phys Chem Ref Data*. 1989;18(4):1565-1636. doi:10.1063/1.555837.

3. Guenther AB, Jiang X, Heald CL, et al. Model Development The Model of Emissions of Gases and Aerosols from Nature version 2 . 1 (MEGAN2 . 1): an extended and updated framework for modeling biogenic emissions. 2012:1471-1492. doi:10.5194/gmd-5-1471-2012.

4. Hurley MD, Sokolov O, Wallington TJ. Organic aerosol formation during the atmospheric degradation of toluene. *Environ Sci Technol*. 2001;35(7):1358-1366. doi:10.1021/es0013733.

5. Lu J, Gerke TL, Buse HY, Ashbolt N. Development of an Escherichia coli K12-specific quantitative polymerase chain reaction assay and DNA isolation suited to biofilms associated with iron drinking water pipe corrosion products. *J Water Health*. 2014;12.4(December):763-771. doi:10.2166/wh.2014.203.

6. Nicholson & Setlow, P. Molecular Biological Methods for Bacillus, eds. C. Harwood & S. Cutting, New York: John Wiley, pp.391-450, 1990

7. O'Connell KP, Bucher JR, Anderson PE, et al. Real-Time Fluorogenic Reverse Transcription-PCR Assays for Detection of Bacteriophage MS2. 2006;72(1):478-483. doi:10.1128/AEM.72.1.478.

8. Qiu C, Khalizov AF, Zhang R. Soot aging from OH-initiated oxidation of toluene. *Environ Sci Technol*. 2012;46(17):9464-9472. doi:10.1021/es301883y.

9. Pan Y, Hill SC, Coleman M. Photophoretic trapping of absorbing particles in air and measurement of their single-particle Raman spectra. 2012;20(5):145-147.

10. Santarpia JL, Pan Y, Hill SC, et al. Changes in fluorescence spectra of bioaerosols exposed to ozone in a laboratory reaction chamber to simulate atmospheric aging. 2012;20(28):348-357.

11. Ratnesar-Shumate S, Pan Y, Hill SC, et al. Journal of Quantitative Spectroscopy & Radiative Transfer Fluorescence spectra and biological activity of aerosolized bacillus spores and MS2 bacteriophage exposed to ozone at different relative humidities in a rotating drum. *J Quant Spectrosc Radiat Transf*. 2015;153:13-28. doi:10.1016/j.jqsrt.2014.10.003.

APPENDIX A T-TABLES

Appendix of Statistical Tests

***E. coli* Viability UV Light**

t-Test: Two-Sample Assuming Equal Variances

	No-UV	*UV light*
Mean	-0.4624943	-0.7466471
Variance	0.11953804	0.3699295
Observations	6	6
Pooled Variance	0.24473377	
df	10	
t Stat	0.99486853	
P(T<=t) one-tail	**0.1716317**	
t Critical one-tail	1.81246112	

***E. coli* Viability RH**

t-Test: Two-Sample Assuming Equal Variances

	Low RH	*High RH*
Mean	-0.462494285	-0.8292386
Variance	0.119538036	0.11368385
Observations	6	5
Pooled Variance	0.116936173	
df	9	
t Stat	1.771141512	
P(T<=t) one-tail	**0.055153859**	
t Critical one-tail	1.833112933	

***E. coli* Viability Ozone**

t-Test: Two-Sample Assuming Equal Variances

	No Ozone	*Ozone*
Mean	-0.462494285	-0.7845096
Variance	0.119538036	0.25837556
Observations	6	6
Pooled Variance	0.188956796	

df	10
t Stat	1.283086338
P(T<=t) one-tail	**0.114200091**
t Critical one-tail	1.812461123

E. coli Viability Toluene

t-Test: Two-Sample Assuming Equal Variances

	W/O Toluene	*W/ Toluene*
Mean	-0.4624943	-0.8420124
Variance	0.11953804	0.07554484
Observations	6	3
Pooled Variance	0.10696855	
df	7	
t Stat	1.64104087	
P(T<=t) one-tail	**0.0723970**	
t Critical one-tail	1.89457861	

E. coli Viability Toluene and UV light

t-Test: Two-Sample Assuming Equal Variances

	UV light W/O Toluene	*UV light W/ Toluene*
Mean	-1.0951768	-2.4301991
Variance	0.44842336	0.94877385
Observations	10	11
Pooled Variance	0.71176573	
df	19	
t Stat	3.6216517	
P(T<=t) one-tail	**0.00090835**	
t Critical one-tail	1.72913281	

E. coli PCR Toluene and UV light

t-Test: Two-Sample Assuming Equal Variances

	UV light W/O Toluene	*UV light W/ Toluene*
Mean	-0.215061205	-0.358475745
Variance	0.043547026	0.051714176
Observations	10	11
Pooled Variance	0.047845526	
df	19	
t Stat	1.500580203	
P(T<=t) one-tail	**0.074949698**	
t Critical one-tail	1.729132812	

***E. coli* PCR A-pinene and UV light**

t-Test: Two-Sample Assuming Equal Variances

	UV light W/O A-pinene	*UV light W/ A-pinene*
Mean	-0.2150612	-0.2073793
Variance	0.04354703	0.11444326
Observations	10	11
Pooled Variance	0.08086084	
df	19	
t Stat	-0.0618279	
P(T<=t) one-tail	**0.47567281**	
t Critical one-tail	1.72913281	

***B.t.* Viability UV light**

t-Test: Two-Sample Assuming Equal Variances

	No UV	UV light
Mean	-0.05209884	-0.32169
Variance	0.003266944	0.03619151
Observations	7	28
Pooled Variance	0.030205227	
df	33	
t Stat	3.67078234	
P(T<=t) one-tail	**0.00042376**	
t Critical one-tail	1.692360309	

***B.t.* Viability Pinene**

t-Test: Two-Sample Assuming Equal Variances

	No Pinene	*Pinene*
Mean	-0.0766603	-0.1233333
Variance	0.00221399	0.00333333
Observations	4	3
Pooled Variance	0.00266173	
df	5	
t Stat	1.18447445	
P(T<=t) one-tail	0.14472779	
t Critical one-tail	2.01504837	

***B.t.* Viability Pinene and UV light**

t-Test: Two-Sample Assuming Equal Variances

	UV light	*UV light and A-Pinene*
Mean	0.399737868	-0.4461126
Variance	0.002348542	4.7543E-05
Observations	3	3
Pooled Variance	0.001198042	
df	4	
t Stat	1.64093403	
P(T<=t) one-tail	0.088077549	
t Critical one-tail	2.131846786	

***B.t.* Viability Pinene, UV Light & Ozone**

t-Test: Two-Sample Assuming Equal Variances

	UV light and Ozone	*UV light, Ozone and Pinene*
Mean	-0.3585393	-0.4868163
Variance	0.00861108	0.00117488
Observations	3	3
Pooled Variance	0.00489298	

df	4
t Stat	2.24598926
P(T<=t) one-tail	0.04401774
t Critical one-tail	2.13184679

MS-2 Infectivity UV Light

t-Test: Two-Sample Assuming Equal Variances

	No UV light	*UV light*
Mean	-0.0852954	-0.9374559
Variance	0.00121685	0.03913942
Observations	3	4
Pooled Variance	0.02397039	
df	5	
t Stat	7.20651729	
P(T<=t) one-tail	**0.00040085**	
t Critical one-tail	2.01504837	

MS-2 Infectivity High RH

t-Test: Two-Sample Assuming Equal Variances

	Low RH	*High RH*
Mean	-0.0852954	-0.4731788
Variance	0.00121685	0.01672748
Observations	3	3
Pooled Variance	0.00897217	
df	4	
t Stat	5.0153143	
P(T<=t) one-tail	**0.00370491**	
t Critical one-tail	2.13184679	

MS-2 Infectivity High RH and Ozone

t-Test: Two-Sample Assuming Equal Variances

	Ozone and High RH	*High RH*
Mean	-0.845	-0.4731788
Variance	0.00125	0.01672748
Observations	2	3
Pooled Variance	0.01156832	

df	3
t Stat	-3.786951
P(T<=t) one-tail	**0.01614503**
t Critical one-tail	2.35336343

MS-2 Infectivity Ozone

t-Test: Two-Sample Assuming Equal Variances

	No Ozone	*Ozone*
Mean	-0.085295398	-0.1066667
Variance	0.001216854	0.00203333
Observations	3	3
Pooled Variance	0.001625094	
df	4	
t Stat	0.64928707	
P(T<=t) one-tail	**0.275775571**	
t Critical one-tail	2.131846786	